ACOUSTIC EMISSION AND MECHANICAL PROPERTIES OF PARTICLE REINFORCED COMPOSITES

by

ANA ESMERALDA GODOY

B.Sc., (Metallurgical Engineering),

University Simon Bolivar, Venezuela, 1979

A THESIS SUBMITTED IN PARTIAL FULFILMENT OF

THE REQUIREMENTS FOR THE DEGREE OF

MASTER OF APPLIED SCIENCE

in

THE FACULTY OF GRADUATE STUDIES

Department of Metallurgical Engineering

We accept this thesis as conforming

to the required standard

THE UNIVERSITY OF BRITISH COLUMBIA

August, 1982

In presenting this thesis in partial fulfilment of the requirements for an advanced degree at the University of British Columbia, I agree that the Library shall make it freely available for reference and study. I further agree that permission for extensive copying of this thesis for scholarly purposes may be granted by the head of my department or by his or her representatives. It is understood that copying or publication of this thesis for financial gain shall not be allowed without my written permission.

Department of Metl Eng.

The University of British Columbia
1956 Main Mall
Vancouver, Canada
V6T 1Y3

Date 17/09/82

ABSTRACT

Fracture and acoustic emission (AE) tests were performed on alumina particle-filled epoxy and alumina particle-filled martensitic steel composites. The ring-down counting method was used to measure AE.

Three-point bending tests were carried out for the martensitic steel composites and AE was recorded during the fracture test. The alumina appeared to have little effect on the AE from martensitic steel.

The elastic modulus and AE attenuation of the alumina particle-filled epoxy composites were analyzed. The elastic modulus and AE attenuation of the epoxy composites were independent of the average alumina particle size. The elastic modulus increased with increasing alumina volume fraction and the AE attenuation decreased slightly with increasing alumina volume fraction.

Double torsion, wedge-loading and three-point bending fracture tests were carried out for the alumina-reinforced epoxy composites. AE was recorded during each fracture test. The fracture energy and toughness values increased with increasing volume fraction and were independent of the particle

size. The increase in fracture surface due to the presence of particles accounted for about 60% of the increase in fracture energy.

Crazing seemed to be the major source of AE in pure epoxy. During failure of the composites the AE increased with increasing particle size. A cut-off value in particle size at about 40 μm appears to exist, below which no increase in AE occurs with the addition of particles. For intermediate alumina volume fractions a maximum was observed in AE versus volume fraction curves. The pinning and release of the crack front due to the presence of hard particles appeared to be the major contributing factor to the AE of the epoxy composites.

TABLE OF CONTENTS

LIST OF TABLES

LIST OF FIGURES

NOMENCLATURE

Symbol	
a	crack length
A	amplitude of acoustic wave
A_s	total area of intersected particles
A_t	Parameter in equations for calculating the theoretical elastic modulus of particle-filled composites
AE_{MOD}	AE at a zero distance between source and transducer
B	Beam thickness
B_c	Constant dependent on the elastic modulus
B_n	slab thickness in the plane of the crack
c	parameter in equations for calculating the theoretical elastic modulus of particle-filled composites
C	compliance
C_c	constant dependent on the dimensions of double torsion specimens
d	interparticle distance
D	average filler particle size
E	modulus of elasticity
E_A	elastic modulus of alumina
E_C	elastic modulus of a composite
E_E	elastic modulus of epoxy
E_G	elastic modulus of glass

Symbol

E_{AE}	acoustic emission energy
F	fraction of acoustic emission wave population
F_F	friction force
G	fracture energy
G_{co}	corrected fracture energy
G_o	energy per unit area required to form a new fracture surface
H	beam width in wedge-loading tests
I_p	moment of inertia of a non-grooved sample
I_{sg}	moment of inertia of a grooved sample
K	stress intensity
L/2	distance between loading points in three-point bending tests
L_T	total specimen lenght
w	weight
m_A	weight of alumina
m_{A+B}	weight of alumina powder and porcelain boat
$m_{accelerator}$	weight of epoxy accelerator
m_B	weight of porcelain boat
$m_{curing\ agent}$	weight of curing agent
m_{LE}	weight of liquid epoxy
m_{resin}	weight of epoxy resin
m_s	weight of a sample
$(m_s)_w$	weight of a sample immersed in water
n(A)	fraction of the emission with a peak amplitude greater than A

Symbol	
N	number of ring-down counts
N_s	average number of particle intersections per unit area of sectioning plane
N_v	number of particles per unit volume
$\dot{N}(t)$	ring-down count rate
p	probability of fracture plane intersecting a particle
P	applied load
s	groove half length
SLO	slope of pulser counts versus distance calculated lines
S_p	surface of a particle
t	time
T	critical line energy per unit length of crack front
T_H	highest curing temperature
T_p	ambient temperature
U_f	work of friction forces
V_A	volume of alumina
V_f	volume fraction of filler
V_{LE}	volume of liquid epoxy
V_o	maximum initial voltage
V_p	volume of a particle
V_{SE}	volume of solid epoxy
V_t	threshold voltage

Symbol	
V_T	total volume
$V(t)$	RMS voltage at a time t
w_m	moment arm in double torsion tests
W	bar width in double torsion tests
W_B	width of three-point bending specimens
X_n	crack length elevated to the n^{th} power
y	deflection of beams
y_{INT}	y intercept of pulser counts versus distance calculated lines
Y	parameter in the stress intensity equation of three-point bending specimens
α	thermal contraction coefficient
$\alpha_{Al_2O_3}$	thermal contraction coefficient of alumina
α_{epoxy}	thermal contraction coefficient of epoxy
α_n	fitting parameter in compliance equations
β	logarithmic voltage decrement
θ	wedge half angle
ν	Poisson's ratio
ν_A	Poisson's ratio of alumina
ν_E	Poisson's ratio of epoxy
ν_R	transducer resonant frequency
ρ	density
ρ_A	density of alumina
ρ_E	density of epoxy
ρ_I	density of bubble-free epoxy composites

Symbol

ρ_{LE}	density of liquid epoxy
ρ_s	density of a composite
ρ_w	density of water
σ	thermal stress

ACKNOWLEDGEMENT

The author wishes to thank Dr. J.S. Nadeau, Mr. Roger Bennett, Mrs. D. Benz and Mrs. E. Nadeau for their guidance and encouragement with this work.

Acknowledgement is made of financial assistance from the National Science and Engineering Research Council of Canada.

1. INTRODUCTION

Acoustic emission is the name given to the elastic waves generated during transient changes in the local stress and strain fields within a material. The term is also applied to the techniques used to detect such elastic waves.

In many studies over the last twenty years acoustic emission has been monitored in order to obtain a greater insight into deformation, failure and fracture processes in materials. This technique has been used as a tool for quality control, failure analysis and failure prevention. However, the sources, propagation and detection of acoustic emission are not yet clearly understood. Full advantage of acoustic emission techniques will not be realized until fundamental knowledge such as the nature of the generation of the acoustic waves is obtained. It was the overall objective of this study to gain insight into some fundamental mechanisms of acoustic emission generation. The specific objectives were the following:

(i) to determine the effect of particle size and volume fraction on the mechanical properties and on acoustic emission during the fracture of particle-filled composites.

(ii) to relate fundamental fracture mechanisms to the acoustic emission of particle-filled composites.

First, a brief summary is given of the present state of knowledge on acoustic emission.

1.1. Measurement of Acoustic Emission

1.1.1. Instruments Required for the Detection of Acoustic Emission

Acoustic emission monitoring techniques are active testing methods in which the acoustic emission signals are transient and generated in conjunction with failure, deformation or phase transformation processes within a structure. Sensitive electromechanical transducers are used to detect strain waves on the surface of the monitored structure. The response of the transducer to a strain wave (event) becomes the "acoustic emission" signal which is electronically processed. It is passed through a first amplifier which, in addition to amplifying the signals, produces harmonics of the signal and contributes a great deal of the system noise[1]. Therefore, the first amplification is kept to a minimum and is followed by filtering and reamplifying. The signal then is analyzed in a processing unit.

This step will be explained in Section 1.1.2. The final output is shown on a digital display and/or plotted on a chart (Fig. 1).

1.1.2. Parameters Used for Measuring Acoustic Emission

1.1.2.1. Ring-Down Count Method

The number of times the magnitude of the voltage (amplitude) in an acoustic emission event exceeds a threshold value is defined as the ring-down count number for that event (Fig. 2). The signals are usually in the form of damped sinusoids and the number of ring-down counts, N, for an event detected by the transducer has been shown to be[2]:

$$N = \frac{\nu_R}{\beta} \ln \frac{V_o}{V_t} \qquad (1)$$

where ν_R is the transducer resonant frequency,
β is the logarithmic voltage decrement,
V_o is the maximum initial voltage, and
V_t is the threshold voltage.

The count rate is the ratio of the number of counts to the time during which they take place.

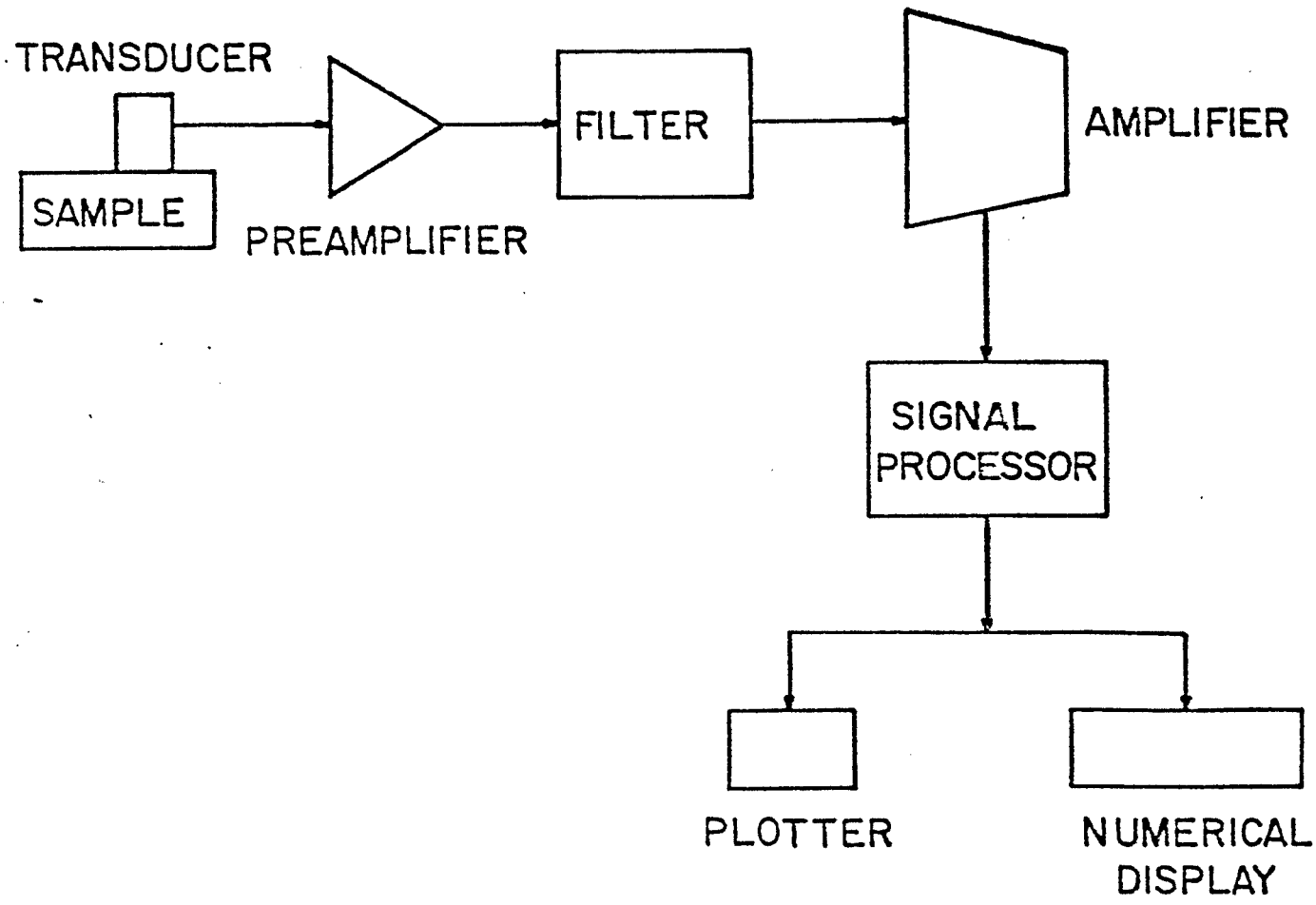

Figure 1. Acoustic emission monitoring system.

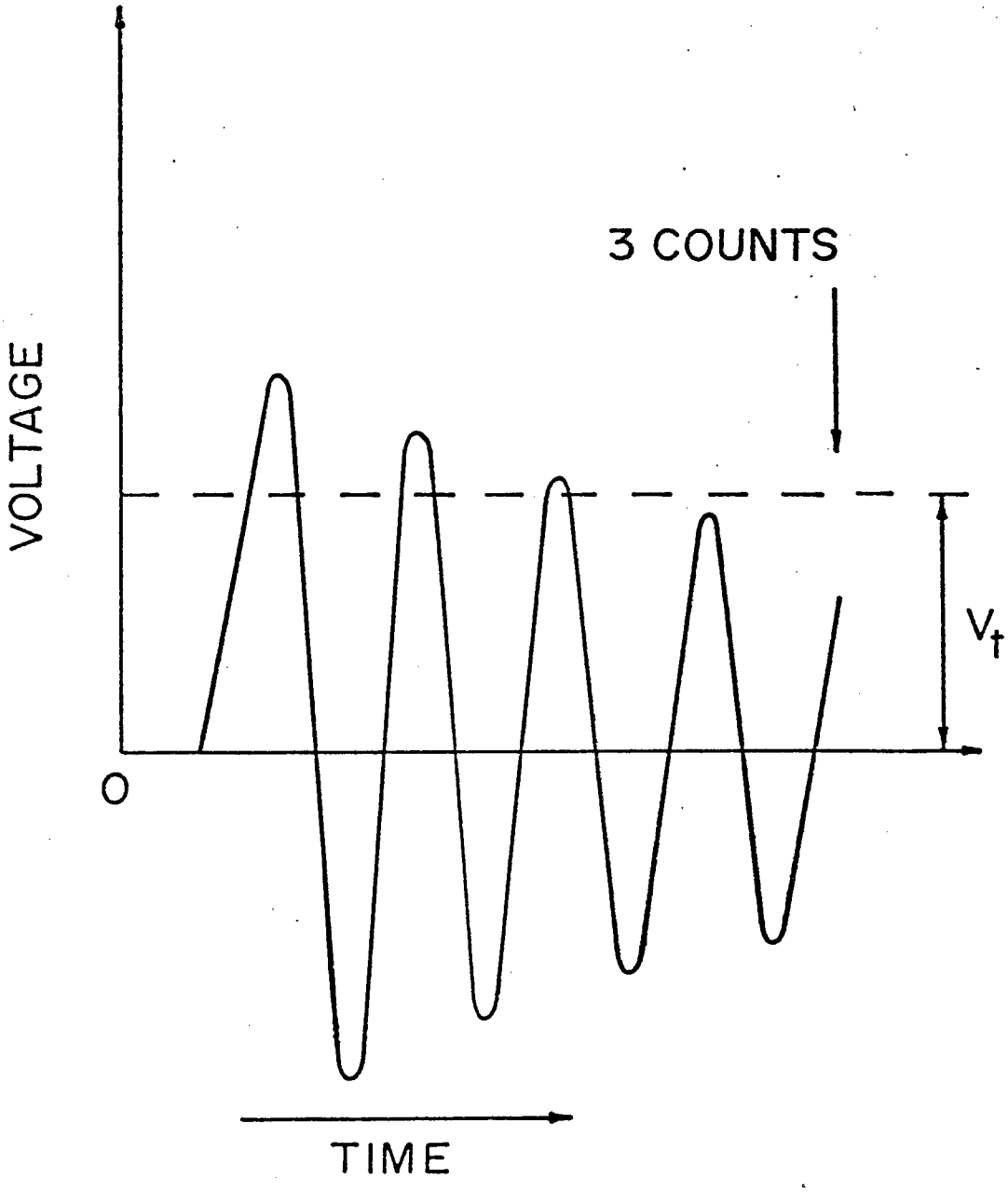

Figure 2. Ring-down count method; V_t is the threshold voltage.

The number of counts is influenced by the following factors:

(i) the geometry of the specimen.
(ii) gain (magnitude of amplification of the signal).
(iii) performance of the amplifiers and filters.
(iv) selected frequency range.
(v) detection threshold voltage.
(vi) transducer to specimen bond.
(vii) transducer to source distance.
(viii) transducer properties.

The number of counts is not a measure of a fundamental property.

1.1.2.2. Root Mean Square (RMS) Method

This technique measures the root mean square of the amplitude of the acoustic signals and is not dependent on threshold voltage. Used alone it yields information on the intensity of acoustic emission, but it does not give an indication of the strain energy released in the total fracture process. Therefore, the RMS method is more suitable for studying acoustic emission intensity.

Energy analysis is possible by using more sophisticated equipment and can mean one of the following:

(i) the sum of the squares of the peak emission voltages.

(ii) the area under squared voltages on the squared voltage vs. time curve.

(iii) $$E_{AE} = \Sigma \dot{N}(t) V^2(t) \qquad (2)$$

where E_{AE} is the measured energy,

$\dot{N}(t)$ is the count rate,

$V(t)$ is the RMS voltage at a time t.

The RMS and energy analysis methods are influenced by the same variables that affect the ring-down count method with the exception of the detection threshold voltage.

1.1.2.3. Amplitude Distribution Analysis

The distribution of amplitudes of acoustic emission events are analyzed. An amplitude sorter, which is responsive only to the peak amplitude of the signal, not to the ring-downs which tend to obscure the essential data, has been employed[3]. The sorter separates the amplitudes into different amplitude ranges. For example, the Dunegan Endevco amplitude sorter separates the signals into the following ranges: 0.05 - 0.5, 0.5 - 50, 50 - 500, 500 - 5000 and

> 5000 mV^3. The fraction of the emission population whose amplitude falls between A and A + δA, where A is the peak amplitude, is given by the following relation[3]:

$$F = n(A + \delta A) - n(A) \qquad (3)$$

where n(A) is the fraction of the emission population whose peak amplitude exceeds A.

Amplitude distribution analysis is useful for recognizing specific deformation processes in the presence of background noise. It can also detect significant changes in the nature of the deformation or failure mechanism. This technique becomes very useful, for example, in fibre composites, where different failure processes such as matrix yielding and fibre failure occur. Therefore, amplitude distribution analysis can complement ring-down count and RMS measurements.

1.1.2.4. Frequency Analysis

The emission signal is passed into a transient recorder where the waves are translated into digital form for processing by a computer. Fourier transform programs interpret the data as a relation between peak amplitudes and wave frequency[2].

This technique can reveal wave frequencies characteristic of particular acoustic emission sources. Ideally, major amplitude peaks should occur for such frequencies. For example, in fibre reinforced composites, fibre failure and matrix yielding should exhibit different characteristic wave frequencies. It appears that the geometry of the sample does not always have a pronounced influence on the frequency analysis[2].

This method requires a great deal of instrumentation and the interpretation of results is complex. Therefore, it is not as commonly used as the other methods.

1.2. Sources of Acoustic Emission

At present, the following processes have been identified as acoustic emission sources:

(i) dislocation glide[4,5],
(ii) release of dislocation pile-ups from pinning points[4],
(iii) decohesion and fracture of second phases and of inclusions[6-12],
(iv) release of cracks from pinning points[13],
(v) phase transformations[14,15].

1.3. Current Research on Acoustic Emission

The major concerns about acoustic emission are related to its generation, propagation and detection.

Attempts have been made to characterize the effect of microstructure and macroscopic parameters, such as bulk stress, strain and toughness, on the generation of acoustic waves[2,4-12]. Other studies have analyzed the change of local stress and strain fields with time[2,13].

Acoustic emission measurements are influenced by the scattering of waves at structural boundaries, system resonances and attenuation. Energy loss through thermal effects, interaction with dislocations, interaction with second phases and microstructural discontinuities causes attenuation of the propagating stress wave. The decrease of amplitude due to the spreading of the wave in space also contributes to attenuation[16]. Attenuation has been expressed as a function of the dispersion of sound waves and of the absorption of the waves into the material[17]. Because of the numerous variables involved, very little work has been done on attenuation.

Attempts are being made to standardize acoustic emission measurements so that results obtained using different testing

techniques become comparable. It then becomes possible, for instance, to compare experiments done with different gains[2,18], materials and equipment.

2. EXPERIMENTAL PROCEDURE

In this chapter a rationale and a description have been given of the selection of materials, composite fabrication, material characterization tests, fracture and acoustic emission experiments. The materials selected were alumina-filled epoxy and alumina-filled martensitic steel.

The experiments on epoxy composites were divided into three categories:

1) material characterization
2) fracture tests
3) acoustic emission tests

In the section dealing with material characterization, the purpose and procedure of measuring the density, elasticity and attenuation were given; the data from these tests were essential to interpret the results from the fracture and acoustic emission experiments.

Fracture tests consist of double torsion, wedge loading, and three-point bending tests. Double torsion tests were undertaken for studying fracture and acoustic emission. However, these tests were abandoned for reasons explained in this chapter. To confirm wedge-loading tests, three-point

bending tests were carried out.

Acoustic emission was monitored during every fracture test performed.

For alumina-filled martensitic steel only three-point bending tests were conducted because of experimental difficulties.

2.1. Selection of Materials

The criteria for selecting the material to be tested were as follows:

(i) the materials had to have a minimum number of mechanisms of acoustic emission during fracture.
(ii) the microstructure of the material chosen had to be easy to control and reproduce.

In order to fulfill these requirements, particle-filled composites were chosen and the selection of a brittle matrix and hard filler particles was made. Sources of acoustic emission, such as dislocation glide, dimple formation, yielding, and the fracture of particles were thus avoided.

The material selected as a filler was aluminum oxide, which is very hard and is available in a wide range of particle sizes. The aluminum oxide used was technical abrasive grain type W from Carborundum. It was sieved and separated into the following size ranges: 36-44 μm, 55-74 μm, 75-105 μm, 106-124 μm, 125-149 μm.

Zinc and epoxy were initially selected as matrices. Zinc was subsequently discarded in favour of martensitic steel because it was found that the zinc composite was very ductile and thus not suitable for brittle fracture tests. To fabricate the martensitic steel matrix from powder, iron powder of the following composition was used:

Carbon:	0.105 wt.%
Mn:	0.01 wt.%
Si:	0.10 wt.%
Fe Atomet 28:	balance

The source of carbon was Fisher Scientific technical grade of graphite powder.

The epoxy was fabricated using the hardener nadic methyl anhydride (Ciba Geigy 906), the epoxy resin EPON 828 (Shell) and the accelerator triethylamine (Ciba Geigy 6010).

2.2. Fabrication of Composites

2.2.1. Fabrication of Epoxy Composites

The cycle of mixing and curing used was described by R.J. Crowson and R.G.C. Arridge[19]. The matrix material had the following composition:

100 parts by weight	-	Resin Epon 828
90 parts by weight	-	curing agent nadic methyl anhydride
2 parts by weight	-	accelerator triethylamine

The alumina powder was first added to the curing agent. The mixture was heated to ≈ 40°C and stirred for 20 minutes. The epoxy resin was then added and the mixture was heated and stirred for 20 minutes. The mixture was left standing in a vacuum dessicator for five minutes. After removing it from the dessicator the accelerator was added and the mixture was heated for five more minutes. The mixture was cast into a heated mould and rotated at a frequency of 3.5 rev/min for sixteen hours at 100°C. To end the curing process, the temperature was increased to 150°C for one hour and finally to 200°C for half an hour. The mould consisted of two aluminum plates and a silicone rubber frame (Fig. 3). This type of mould allowed heat, and trapped gases to be

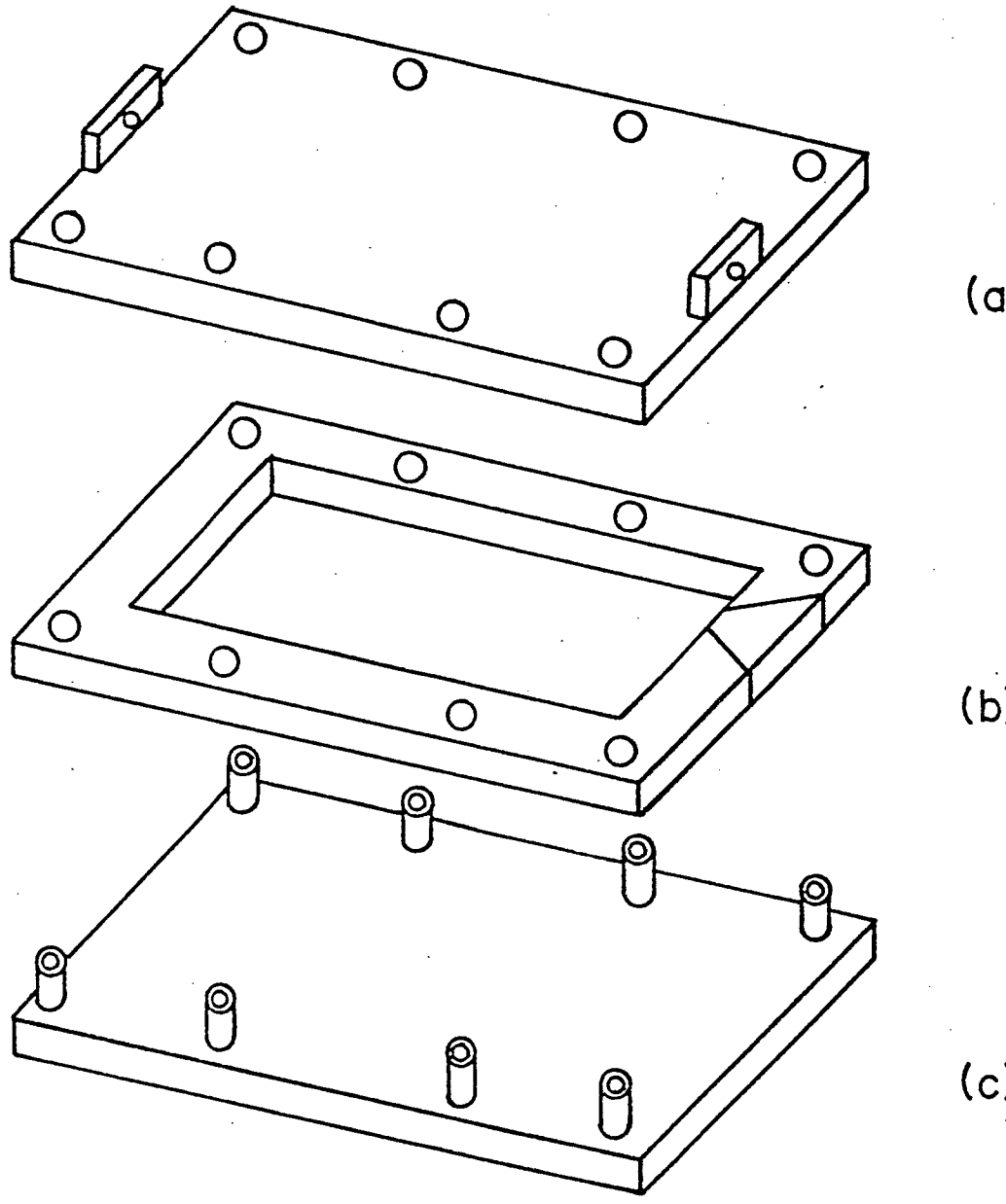

Figure 3. Epoxy composites mould.
(a) and (c). Aluminum plates.
(b). Silicon rubber gasket.

released while the epoxy cured. The samples obtained were rectangular slabs measuring 22 cm x 7.6 cm x 1.3 cm. The formulas used to calculate the amounts of resin, curing agent, accelerator, and alumina necessary for achieving a particular volume fraction of filler, V_f, were developed as follows:

$$V_f = \frac{V_A}{V_T} \tag{4}$$

$$1 - V_f = \frac{V_{SE}}{V_T} \tag{5}$$

where V_A is the volume of aluminum oxide,
V_{SE} is the volume of solid epoxy, and
V_T is the volume of the composite.

Epoxy shrinks during curing. The shrinkage is approximately 5% of the volume of liquid epoxy (V_{LE}). Thus,

$$1 - V_f = \frac{0.95\ V_{LE}}{V_T} \tag{6}$$

Substituting volume V with mass density ratio, m/ρ:

$$m_A = V_T \rho_A V_f \tag{7}$$

$$m_{LE} = \frac{1}{0.95} V_T \rho_{LE} (1 - V_f) \quad (8)$$

where $\rho_A = 3.90$ gr/cc ±

$\rho_{LE} = 1.17$ gr/cc ±

$V_T = 226$ cc ±

Considering a 1% loss of material during casting:

$$m_A = 890\ V_f \quad (9)$$

$$m_{LE} = 281(1 - V_f) \quad (10)$$

From the composition of the matrix (described at the beginning of this section) the following equations can be obtained:

$$m_{resin} = 0.521\ m_{LE} \quad (11)$$

$$m_{curing\ agent} = 0.469\ m_{LE} \quad (12)$$

$$m_{accelerator} = 0.010\ m_{LE} \quad (13)$$

2.2.2. Fabrication of Steel Composites

Particle-filled steel was obtained by hot forging a mixture of graphite, iron and alumina powders. The graphite

content was 1 wt.% in the iron-graphite mixture. This powder was enclosed in a steel container, covered with graphite cups to prevent decarbonization, and heated at 1100 C for 15 minutes. It was then placed in a forging die made of hot worked steel of a hardness of 50 R_C. The load used for forging was 40 KN and the loading rate was 50 KN/sec. The cylindrical forged product had a diameter of 5.70 cm and a height of 1.55 cm.

The material was then hot rolled at 1100°C. The steel was covered by graphite during heating. Six passes, each of approximately 1.5 mm reduction in thickness, were used.

The samples contained volume fractions of alumina particles from 0 to 0.05. Samples of similar volume fractions but containing alumina of different grain sizes, Section 2.1., were also made.

2.3. Tests on Epoxy Composites

2.3.1. Material Characterization

2.3.1.1. Density and Particle Volume Fraction Determination

After casting, the actual volume fraction of alumina was unknown because particle segregation occurred during

this process. The density of the composites was measured in order to calculate the void percentage introduced by the particles. Density values were essential to measure the volume fraction of the filler.

After a sample was broken, a piece was cut from one of the fracture faces. The density of the piece was measured using the water immersion method. Small strings of thin nylon thread were glued to the specimen in order to suspend it on an analytical balance. The sample was dried, weighed, immersed in water, and weighed again. Density was determined using the following equation:

$$\rho_s = \frac{m_s}{\frac{m_s - (m_s)_w}{\rho_w}} \qquad (14)$$

where ρ_s is the sample density,

m_s is the weight of the sample,

$(m_s)_w$ is the weight of the sample immersed in water, and

ρ_w is the density of water.

Next the amount of alumina in the sample was determined by the following procedure:

The epoxy composite sample and a porcelain boat were dried and weighed separately. The boat was again weighed with

the specimen inside, and placed in the furnace at 550°C for an hour. Only alumina was left in the container and the weight of boat and powder together was measured.

$$V_f = \frac{(m_{A+B} - m_B)/\rho_A}{m_s/\rho_s} \qquad (15)$$

where m_{A+B} is the weight of alumina powder and boat
and m_B is the weight of the boat

The density of alumina was measured using a pycnometer.

2.3.1.2. Elastic Constants

Elastic constants were needed to verify the analytical equations (Sect. 2.3.2.2.) developed for the stress intensity in wedge loading tests (Fig. 4).

The data required for calculating the modulus of elasticity were obtained while calibrating the compliance+ of wedge-loaded specimens. The procedure of this experiment is described in Section 2.3.2.4.

$$E = \frac{8a^3P}{H^3By} \qquad (16)$$

+ Specimen deflection per unit load

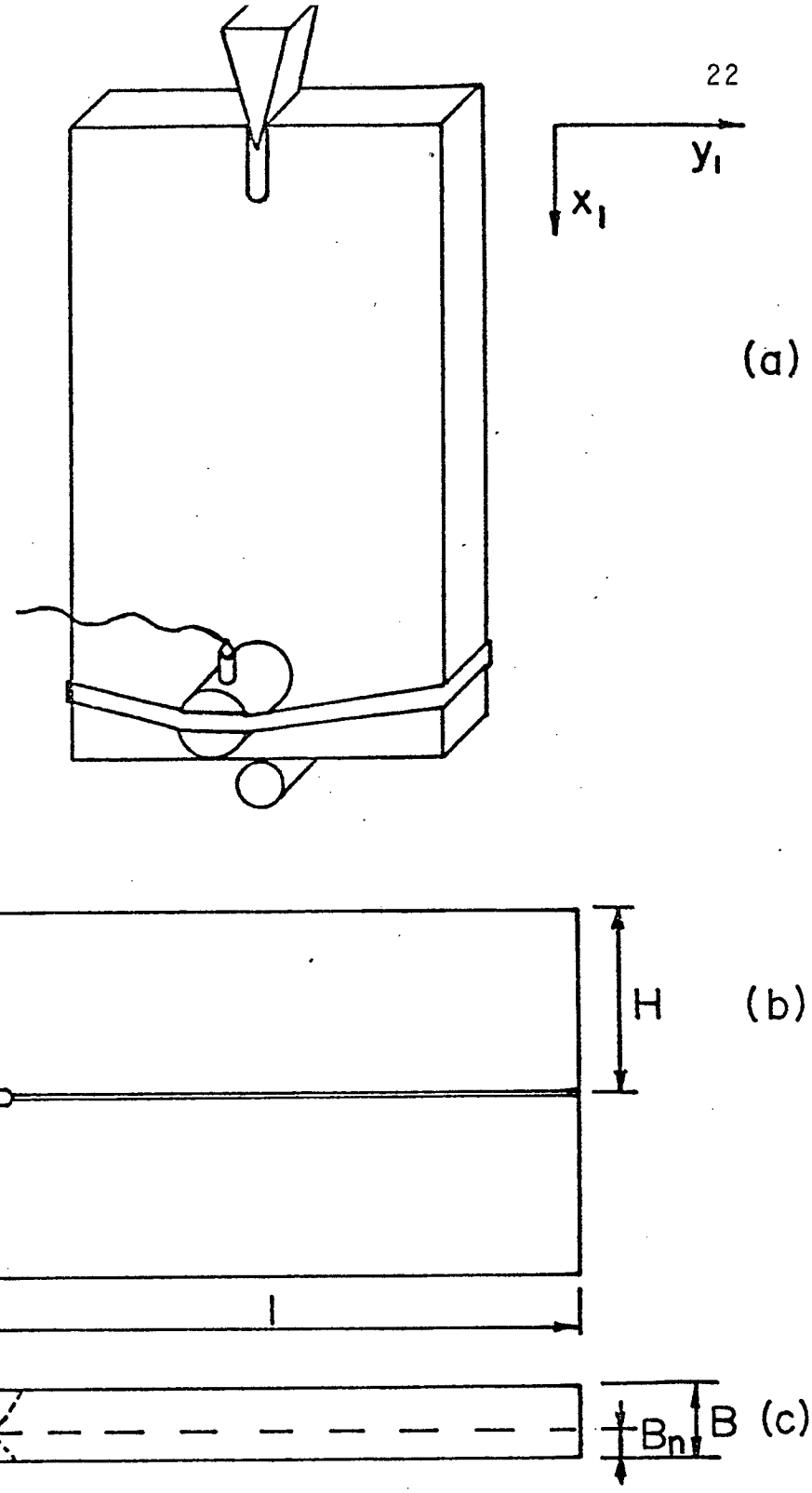

Figure 4. Wedge-loading apparatus and specimen.

(a) Loading fixture, transducer and specimen front-view.
(b) Specimen back-view.
(c) Specimen side-view.

where E is the modulus of elasticity,

P is the load applied to the sample in the direction y_1, (Figure 4),

a is the crack length,

H is the beam width,

B is the beam thickness,

y is the deflection of the two beams in the direction y_1, (Figure 4).

2.3.1.3. Elastic Wave Attenuation

In order to compare the acoustic emission generation of composites of different filler content and sizes, it was necessary to know the effect of particle volume fraction on attenuation. The alumina particles might change the attenuation of epoxy either by increasing the scatter of the waves or by improving the propagation of the waves*. Therefore, the measurement of attenuation was carried out on every sample, prior to the fracture test.

In some tests an AE source (pulser) was fixed at one end of an epoxy composite specimen measuring 22.0 cm x 3.7 cm x 1.3 cm, while a transducer was placed at the other end (Fig. 5a).

* During these experiments it was found that glass had much less attenuation than epoxy

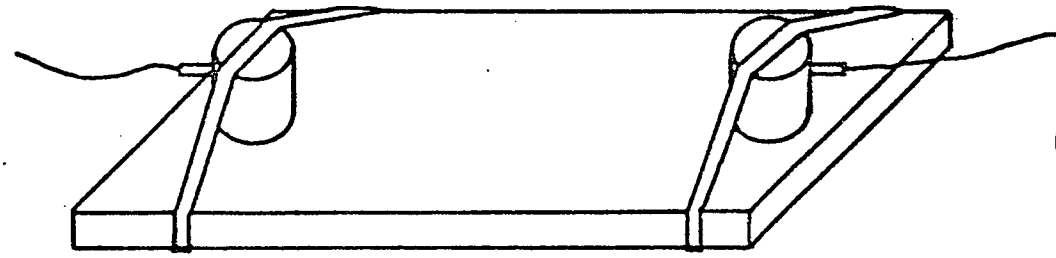

(a).

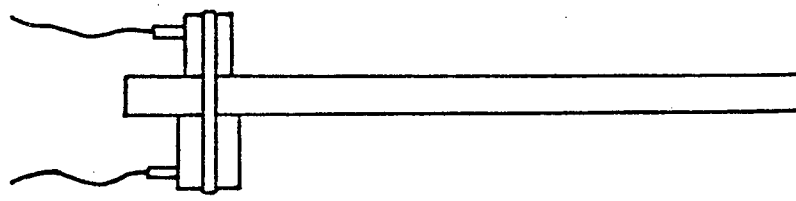

(b).

Figure 5. Pulser attenuation tests.

(a) Test for attenuation versus distance.
(b) Front-to-front attenuation test.

AE counts were accumulated for periods of one minute of pulsing. Then, the distance between the transducer and the pulser was reduced in 2.5 cm decrements until the two were in contact. The same test was done for a glass sample of 22.0 cm x 3.7 cm x 0.6 cm for a pulsing period of five minutes.

A second type of test was conducted with the pulser and the transducer placed front to front, separated by the sample thickness (Fig. 5b).

The equipment used for the attenuation tests was:

(i) Pulser - 908 Dunegan/Endevco
(ii) Wide band transducer, sensitive in the frequency range 0.2 - 0.8 MHz - D 9201 D/E
(iii) Preamplifier
(iv) Filter
(v) Post-amplifier
(vi) Ring-down counter
(vii) Plotter
(viii) Test pulse generator

Items (iv) through (vi) were contained in the Dunegan Endevco 301 Totalizer. Item (viii) was contained in the Dunegan

Endevco 920 distribution analyzer. The functions of items (ii) through (vi) were explained in Section 1.1. The test generator gives a pulse of +5 volts which is transformed into a burst of stress waves through the pulser. The pulser in itself is a transducer.

A total gain of 95 dB was used. Signals which were not in the 0.1 - 0.3 MHz range were filtered. A threshold voltage of 1 volt was fixed. The gain, frequency range, and threshold voltage were kept constant.

2.3.2. Fracture Tests

2.3.2.1. Double Torsion Specimens

Initially, one of the objectives of this study was to correlate acoustic emission rates to the values of stress intensity in slow crack growth tests. Double torsion tests were chosen because of their simple geometry (Fig. 6) and because of the independence of stress intensity (K) on the crack length for this sample. The standard stress intensity equation is the following[20]:

$$K = Pw_m\left(\frac{3(1+\nu)}{WB^3B_n}\right)^{1/2} \qquad (17)$$

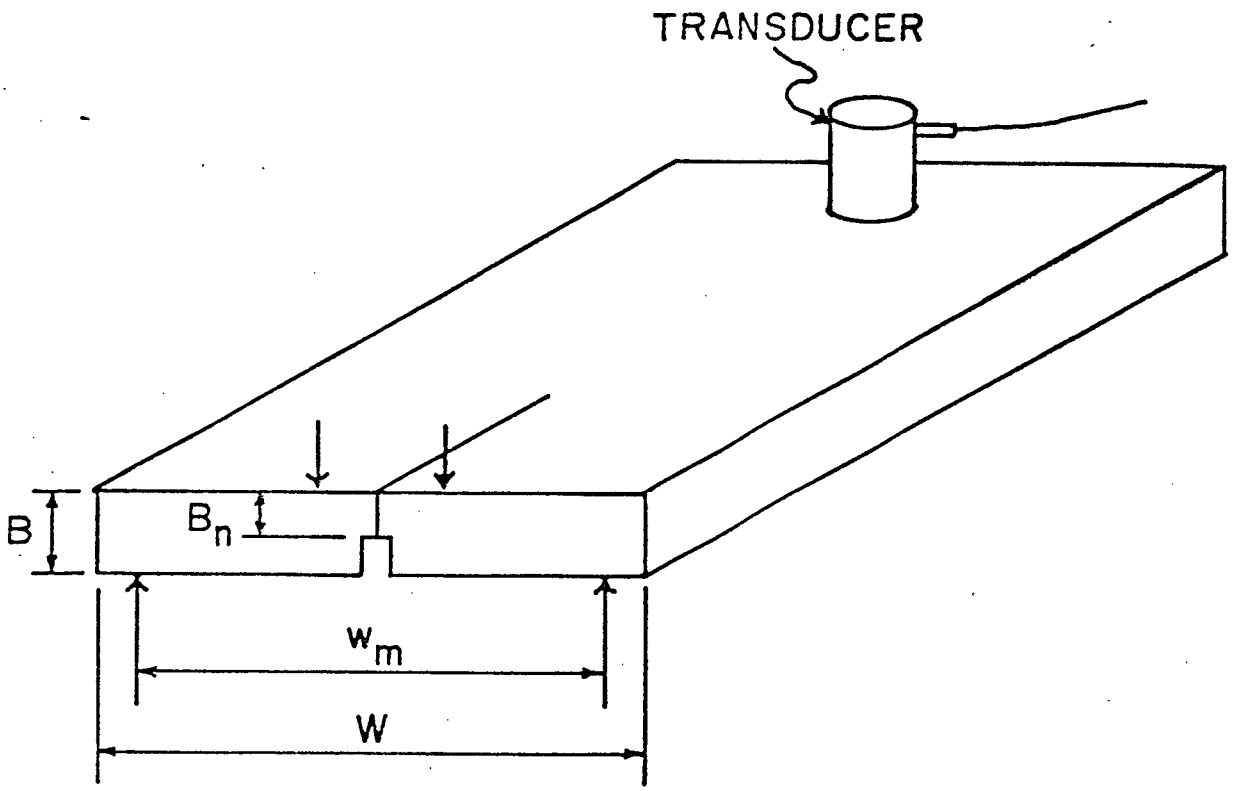

Figure 6. Double torsion specimen and loading points.

where $P/2$ is the total load applied to one bar,

w_m is the moment arm,

$W/2$ is the bar width,

B is the bar thickness,

B_n is the slab thickness in the plane of the crack,

ν is Poisson's ratio.

Two methods were used to measure crack speeds in double torsion tests:

(i) The load relaxation method, where the crosshead displacement is kept constant while the crack is propagating.

(ii) The constant load method, where the crosshead speed is kept constant while the crack is propagating.

The compliance of double torsion specimens can be expressed with the following equation[21]:

$$y = P(B_c a + C_c) \tag{18}$$

where B_c and C_c are constants that depend on the elastic modulus of the test material and the dimensions of the specimen

and test device. Differentiating with respect to time yields the following equation:

$$\frac{dy}{dt} = (B_c a + C_c) \frac{dP}{dt} + B_c P \frac{da}{dt} \tag{19}$$

Thus, for the load relaxation method, the crack speed can be expressed as:

$$\frac{da}{dt} = - \frac{a_i P_i}{P^2} \left(\frac{dP}{dt}\right) \tag{20}$$

where a_i is the crack length and P_i is the load at the onset of relaxation. For the constant load method, the crack speed is given by the following equation:

$$\frac{da}{dt} = \frac{dy}{dt} \frac{1}{B_c P} \tag{21}$$

Procedure: Particle-filled epoxy slabs of 22.0 cm x 7.6 cm x 1.3 cm were grooved through the half width with a thin diamond saw. A notch of 2.5 cm depth was also cut with the diamond saw along the same direction as the groove (Fig. 6). A small crack was initiated by pressing a razor blade to the bottom of the notch. The double torsion fixture used is illustrated in Figure 6. The crosshead speed for the experiments was 5.08×10^{-3} cm/min.

Several problems were encountered while carrying out double torsion tests. One was the difficulty in locating the crack along the specimen, since the material was not transparent. A second difficulty was encountered when the cracks wandered from the guiding grooves; in this case the formula for calculating stress intensity could not be applied. Because of these problems, the double torsion tests were abandoned and a wedge-loading method was adopted.

2.3.2.2. Wedge-Loading Specimens

A double cantilever beam specimen was placed between a wedge and a supporting rod, which was attached to a compression load cell contained in an Instron testing machine (Fig. 4). The wedge moved into the notch during the test. A wedge of 30° was chosen, as suggested by the work of Hoagland et al[22]. The specimens here were the uncracked arms of samples used for double torsion tests. Epoxy rectangular slabs of 22.0 cm x 3.7 cm x 1.3 cm were grooved 2/3 of their total thickness. The groove made with a thin diamond saw ran along the axis of the beam. At one end of the groove a notch of approximately 3.5 cm was cut with a thick diamond saw (Fig. 4). At the bottom of the notch a crack was initiated with a razor blade. The sides of the notch were levelled in order to allow better contact with the wedge.

The analytical expression for the fracture toughness of wedge loading tests was developed as follows:

$$E = \frac{8a^3P}{H^3By} \tag{16}$$

and

$$C = \frac{y}{P} \tag{22}$$

Fracture energy, G , is given by equation (23)[23].

$$G = \frac{P^2}{2B_n}\left(\frac{\partial C}{\partial a}\right) \tag{23}$$

Substituting (16) and (22) in (23)

$$G = \frac{12P^2a^2}{H^3BB_nE} \tag{24}$$

If it is assumed that the factor $(1-\nu^2)^{-1/2}$ is approximately one, the stress intensity, K, is related to G by equation (25)

$$K \simeq \sqrt{GE} \tag{25}$$

Therefore,

$$K = \frac{2\sqrt{3}\ aP}{(H^3BB_n)^{1/2}} \tag{26}$$

Since the stress intensity is a function of crack length, careful measurement of the crack length was required. To locate the crack in the specimen, the side opposite the groove was coated with a layer of black, water-proof ink.

The sample was loaded as the wedge travelled at a constant speed of 5.08×10^{-3} cm/min. The graph of load vs. time was recorded. When the crack propagated, the load dropped; the position of the crack on the specimen and the local maximum load on the chart were labelled after crack propagation with the same number (i). The testing continued until the sample was completely broken. A sample of the data obtained for these tests is in Appendix I.

2.3.2.3. Three-Point Bending Tests

These tests were done in order to confirm the toughness values obtained in the wedge-loading experiments.

The rectangular samples of 10.5 cm x 1.4 cm x 1.3 cm were cut from epoxy slabs with a thin diamond saw. A notch of 50% of the total thickness was made and a crack was initiated by pressing a razor blade into the bottom of the notch. A three-point bending fixture was attached to a compressive load cell on the Instron (Fig. 7).

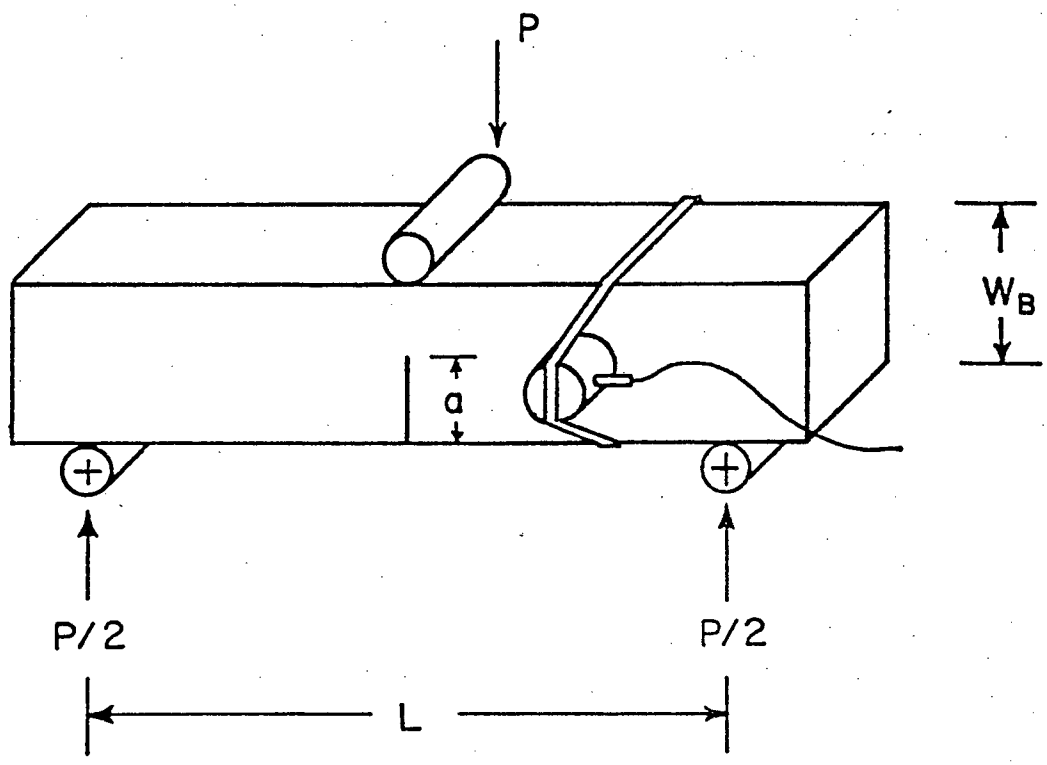

Figure 7. Three-point bending specimen and loading points.

Some of the samples exhibited slow crack growth during these tests (the crack stopped before propagating through the whole specimen). In these cases, the maximum load was recorded. The toughness for these samples is given by the following equations[23]:

$$K = \frac{3YPL\sqrt{\pi a}}{2 B_n W_B^2} \tag{27}$$

$$Y(L/W_B = 8) = 1.107 - 2.120(a/W_B) + 7.71(a/W_B)^2 - 13.5(a/W_B)^3 + 14.25(a/W_B)^4 \tag{28}$$

where $L/2$ is the distance between loading points,

W_B is the sample width and

Y is a parameter dependent on the specimen dimensions.

2.3.2.4. Compliance Calibration

2.3.2.4.1. Double Torsion Specimens

Calibrating a specimen consists of relating the deflection per unit load to the crack length of the sample and comparing the measurements to the standard equation. It was performed to verify whether the equations developed analytically for double torsion tests (Section 2.3.2.1.) were applicable for the experiments carried out in this study. Once the compliance calibration had been completed, the fracture energy and toughness could be calculated using Equations 23 and 25. Compliance calibration also permits the calculation of crack velocities for these samples.

In order to perform compliance measurements, a notched ("cracked") sample was loaded and the graphs of deflection vs. time and load vs. time were recorded for a particular crack length. Then, the length of the notch was increased and this process was repeated until the length of the notch was 2/3 of the total length of the specimen. After obtaining the compliance for six different crack lengths, the sample was considered calibrated. For each notch length, using linear regression analysis, the relation of deflection and load was approximated as a linear function. The slope of the line was the compliance of the sample for the particular notch length. Graphs were made with the compliance plotted as a function of the crack length.

The deflection of the sample was measured with a linear voltage differential transducer (LVDT). Deflections of loads up to 534 N were recorded for the different notch lengths tested. The notches were made with a thin diamond saw.

2.3.2.4.2. Wedge-Loading Specimens

Compliance calibration of wedge-loading specimens was performed for the same reasons it was carried out for double torsion samples. The compliance test made possible the calibration of grooved specimens when the analytical solution

was difficult. Once the calibration was done, using the elastic modulus of the material, fracture toughness was calculated.

Procedure: Two cross-marks were made on the sample with a razor blade. While the fracture test was being conducted and the wedge penetrated the notch, the deflections of the cross-marks were measured using a travelling microscope. After the crack was located and marked on the specimen, the Instron crosshead was stopped and the load and deflection were recorded. The method of obtaining compliance vs. crack length graphs was the same as in Section 2.3.2.4.1.

The compliance of a sample with a crack length of 2.5 cm was obtained with and without a groove to measure the effects of the side groove on the calibration.

2.3.3. Acoustic Emission Tests

A D 9201 A D/E transducer was attached to the double torsion, wedge-loading, and three-point bending specimens while performing fracture tests (Figs. 4, 6 and 7). Teflon tape was wrapped around the samples and/or fixture where there was contact between the specimens and the fixture. A total gain of 95 dB was used. Signals which were not

in the 0.1 - 0.3 MHz range were filtered out. A threshold voltage of 1 volt was fixed. The gain, frequency range, and threshold voltage were kept constant for every fracture test. Graphs of acoustic emission vs. time were recorded on the charts attached to the acoustic emission equipment. In the wedge-loading tests, after crack propagation the same number (i) was used to designate:

a) the AE counts on the AE vs. time chart,
b) the local maximum load on the load vs. time chart,
c) the position of the crack on the specimen.

2.4. Tests on Steel Composites

2.4.1. Fracture Tests

Milling machines could not be used for producing samples from the steel composite slabs because the alumina in the material caused severe tool wear. Three-point bending specimens were chosen because of their simple preparation, involving a minimum amount of cutting. Also, the hot-rolled slabs yielded a maximum number of specimens when beams were used. The samples were cut into pieces of 7.5 cm x 0.6 cm x 0.25 cm, using a thin diamond saw at a speed of 10^{-3} m/min.

In order to estimate the austenizing temperature of the composite, its carbon content was determined using a Leco Analyzer. Carbon contents were found to be in the range 0.52 - 0.66. The samples were surface-ground to eliminate surface scales. To get a homogeneous martensitic matrix, the specimens were austenized at 860°C and water-quenched. Grooves of 50% depth were made on the sample (Fig. 7). A three-point bending fixture, attached to a compressive load cell on the Instron, was used. A cross-head speed of 5.08×10^{-3} cm/min was maintained to break the samples. The maximum loads were recorded. Equations 27 and 28 were used to calculate the fracture toughness.

In order to test the consolidation of the iron powders during hot forging and hot rolling, one of the samples was broken by impact at liquid nitrogen temperatures.

Some of the specimens were coated with gold to aid in examining the fracture surface using the Scanning Electron Microscope and the X-ray energy dispersive analyzer.

2.4.2. Acoustic Emission Tests

A D 140 B D/E transducer was fastened to one side of the sample (Fig. 7) using the device shown in Fig. 8. The

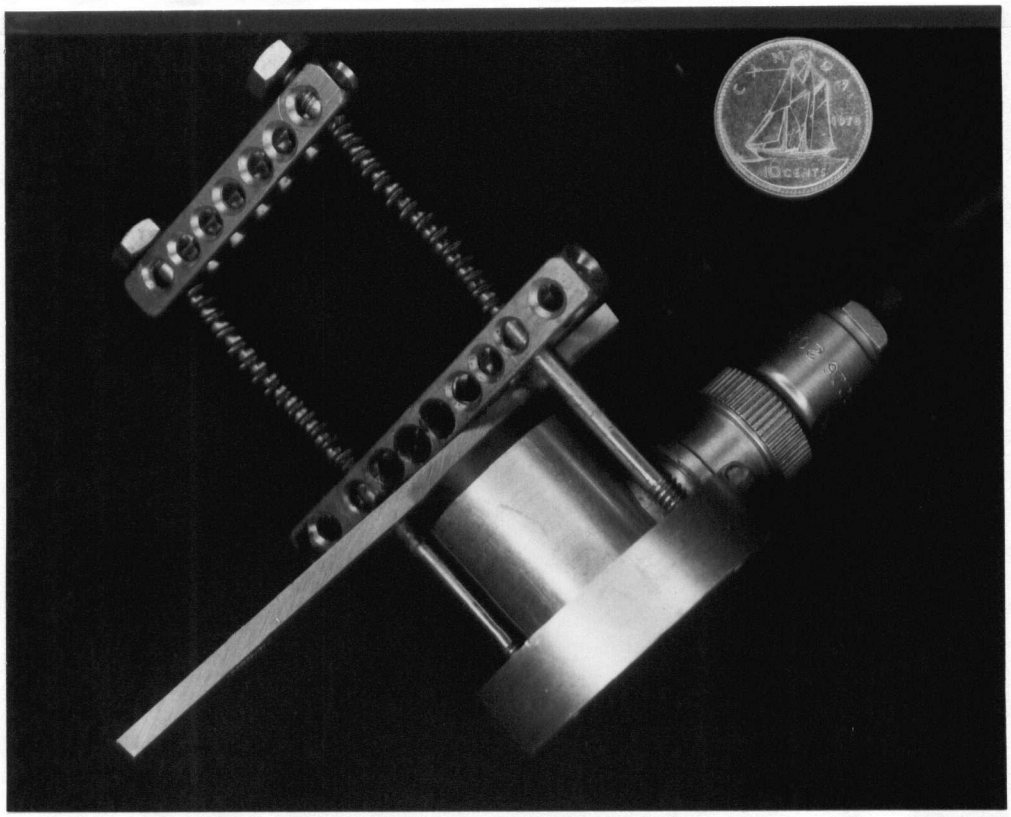

Figure 8. Fixture used for attaching transducer to martensitic steel composite specimens.

gain, frequency range, and threshold voltage used were the same as described in Section 2.3.3.

3. RESULTS AND CALCULATIONS

The results and the trends of the data obtained from the tests conducted in the study are reported in this chapter. The order followed for presenting the data is similar to that followed for describing the experimental procedure.

The results and calculations from the experiments on epoxy composites were divided into three categories:

1) Material characterization.
2) Fracture data.
3) Acoustic emission data.

Only fracture and AE results were presented for the martensitic steel composites.

3.1. Tests on Epoxy Composites

3.1.1. Material Characterization

3.1.1.1. Density and Particle Volume Fraction Determination

The densities and particle volume fractions of the fractured samples are listed in Table I. The density of alumina was determined as 3.990 g/cm^3 using pycnometers.

TABLE I

Densities and Volume Fractions of Alumina-Filled Epoxy Specimens

Average[+] Alumina Particle Size (μm)	Density (gr/cm^3)	Alumina Volume Fraction
-	1.22	0.000
-	1.22	0.000
40	1.24	0.006
"	1.48	0.090
"	1.76	0.128
50	1.26	0.013
"	1.29	0.025
"	1.32	0.037
"	1.45	0.087
"	1.58	0.132
"	1.61	0.140
65	1.33	0.038
"	1.34	0.042
"	1.35	0.045
"	1.44	0.077
"	1.45	0.083
"	1.48	0.093
"	1.55	0.121
"	1.56	0.124
"	1.58	1.130
"	1.75	0.191
"	1.76	0.194
"	1.77	0.200
"	2.00	0.288
"	2.01	0.288
"	2.01	0.287
"	2.14	0.337
"	2.14	0.336
90	1.24	0.007
"	1.34	0.042
"	1.58	0.134
"	1.74	0.189
"	1.75	0.195
"	1.85	0.230
"	2.08	0.314
"	2.17	0.378
115	1.27	0.096
"	1.30	0.025
"	1.44	0.076
"	1.47	0.093
128	1.44	0.078
"	1.51	0.106
137	1.23	0.001
"	1.23	0.003
"	1.28	0.021
"	1.29	0.025
"	1.31	0.031
"	1.32	0.034
"	1.73	0.186
"	1.93	0.258
"	1.93	0.260
"	2.00	0.281
"	2.07	0.309
"	2.44	0.444
"	2.59	0.499

+ The average alumina particle size was obtained by averaging the highest and lowest particle size in a determined range.

The density of the composites, as expected, increased with increasing alumina volume fraction. The density of bubble-free material (ρ_I) was then calculated according to:

$$\rho_I = V_f\rho_A + (1 - V_f)\rho_E \tag{29}$$

and was found to be in agreement with the measured values to the second decimal place. Therefore, it appears that the material was bubble-free. Fracture surface analysis confirmed this observation.

3.1.1.2. Elastic Constants

The compliance (C) of wedge-loaded specimens is a cubic function of the crack length (a):

$$\frac{y}{P} = \frac{8a^3}{BH^3E} \tag{16}$$

and

$$\frac{y}{P} = C \tag{22}$$

Therefore,

$$C = \frac{8a^3}{BH^3E} \tag{30}$$

The program P:2R of the Biomedical Computer Programs P-series, which utilizes linear regression analysis, was used in order

to obtain a linear function between the measured compliance and a^3.

$$C = \alpha_4 a^3 + b \tag{31}$$

The values of b were negligible, thus

$$C = \alpha_4 a^3 \tag{32}$$

it follows that

$$E = \frac{8}{H^3 B \alpha_4} \tag{33}$$

The elastic moduli (as calculated from Equation 33) for composites of different particle sizes and filler volume fractions are listed in Table II. Figure 9 compares these results with theoretical predictions for these composites. This topic will be dealt with in detail in Chapter 4.

The elastic modulus increased with the alumina volume fraction, but it was independent of particle size (Fig. 9). The same trends have been observed by other investigators[24,25,26]. A scatter band of elastic modulus values can be observed (Fig. 9).

TABLE II

Elastic Constants of Alumina-Filled Epoxy Specimens

Average Alumina Particle Size (μm)	Volume Fraction of Alumina	Elastic Modulus (GPa)
-	0.000	4.344
50	0.013	4.409
"	0.025	5.428
"	0.037	3.677
"	0.087	3.726
"	0.132	5.345
"	0.140	8.975
65	0.038	2.568
"	0.083	5.740
"	0.121	6.995
"	0.194	4.539
"	0.287	11.649
"	0.337	10.775
90	0.007	4.762
"	0.042	2.320
"	0.134	4.720
"	0.189	4.628
"	0.195	5.842
"	0.230	6.738
"	0.314	8.744
"	0.378	9.733
115	0.010	3.873
"	0.025	4.397
"	0.076	4.090
"	0.093	5.707
128	0.078	4.324
"	0.106	3.502
137	0.003	4.153
"	0.021	5.739
"	0.025	4.305
"	0.186	6.487
"	0.258	7.337
"	0.260	7.831
"	0.444	12.559

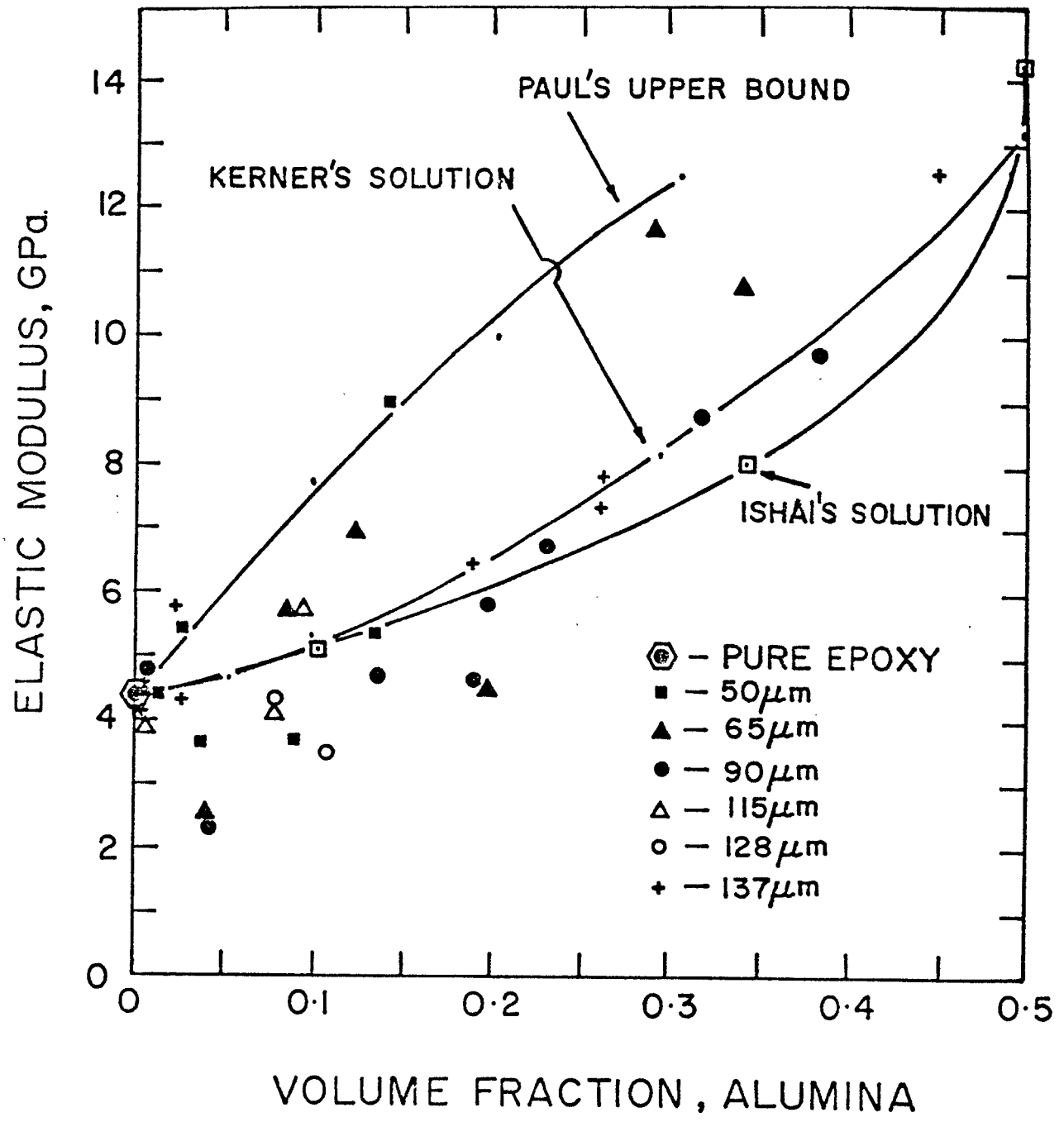

Figure 9. Elastic constants of alumina-filled epoxy compared to theoretical predictions.

3.1.1.3. Elastic Wave Attenuation

The graph of AE counts versus the transducer to pulser distance for epoxy and glass is shown in Figure 10. Epoxy has a much greater inherent attenuation than glass, but the attenuation is relatively insensitive to the distance between source and detector. The shape of the curve is about the same in both cases and other tests indicated that it is sensitive to the shape of the specimen. To interpret the results, the graph was approximated to a linear function, applying linear regression analysis. A graph of such a function is illustrated in Figure 10. The linear equations are listed in Table III. The effect of the volume fraction and particle size of alumina on the calculated slope and on the y intercept is illustrated in Figures 11 and 12, respectively. A significant decrease in the slope of the lines was observed as the alumina volume fraction increased. However, there is no apparent effect of particle size on the slope. The y intercept seems to be independent of the volume fraction and the particle size of the alumina.

The results of front-to-front attenuation tests are summarized in Table III and illustrated in Figure 13. In these tests, the number of counts appears to be independent of the volume fraction and the particle size of alumina. The

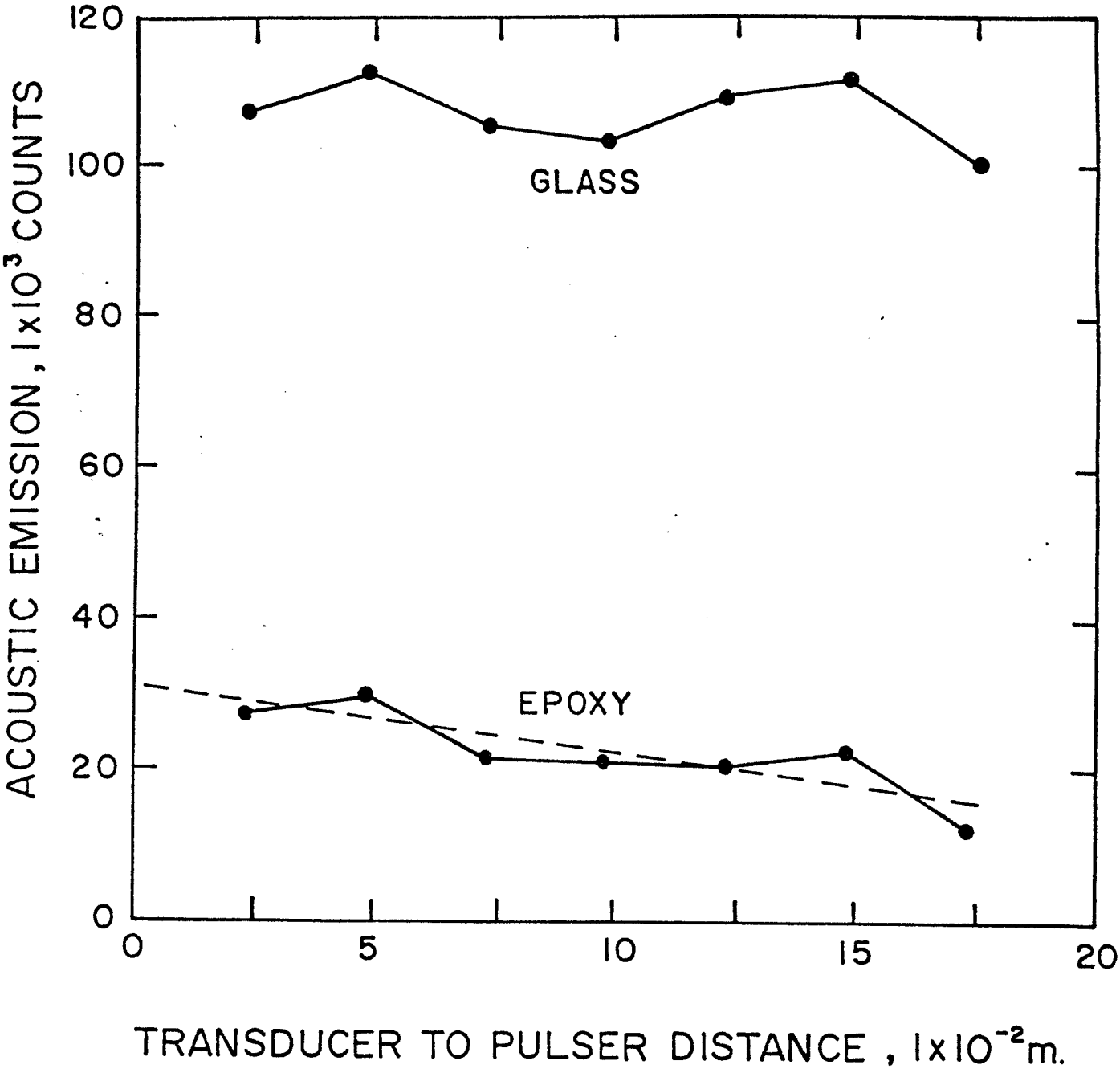

Figure 10. AE counts versus transducer to pulser distance for epoxy and glass.

TABLE III

Linear Equations for Counts Versus Distance Pulser Tests

and Results from Front-to-Front Attenuation Tests

Average Alumina Particle Size (μm)	Volume Fraction of Alumina	Linear Regression Analysis Equations AE = SLO · d + y_{INT} (counts)	Correlation Coefficient r	Results of Front to Front Attenuation Tests (counts)
-	0.000	-22140 x d + 3500.	0.96	3500.
50	0.013	-21280 x d + 3700.	0.98	3260.
"	0.025	-18240 x d + 2860.	0.99	3820.
"	0.037	-20470 x d + 3470.	0.95	2800.
"	0.087	-26780 x d + 3560.	0.97	3000.
"	0.132	-19280 x d + 3250.	0.99	3550.
"	0.140	-13890 x d + 3430.	0.98	3900.
65	0.038	-19660 x d + 3640.	0.92	3000.
"	0.083	-28840 x d + 4420.	0.88	3630.
"	0.121	-24860 x d + 3630.	0.98	3860.
"	0.194	-11090 x d + 2900.	0.95	3280.
"	0.287	-15150 x d + 3830.	0.99	3260.
"	0.337	-12700 x d + 3100.	0.91	3220.
90	0.007	-22430 x d + 3650.	0.98	3100.
"	0.042	-22350 x d + 3460.	0.98	2790.
"	0.134	-21620 x d + 3360.	0.98	3210.
"	0.189	-13340 x d + 3510.	0.93	4410.
"	0.195	-12160 x d + 3030.	0.88	3870.
"	0.230	-15420 x d + 3510.	0.92	4130.
"	0.314	-15570 x d + 3150.	0.96	2640.
"	0.378	- 8070 x d + 3100.	0.86	3280.
115	0.010	-26790 x d + 3970.	0.94	3390.
"	0.025	-25740 x d + 4190.	0.96	3280.
"	0.076	-18750 x d + 3150.	0.97	3690.
"	0.093	-23290 x d + 3590.	0.97	3580.
128	0.078	-21030 x d + 3560.	0.98	3530.
"	0.106	-19210 x d + 3050.	0.96	3100.
137	0.003	-17890 x d + 3690.	0.88	3260.
"	0.021	-18880 x d + 3010.	0.95	3470.
"	0.025	-20080 x d + 3370.	0.99	2780.
"	0.186	-15370 x d + 3900.	0.90	3360.
"	0.258	-13580 x d + 3340.	0.96	4070.
"	0.260	-18580 x d + 3620.	0.94	3530.
"	0.444	-11640 x d + 3520.	0.85	3420.

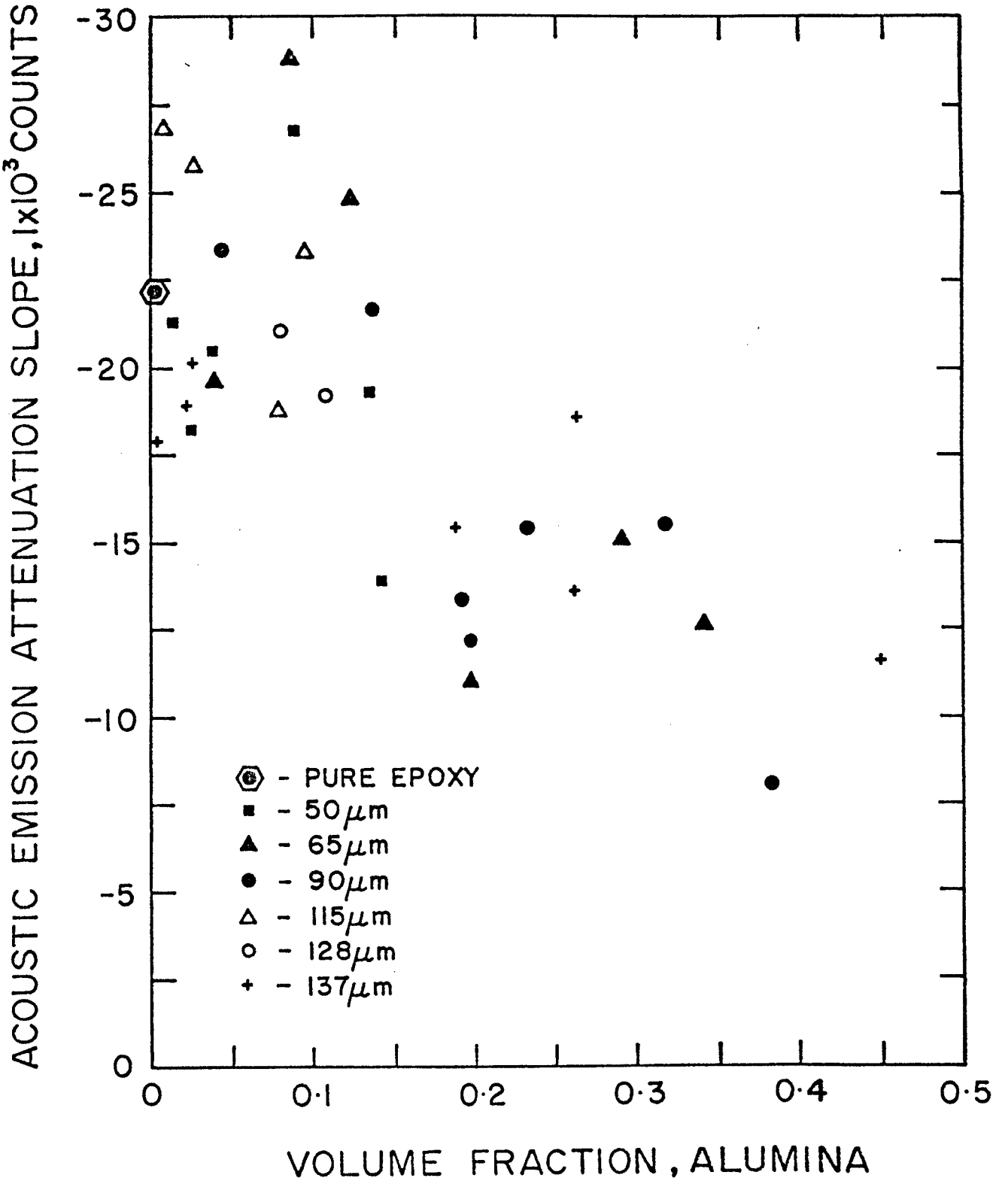

Figure 11. Effect of alumina volume fraction and particle size on the slope of attenuation lines.

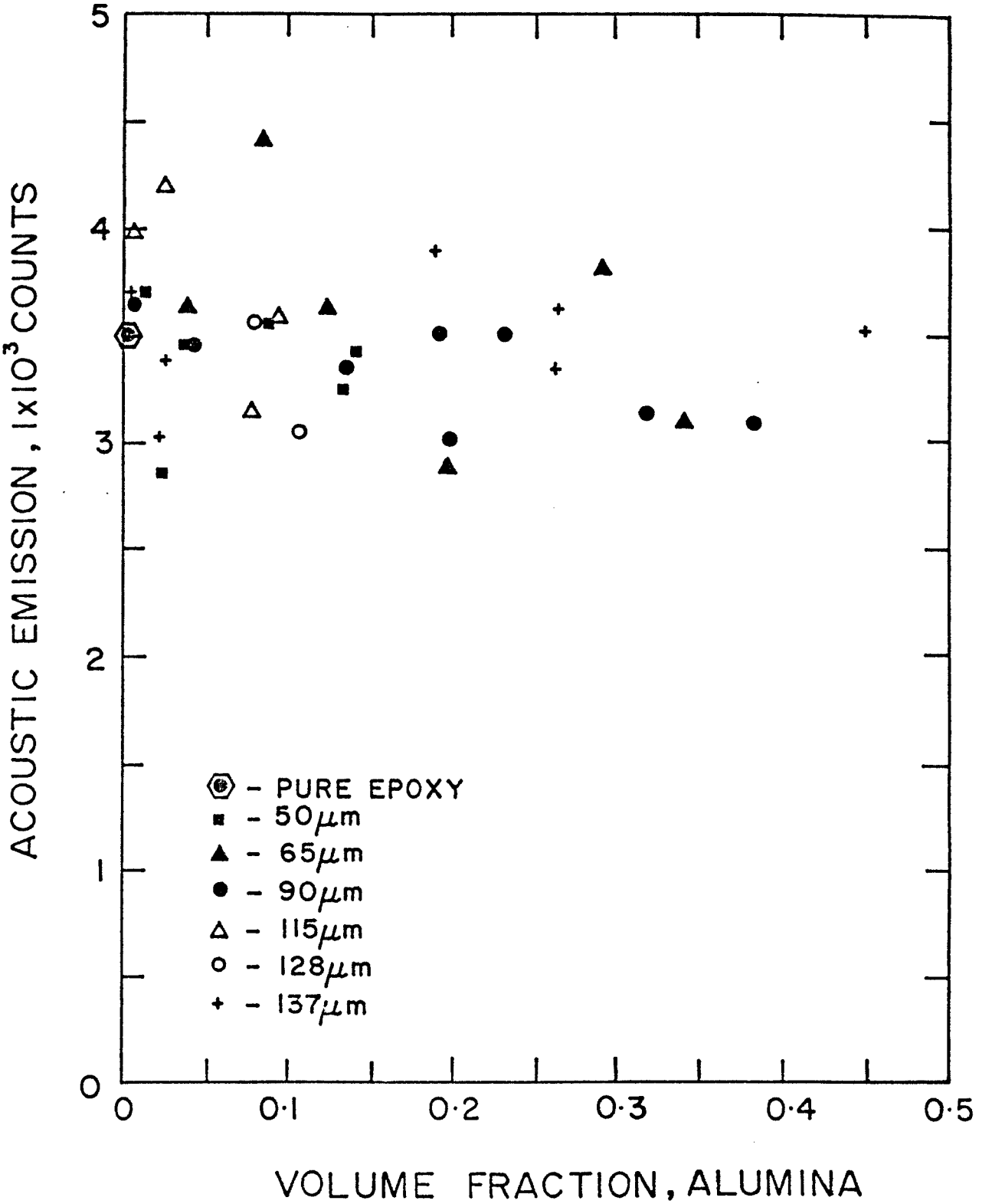

Figure 12. Effect of alumina volume fraction and particle size on the y intercept of attenuation lines.

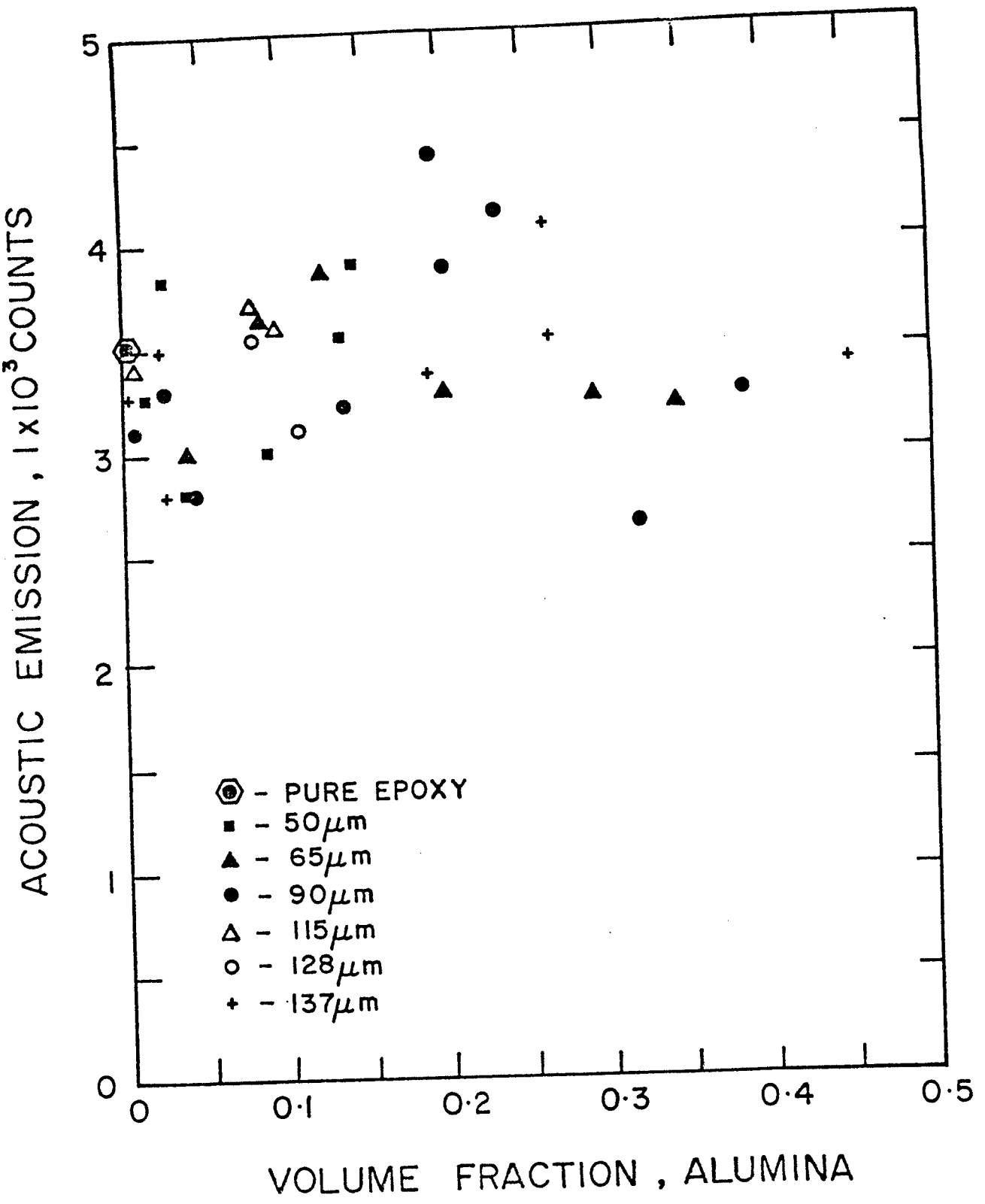

Figure 13. Effect of alumina volume fraction and particle size on counts in front-to-front attenuation tests.

number of counts in front-to-front tests fell within the same range of values as the y intercept in Table III. This seems to indicate that for short distances the differences in attenuation for different microstructures are not large enough to be detected with the testing equipment.

3.1.2. Fracture Tests

3.1.2.1. Double Torsion Tests

The epoxy and the composites tested did not exhibit slow crack growth. Very few toughness values were obtained in the double torsion tests because of the experimental difficulties which were encountered (Section 2.3.2.1.). A summary is given in Table IV. Thus, no conclusion can be drawn from these tests regarding the effect of particle size and volume fraction on fracture toughness. However, the toughness values from the tests were compared with those obtained from other fracture tests and generally good agreement was found. The double torsion values were also in good agreement with results published by Beaumont and Young[27] for low volume fraction silica-filled epoxy fractured in double torsion tests.

TABLE IV

Fracture Toughness of Epoxy Composites.

Double Torsion Tests

Average Alumina Particle Size (μm)	Volume Fraction of Alumina	Fracture Toughness (MPa√m)
50	0.014	0.84
50	0.025	0.90
90	0.035	1.18
90	0.101	1.23
137	0.014	0.69
137	0.022	0.78

3.1.2.2. Wedge-Loading Tests

Figure 14 shows the load to failure versus time, during wedge-loading tests, for pure epoxy and for two epoxy composites. One of the composites had a volume fraction of 0.45 and an average particle size of 137 μm. The second composite had a volume fraction of 0.34 and an average particle size of 65 μm. The load to failure increased with increasing alumina volume fraction.

Listed in Table V are the experimental fracture energy (G_E) and experimental fracture toughness (K_E) of the different composites fractured in wedge-load testing.

Figure 15 illustrates the effect of volume fraction of alumina on fracture toughness for composites of differing average particle size. Both fracture energy and toughness increased with increasing alumina volume fraction but did not seem to be affected significantly by the average particle size of the alumina.

3.1.2.3. Three-Point Bending Tests

Table VI contains values of fracture toughness for the different specimens used in three-point bending tests. These

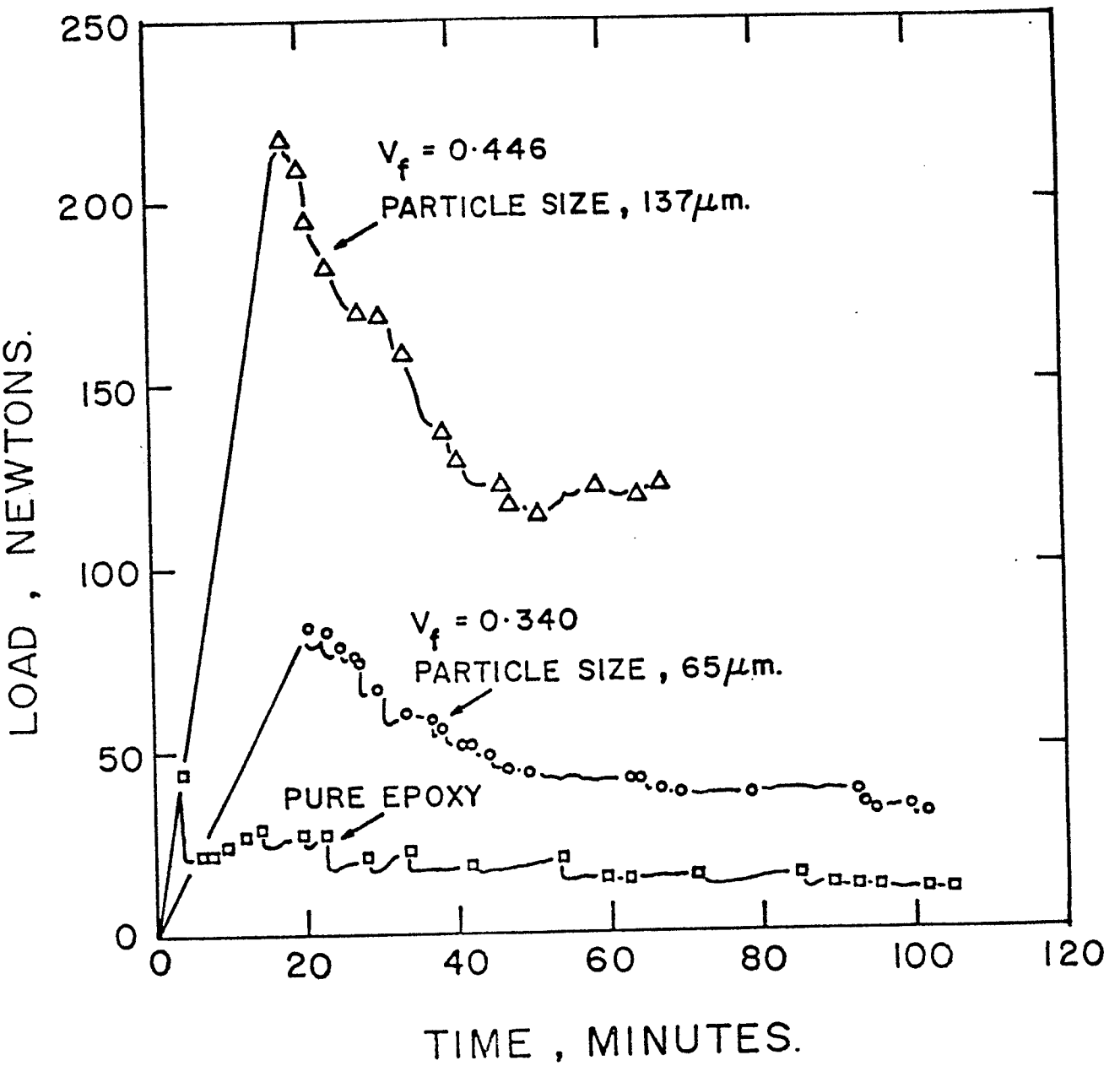

Figure 14. Load versus time curve during wedge-loading test of specimens of different compositions.

TABLE V

Experimental Fracture Energy and Experimental Fracture Toughness of Wedge-Loading Tests

Average Alumina Particle Size (μm)	Alumina Volume Fraction	Average Experimental Fracture Toughness (MPa√m)	Average Fracture Energy G (N/m)
-	0.000	0.97 ± 0.1	220. ± 30.
50	0.013	1.04 ± 0.1	250. ± 50.
"	0.025	1.54 ± 0.1	470. ± 200.
"	0.037	0.97 ± 0.1	260. ± 70.
"	0.087	1.15 ± 0.1	360. ± 90.
"	0.132	1.48 ± 0.1	410. ± 40.
"	0.140	2.33 ± 0.4	620. ± 200.
65	0.038	0.75 ± 0.2	230 ± 100.
"	0.083	1.37 ± 0.1	330. ± 40.
"	0.121	1.89 ± 0.1	590. ± 50.
"	0.194	1.40 ± 0.1	430. ± 70.
"	0.287	3.09 ± 0.2	820. ± 180.
"	0.337	2.83 ± 0.3	750. ± 180.
90	0.007	1.02 ± 0.1	220. ± 50.
"	0.042	0.70 ± 0.1	210. ± 30.
"	0.134	1.31 ± 0.1	370. ± 70.
"	0.189	1.45 ± 0.2	460. ± 70.
"	0.195	1.72 ± 0.1	510. ± 100.
"	0.230	1.66 ± 0.2	410. ± 80.
"	0.314	2.38 ± 0.1	650. ± 90.
"	0.378	2.58 ± 0.2	690. ± 60.
115	0.010	0.79 ± 0.1	160. ± 20.
"	0.025	0.92 ± 0.1	200. ± 70.
"	0.076	1.04 ± 0.1	270. ± 40.
"	0.093	1.36 ± 0.1	330. ± 30.
128	0.078	1.10 ± 0.1	280. ± 50.
"	0.106	1.09 ± 0.1	340. ± 80.
137	0.003	0.69 ± 0.1	120. ± 50.
"	0.021	1.19 ± 0.2	260. ± 100.
"	0.025	0.91 ± 0.1	200. ± 50.
"	0.186	1.50 ± 0.2	350. ± 90.
"	0.258	2.15 ± 0.2	630. ± 160
"	0.260	1.85 ± 0.2	440. ± 90.
"	0.444	3.72 ± 0.3	1110. ± 90.

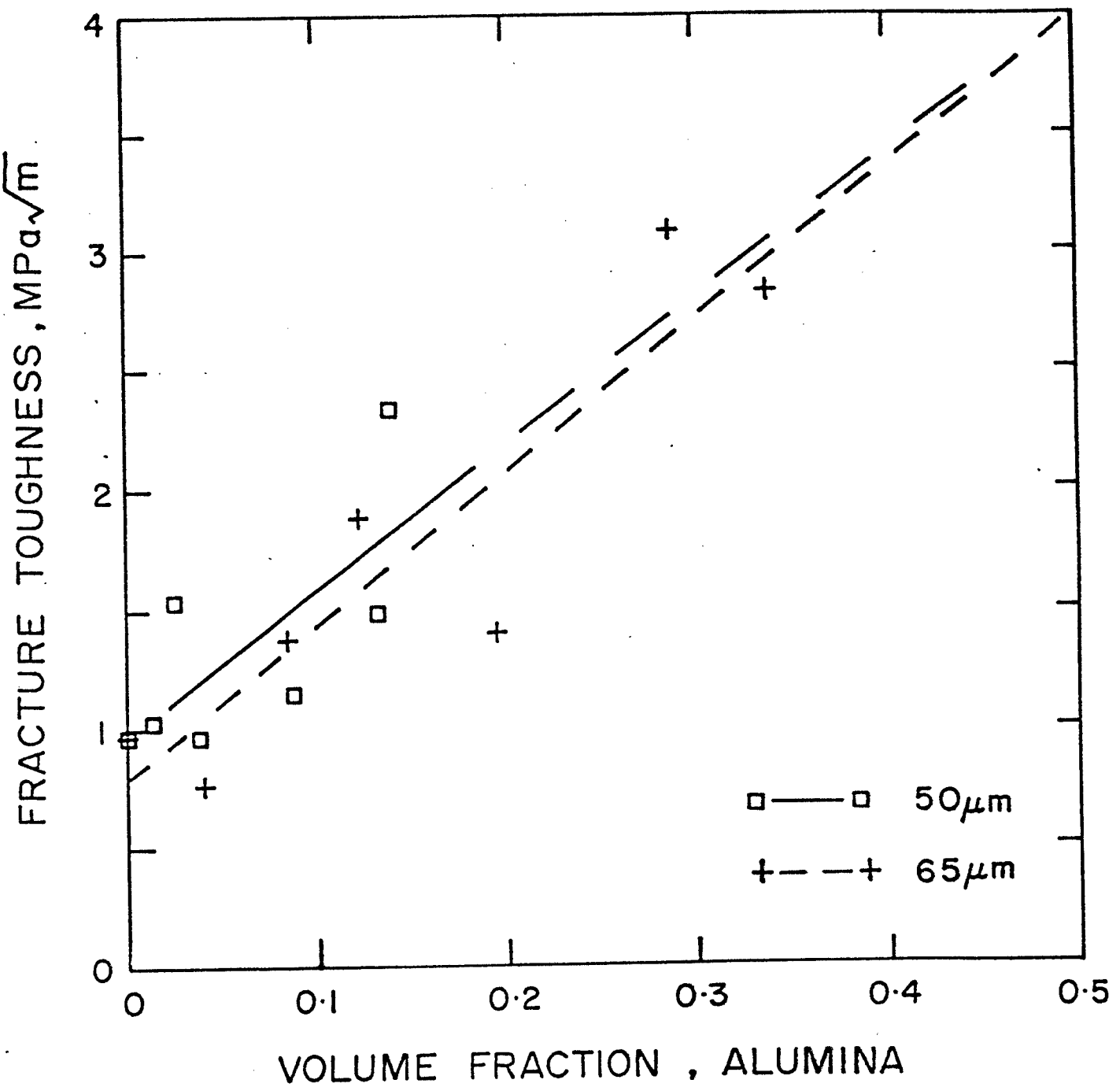

Figure 15a. Effect of alumina volume fraction and particle size on fracture toughness. Wedge-loading tests.

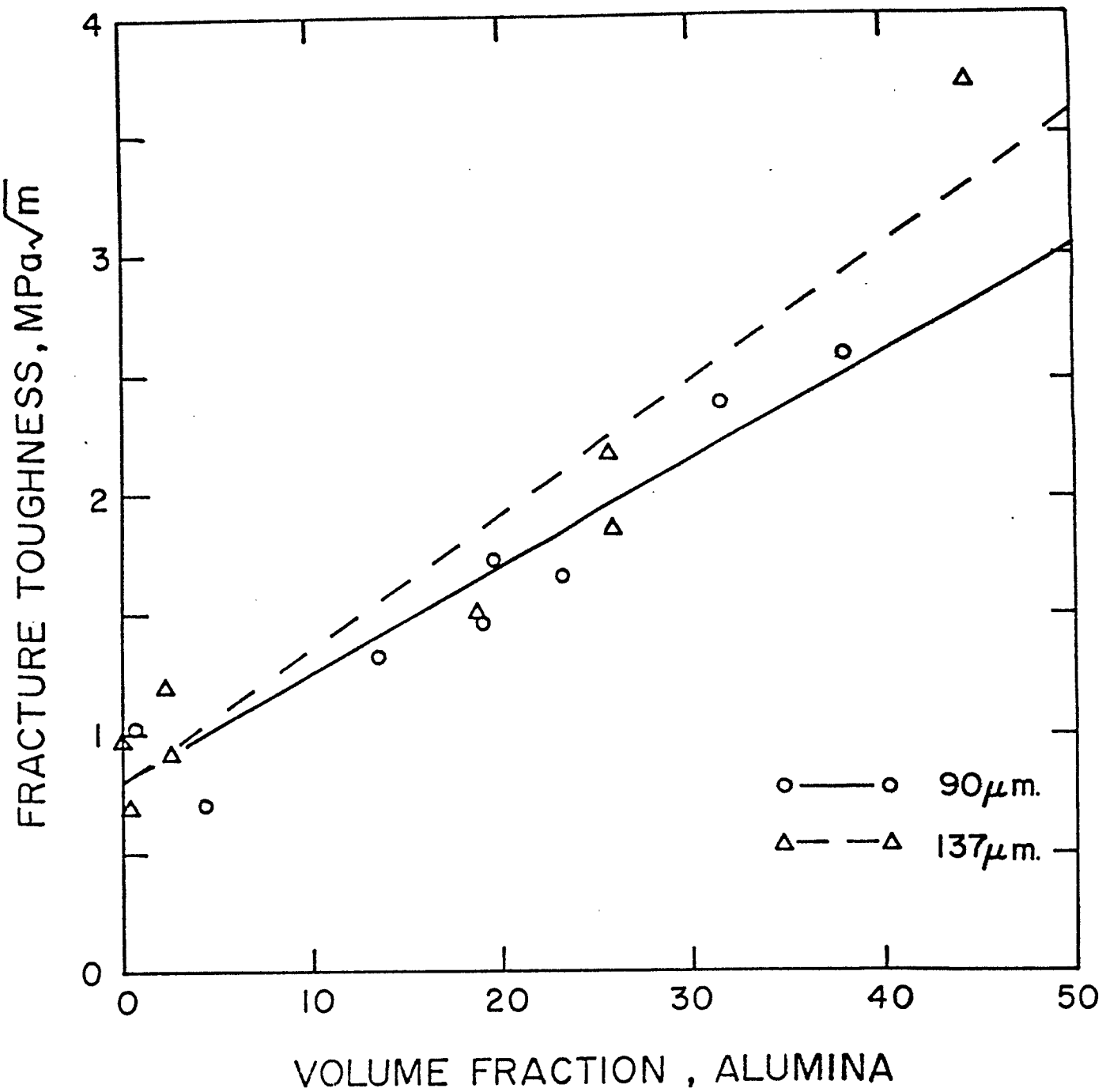

Figure 15b. Effect of alumina volume fraction and particle size on fracture toughness. Wedge-loading tests.

TABLE VI

Fracture Toughness of Epoxy Composites.

Three-Point Bending Tests

Average Alumina Particle Size (μm)	Volume Fraction of Alumina	Fracture Toughness (MPa√m)
-	0.000	0.43
-	0.000	1.03
65	0.042	0.71
"	0.045	1.35
"	0.077	1.12
"	0.093	1.12
"	0.124	1.01
"	0.130	1.54
"	0.201	1.56
"	0.289	1.63
"	0.289	1.42
"	0.333	1.79
137	0.001	0.50
"	0.001	0.89
"	0.031	1.19
"	0.034	0.73
"	0.282	1.35
"	0.310	1.38
"	0.500	1.91

tests, like the wedge-loading tests, showed that the toughness increased with alumina volume fraction and that it was not significantly affected by particle size. Fracture toughness versus alumina volume fraction for wedge-loading and three-point bending tests is shown in Figure 16 for specimens with an average particle size of 64 μm. Figure 17 presents the result for material with an average particle size of 137 μm for double torsion, wedge-loading and three-point bending tests. The different types of loading tests yielded very similar fracture toughness values for low alumina volume fractions. At high volume fractions, where subcritical crack growth was observed in three-point bending tests, wedge-loading tests yielded higher toughness values. No satisfactory explanation was found for the disagreement between the toughness values resulting from wedge-loading and three-point bending tests.

3.1.2.4. Compliance Calibration

3.1.2.4.1. Double Torsion Specimens

A summary of the compliance calibration results for double torsion specimens is given in Table VII. Experimental and calculated compliance values versus notch length are illustrated in Figure 18. Experimental and calculated compliance values are linear functions of notch length, as expected for a constant moment specimen. The calculated

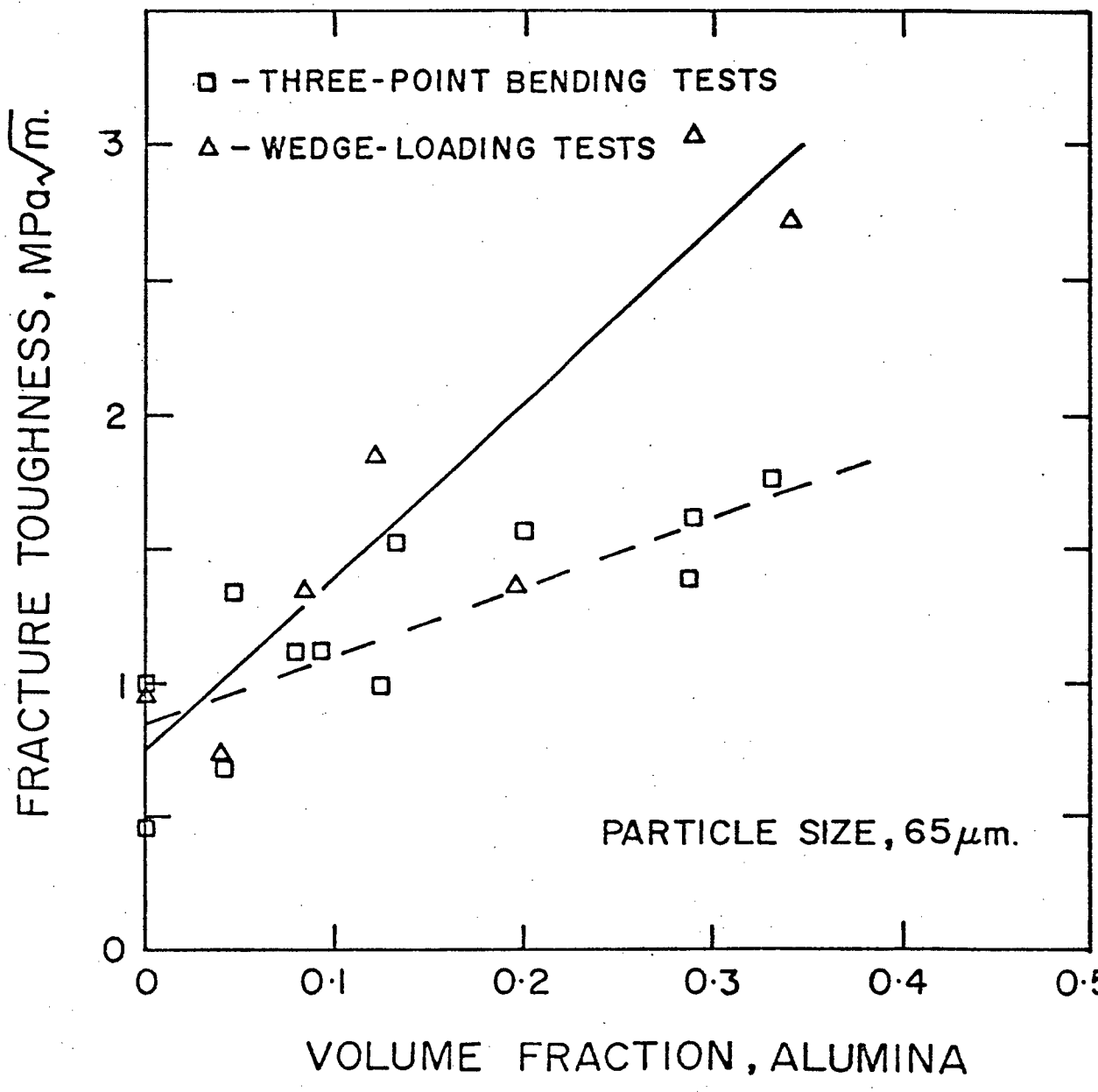

Figure 16. Fracture toughness versus volume fraction. Wedge-loading and three-point bending tests.

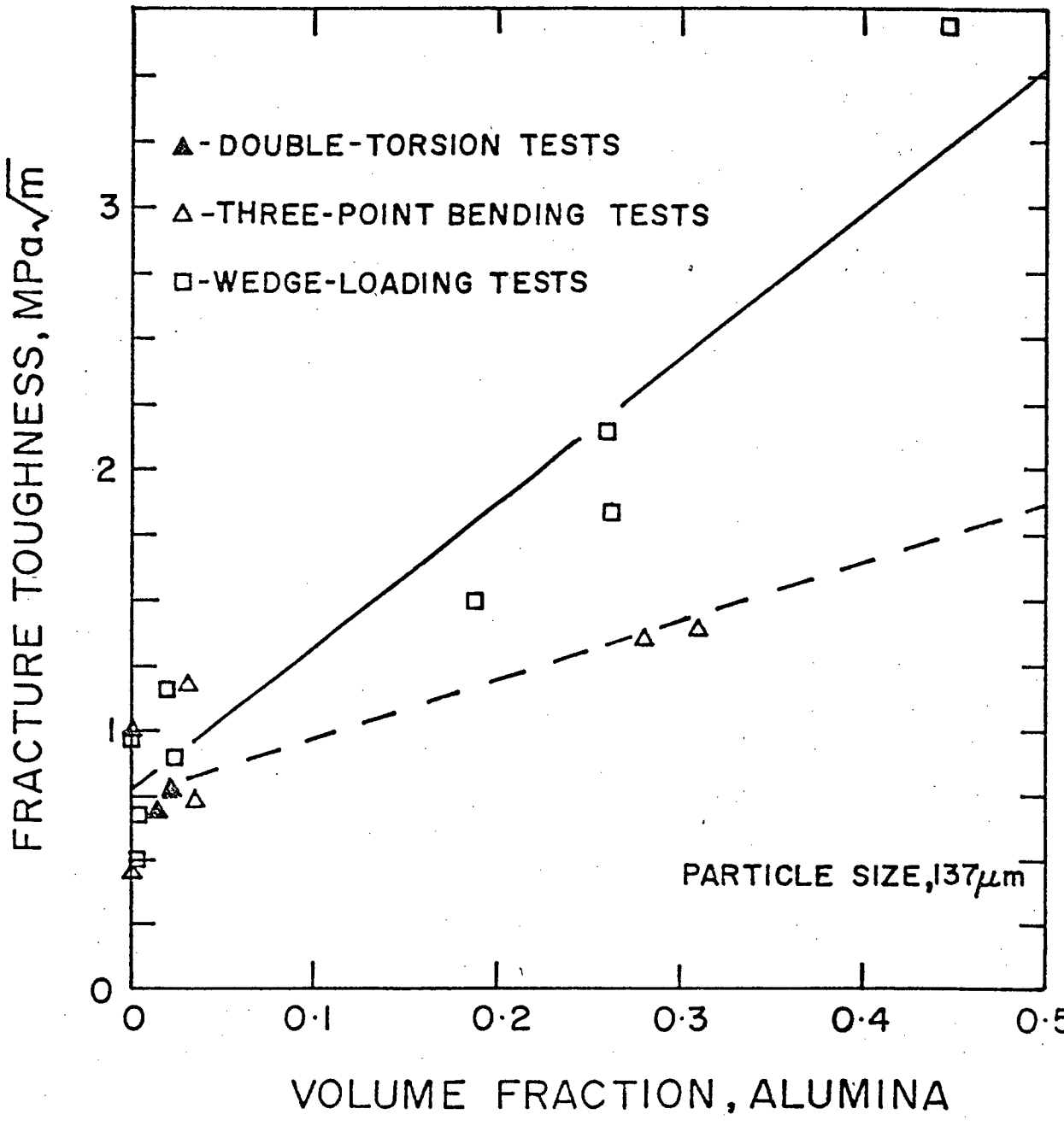

Figure 17. Fracture toughness versus volume fraction. Double torsion, wedge-loading and three-point bending tests.

TABLE VII

Summary of Compliance Calibration Results for Double Torsion Specimens

	V_f = 0.003 Average Particle Size: 137 μm	V_f = 0.122 Average Particle Size: 65 μm	V_f = 0.340 Average Particle Size: 65 μm
Linear Regression Analysis Equations: $C = \frac{y}{P} = Ba + D$	$6.53 \times 10^{-6}a + 3.8 \times 10^{-7}$	$5.06 \times 10^{-6}a + 3.3 \times 10^{-7}$	$2.77 \times 10^{-6}a + 1.19 \times 10^{-7}$
No. of data Points	6	6	6
Correlation Coefficient r	0.99	0.99	0.98

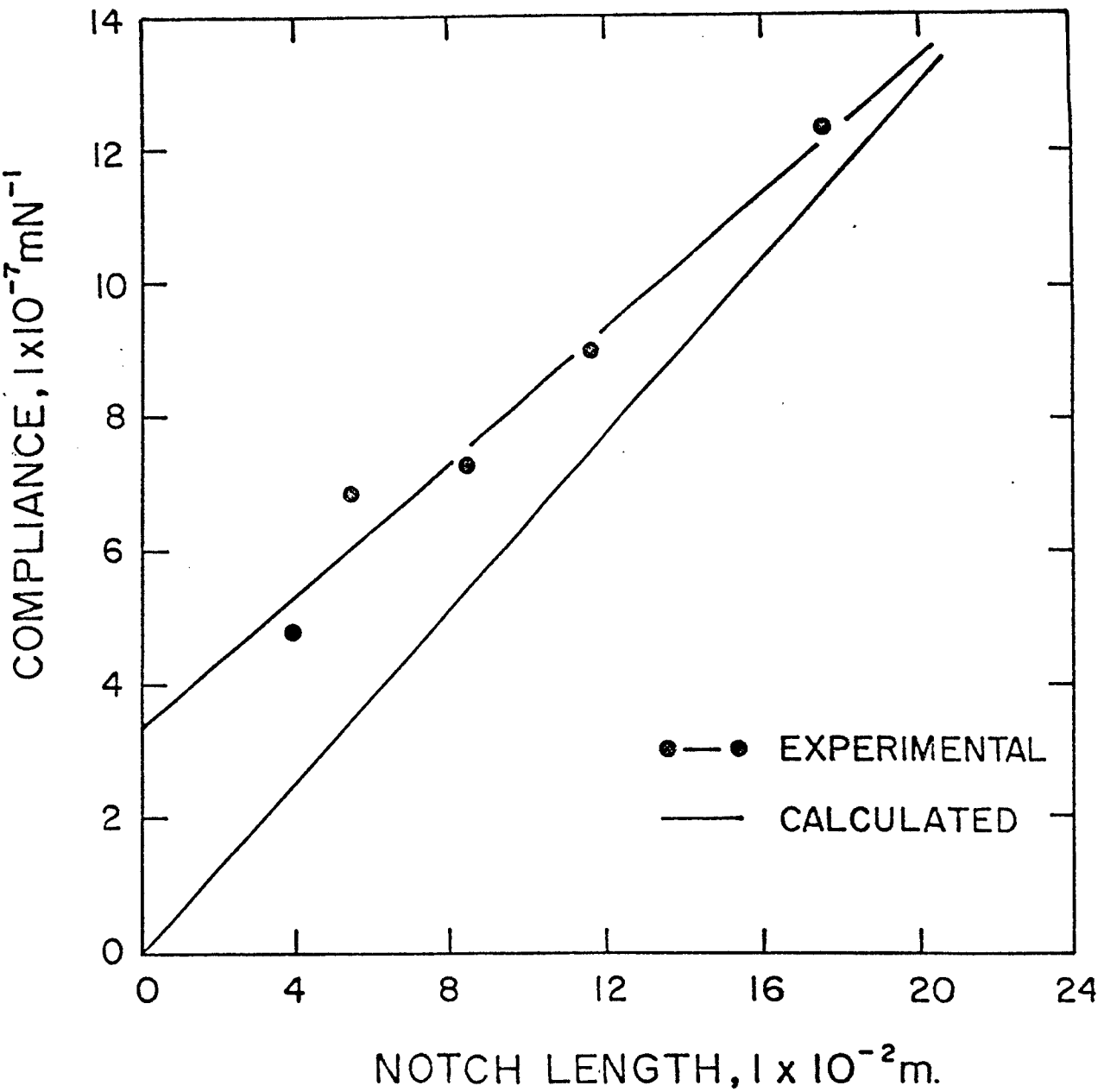

Figure 18. Compliance versus machined notch length of a double torsion specimen. Average particle size: 65 μm. V_f = 0.12.

compliance was obtained using the following equation[20]:

$$C = \frac{w_m 2a(1 + \nu)}{WB^3 E} \qquad (34)$$

where ν = the Poisson's ratio, was approximated to 0.3,

E = the elastic modulus determined in wedge-loading tests. (The composition of the sample was approximately the same as that of the sample in compliance calibration).

This relation assumes that there is no displacement at the loading points for a (crack length) equal to zero. The discrepancy between calculated and empirical compliance is probably due to this assumption.

3.1.2.4.2. Wedge-Loading Specimens

To express the compliance as a function of crack length, empirical curve fitting was done by a computer+. A cubic function was selected for curve fitting for two reasons. First, the analytic equation for compliance in a non-grooved sample is:

$$C = \frac{8a^3}{BH^3 E} \qquad (30)$$

+ The program P:2R of the Biomedical Computer Programs P-series was used.

and second, after a trial run, the empirical values had a correlation coefficient of .99 with the experimental compliance values. The empirical equation for compliance became:

$$C = \alpha_0 + \alpha_1 x_1 + \alpha_2 x_2 + \alpha_3 x_3 \qquad (35)$$

where α_n = fitting parameters and $x_n = a^n$.

In most of the equations α_0 and α_1 were equal to zero.

In Figure 19, the empirical, the analytical and the experimental compliance are graphed, each as a function of crack length. The agreement of the three compliance curves is significant.

Since the analytic compliance is calculated for a non-grooved sample, Hoagland[28] suggests the use of a correction factor for calculating the fracture energy of grooved samples. This factor accounts for the changed moment of inertia because of the presence of the groove. The correction factor is $\left(\frac{I_p}{I_{sg}}\right)^{1/3}$.

where I_{sg} is the moment of inertia of a grooved sample.

I_p is the moment of inertia of a non-grooved sample

s is one half of the groove depth.

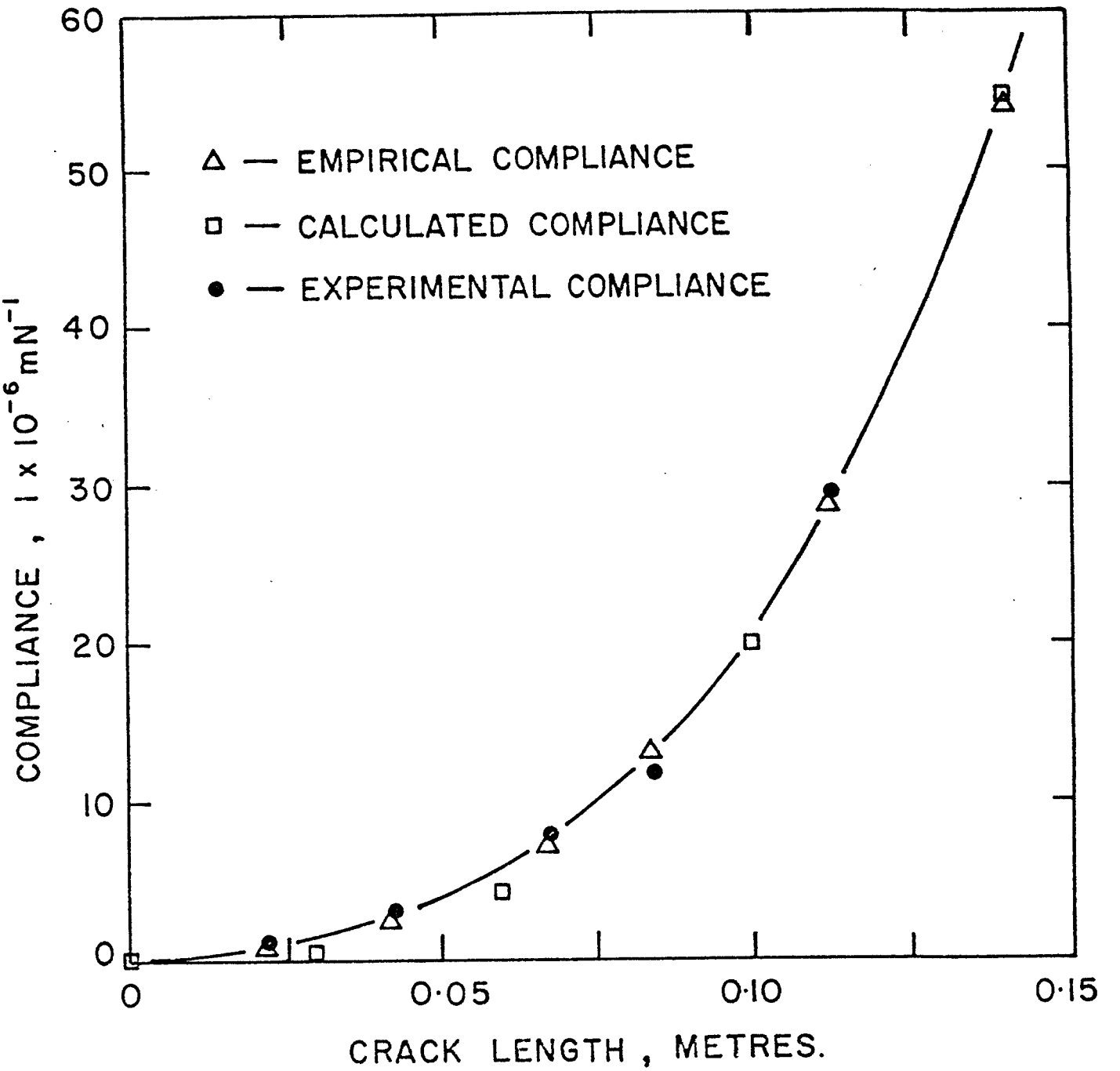

Figure 19. Compliance versus crack length for a wedge-loaded specimen. Average particle size: 90 μm. V_f = 0.23.

$$\frac{I_{sg}}{I_p} = \left[\frac{s}{H}\tan\theta\right]^3\left[4 - \frac{6s}{B}\right] + 4\left[1 - \frac{s}{H}\tan\theta\right]^3 - 12\left[\frac{\left(\frac{1}{2} - \frac{s}{H}\tan\theta + \frac{2}{3}\frac{s^2\tan^2\theta}{BH^2}\right)^2}{1 - \frac{s^2}{BH}\tan\theta}\right] \quad (36)$$

where, θ is the wedge half angle.

Thus, the corrected fracture energy, G_{co}, is:

$$G_{co} = G(I_p/I_{sg})^{1/3} \quad (37)$$

The correction factor for wedge-loading samples was found to be $\leq$ 2%. The experimental compliance of a non-grooved sample, having a notch length of 2.5 cm, remained the same after a groove 2/3 of the sample thickness was introduced. The low correction factor and no apparent effect of the existence of the groove on the compliance explains the agreement between the calculated and experimental values.

3.1.3. Acoustic Emission Tests

AE per area is reported here, since the number of AE counts depends on the size of the area broken in the specimen. In double torsion specimens the crack was hardly visible. Therefore, the data presented here are only from wedge-loading and three-point bending tests.

3.1.3.1. Acoustic Emission from Wedge-Loading Tests

The AE counts accompanying the wedge-loading tests (Figure 14) are plotted versus time in Figure 20. By comparing the two figures it is found that each inflection on the loading curve can be associated with an AE burst. The magnitude of AE increases with the size and volume fraction of particles (Figure 20).

Table VIII summarizes the AE results from wedge-loading tests. The average AE per unit area was calculated by averaging the AE per unit area of all the crack jumps, which occurred during the fracture of the sample. Figure 21 illustrates the effect of volume fraction of alumina on total AE per unit area for composites of differing average particle size. Figure 22 shows average AE per unit area as a function of volume fraction for composites of differing particle size. Total AE per unit area and average AE per unit area increased initially as the alumina volume fraction increased. Then, at a higher volume fraction, total AE per unit area and average AE per unit area dropped, except for the composites of 137 μm particle size where it appeared to reach a plateau. For any volume fraction total AE per unit area and average AE per unit area increased for larger particle sizes.

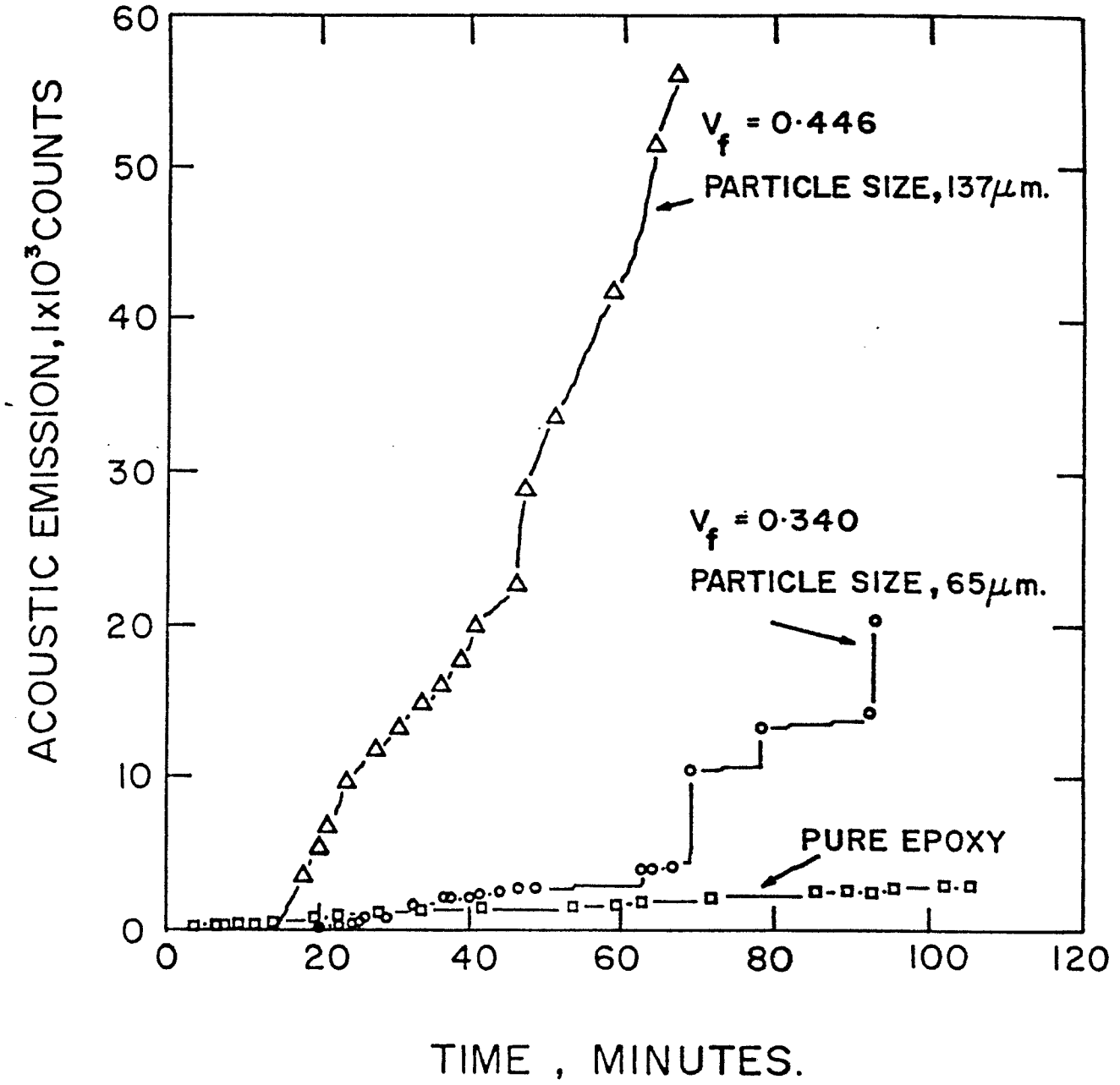

Figure 20. AE versus time curve during wedge-loading tests of specimens of different compositions.

TABLE VIII

Summary of AE Results from Wedge Loading Tests

Average Alumina Particle Size (μm)	Volume Fraction of Alumina	Total Acoustic Emission per Unit Fractured Area (10^7 x counts/m^2)	Average Acoustic Emission per Unit Fractured Area (10^7 x counts/m^2)
-	0.000	0.4496	0.4237
40	0.006	0.2710	0.5930
"	0.091	0.9043	1.8730
"	0.129	1.7069	2.0775
50	0.013	0.8529	0.8671
"	0.025	0.2061	0.5600
"	0.037	1.4261	2.2160
"	0.087	3.5355	3.4724
"	0.132	0.5936	0.7129
"	0.140	1.3424	2.1261
65	0.038	7.0536	7.4424
"	0.083	4.6024	6.2435
"	0.121	7.9932	8.6685
"	0.194	4.2072	4.6237
"	0.287	2.0314	2.1154
"	0.337	3.0960	1.8655
90	0.007	0.3820	0.5697
"	0.042	0.1575	0.1765
"	0.134	3.5319	3.2585
"	0.189	7.8488	7.8110
"	0.195	8.3210	9.0380
"	0.230	12.4906	11.6548
"	0.314	4.0795	2.8995
"	0.378	4.3055	2.3474
115	0.010	3.2374	3.3200
"	0.025	2.1288	2.7618
"	0.076	8.6490	7.9142
"	0.093	9.1538	9.6891
128	0.078	5.5108	5.7799
"	0.106	7.7890	8.9662
137	0.003	0.6103	0.8192
"	0.021	0.8937	1.0541
"	0.025	5.7702	5.4341
"	0.186	16.4538	17.8205
"	0.258	21.7427	22.0946
"	0.260	14.7361	16.2253
"	0.444	14.5145	14.0995

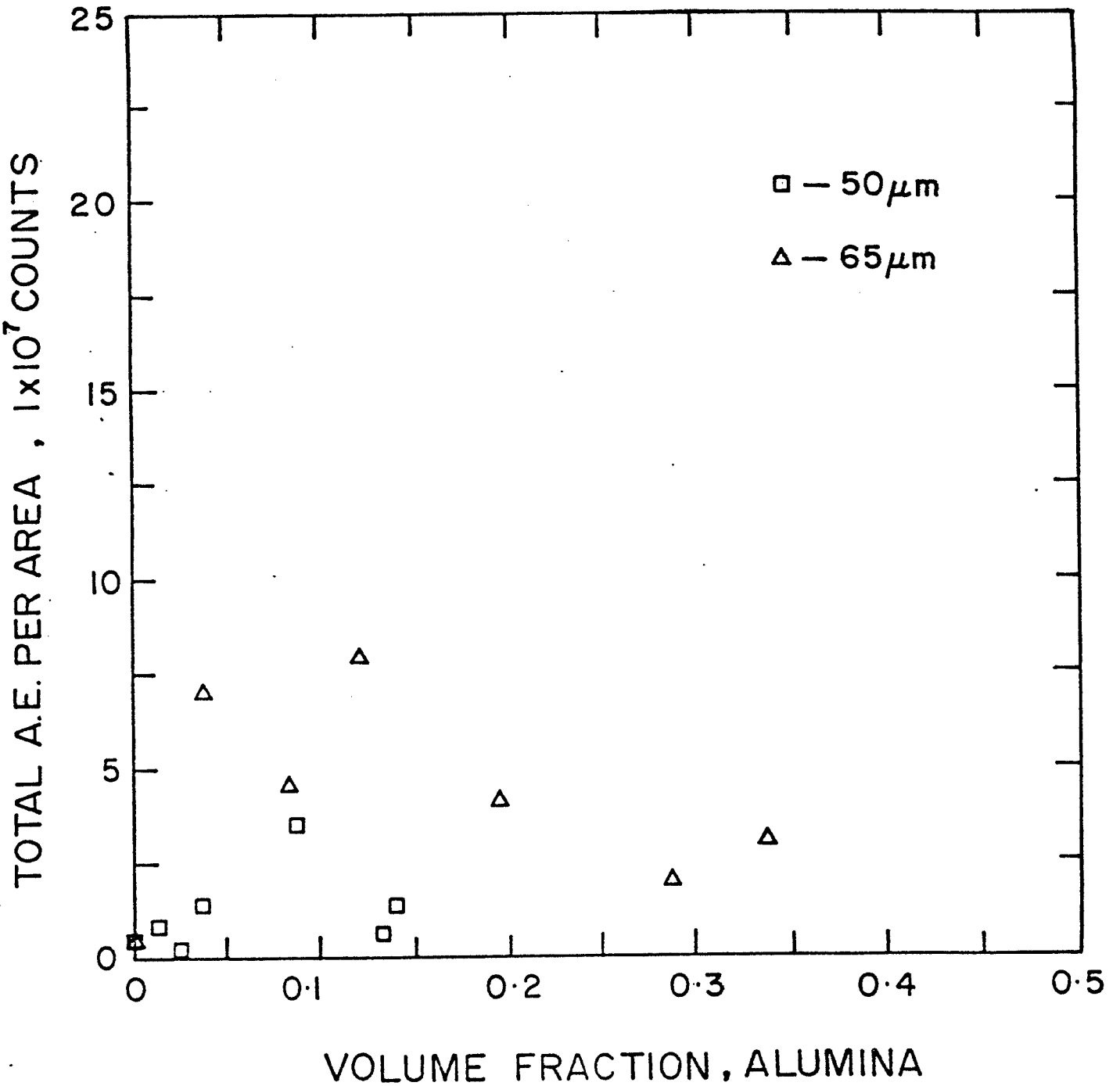

Figure 21a. Effect of volume fraction of alumina on total AE per unit area for composites of differing particle size.

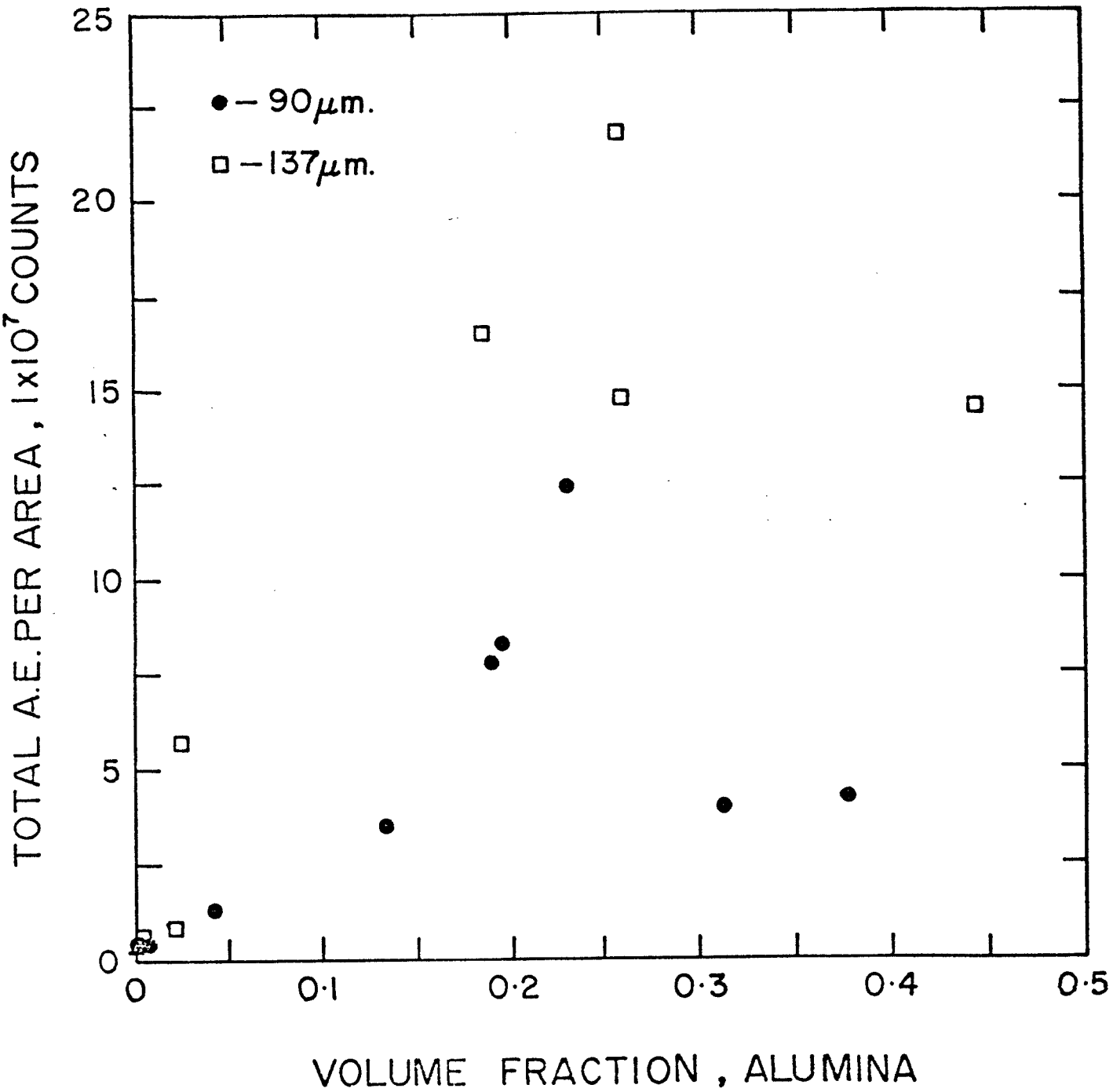

Figure 21b. Effect of volume fraction of alumina on total AE per unit area for composites of differing particle size.

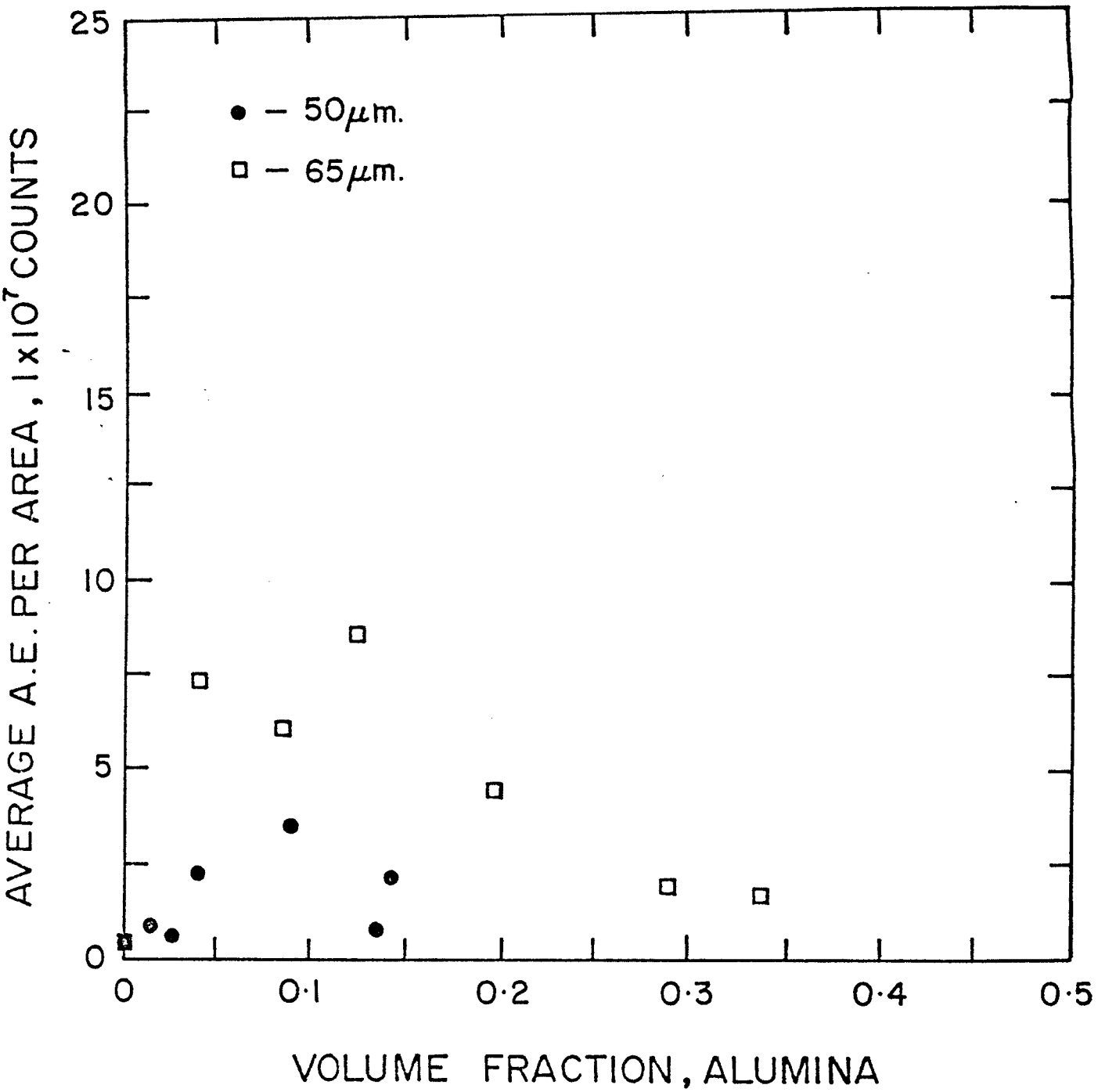

Figure 22a. Effect of volume fraction of alumina on average AE per unit area for composites of differing particle size.

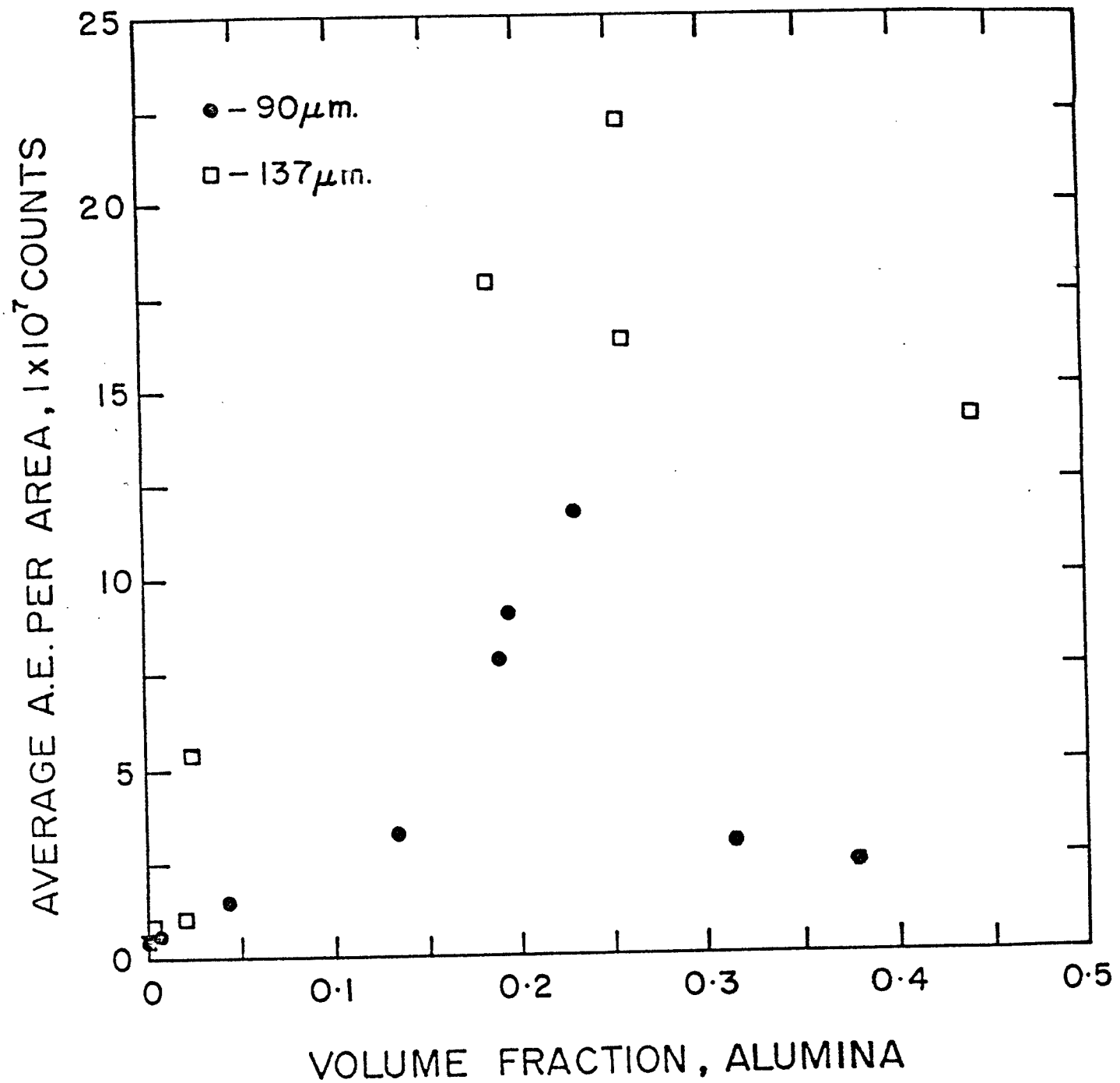

Figure 22b. Effect of volume fraction of alumina on average AE per unit area for composites of differing particle size.

In most wedge-loading tests, the crack followed the groove. However, in a number of specimens the crack deviated from the groove at a short distance from the notch. The test was stopped when this happened, and only the AE of the part of the test in which the crack followed the groove was recorded. Since attenuation is somewhat dependent on the AE source to transducer distance, an attempt was made to correct the AE count for the position of the crack. The following approximation was used:

$$AE_{MOD} = AE\left(1 - \frac{y_{INT}}{SLO}\,(L_T - a)\right) \qquad (38)$$

where, AE_{MOD} is the AE at zero distance from the transducer,

a is the crack length,

y_{INT} and SLO are the y intercept and the slope, respectively, of the AE attenuation lines (Section 3.1.1.3) and

L_T is the length of the specimen.

The shape of the curves of AE_{MOD} did not differ significantly from the graphs in Figures 21 and 22. Therefore, the data for AE_{MOD} were not included.

3.1.3.2. Acoustic Emission from Three-Point Bending Tests

In most of the specimens used in three-point bending tests the crack propagated in one jump. Therefore, only

total AE per unit area was calculated. Table IX contains the AE per unit area for the different specimens used in these tests. The AE data have a large scatter.

In wedge-loading tests an average AE per unit area was calculated by averaging the AE per unit area of all the crack jumps that occurred during the fracture of the sample. In wedge-loading tests standard variations of up to the same magnitude as the average AE per unit area were calculated. When only one AE burst was analyzed, as in three-point bending tests, the AE per unit area calculated represents a much smaller sample.

3.1.4. Fractography of Alumina-Filled Epoxy Composites

Sections of the fracture surface of pure epoxy were covered with fibrils, particularly in the sites where the crack had been arrested. The fibrils ran perpendicular to the crack arrest marks (parallel to direction of crack advance), Figure 23. Figure 24 shows a section where the fibril was initiated. The regions which appeared macroscopically smooth, at higher magnification seemed to have an uneven texture. Small cavities, 1 μm wide, could be seen in the fibrils, (Figure 25).

TABLE IX

Summary of AE Results from Three-Point Bending Tests

Average Alumina Particle Size (μm)	Volume Fraction of Alumina	Total Acoustic Emission (counts)	Total Acoustic Emmission per Unit Fractured Area (10^7 x counts/m^2)
-	0.000	880.	1.0672
-	0.000	330.	0.2672
90	0.042	425.	0.4522
"	0.045	317.	0.3563
"	0.077	949.	1.1152
"	0.093	500.	0.5512
"	0.124	230.	0.2849
"	0.130	220.	0.2398
"	0.201	709.	0.8083
"	0.289	1173.	1.2468
"	0.289	900.	0.9119
"	0.333	1200.	1.4215
137	0.001	581.	0.6569
"	0.001	564.	0.6153
"	0.031	310.	0.3389
"	0.034	550.	0.6099
"	0.282	5500.	6.6951
"	0.310	+	-
"	0.500	39900.	46.5686

+ Out of scale

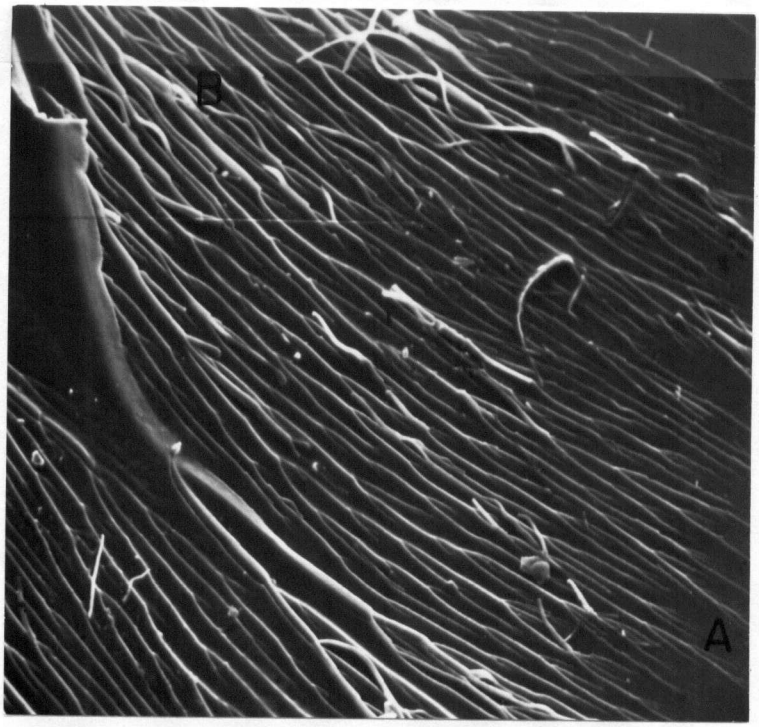

Figure 23. Scanning electron micrograph (SEM) of unfilled epoxy.

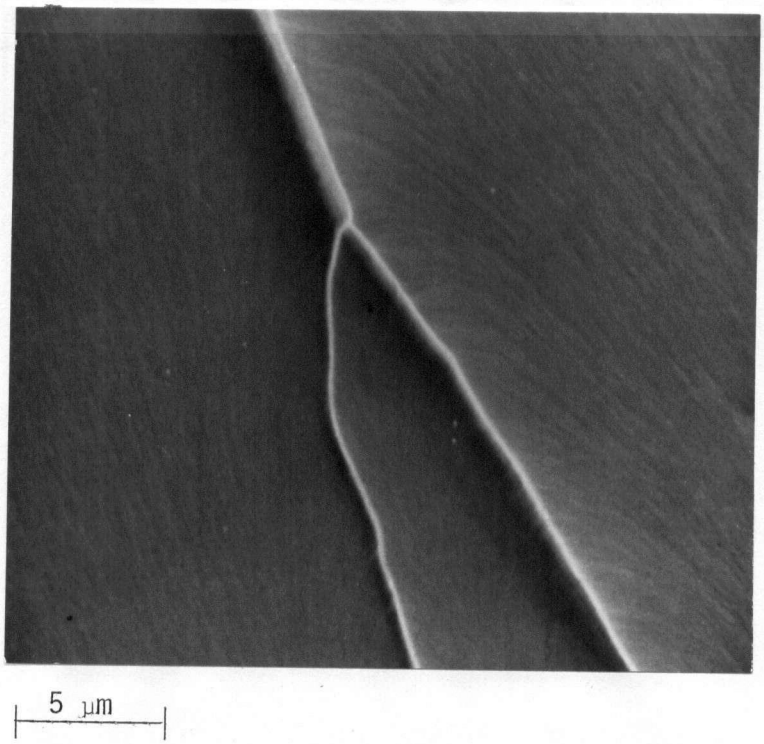

Figure 24. Enlargement of Section A in Figure 23. Unfilled epoxy.

Figure 25. Enlargement of Section B in Figure 23. Unfilled epoxy.

Figures 26a through 26d show the effect of particle size and volume fraction on the fracture surface. In Figures 26a, b and c, marks indicating crack-particle interaction are present. For a large volume fraction, 0.44, such marks can not be seen (Figure 26d). Composites of large particle size exhibit secondary cracking even at low volume fractions (Figure 26b).

The surface of the alumina particles was imprinted in the epoxy matrix (Figures 27 and 28). Figure 28 shows cavities resulting from the separation of alumina particles from the epoxy matrix. Pieces of epoxy were present on the surface of some alumina particles, Figure 29. Using X-ray energy spectral analysis, it was found that pieces of alumina particles fractured during wedge-loading tests (Figure 30).

3.2. Tests on Steel Composites

3.2.1. Fracture Tests

Table X contains values of fracture toughness for the different specimens used in three-point bending tests. For an alumina volume fraction of 0.01, the fracture toughness appeared to decrease with increasing particle size. However, for an alumina volume fraction of 0.05, the toughness values did not follow this trend. Therefore, the lack of a distinct

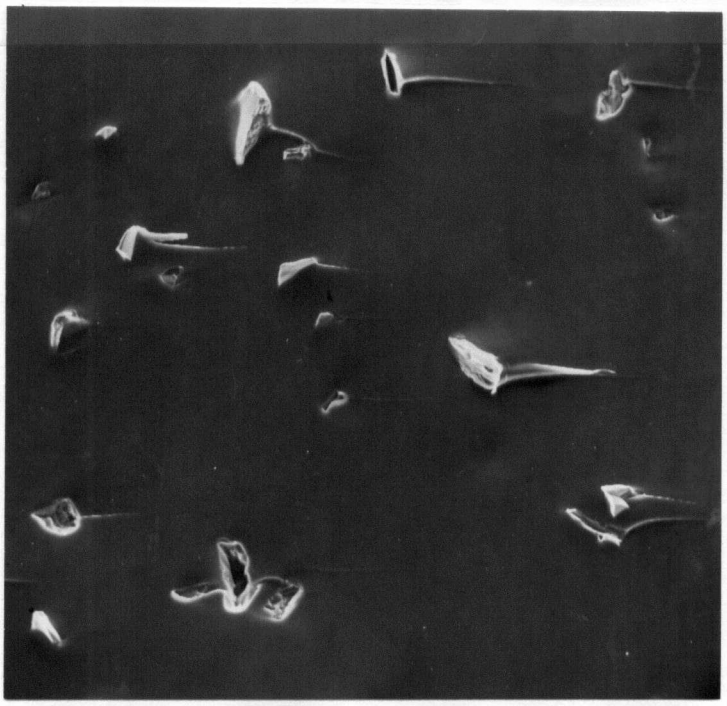

Figure 26. SEM of alumina-filled epoxy.
a. Average particle size: 50 μm.
V_f = 0.013

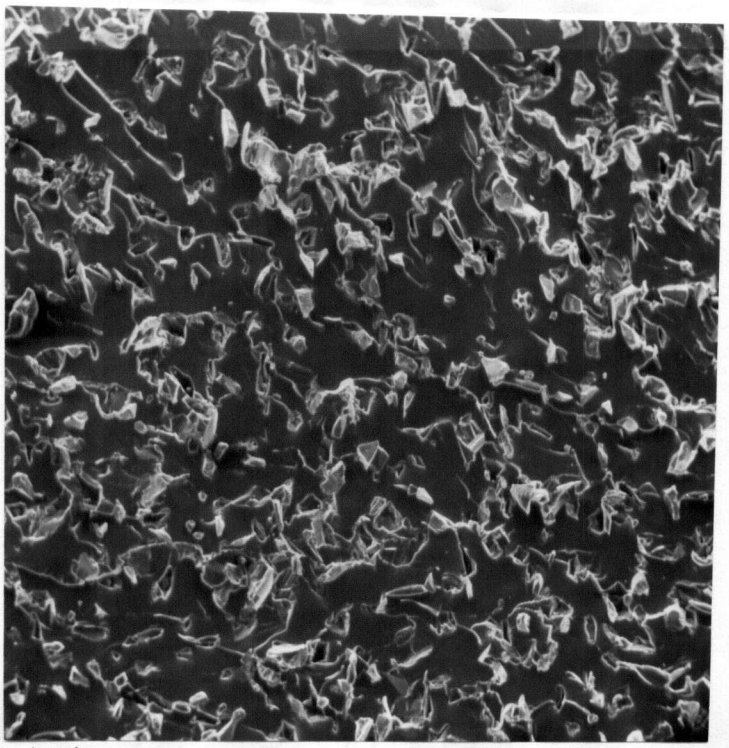

Figure 26. SEM of alumina-filled epoxy.
b. Average particle size: 65 μm.
V_f = 0.194

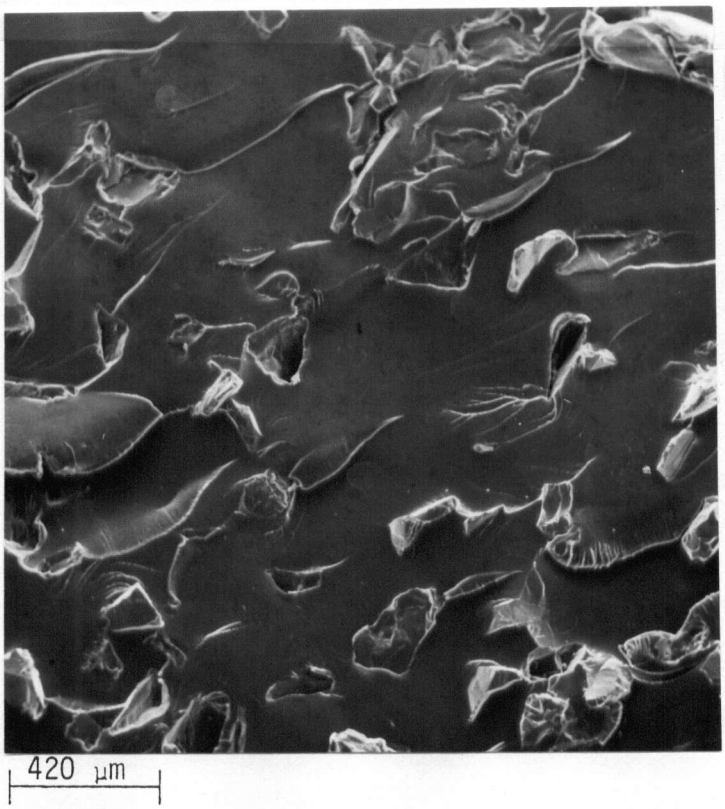

Figure 26. SEM of alumina-filled epoxy.
c. Average particle size: 137 μm.
V_f = 0.186

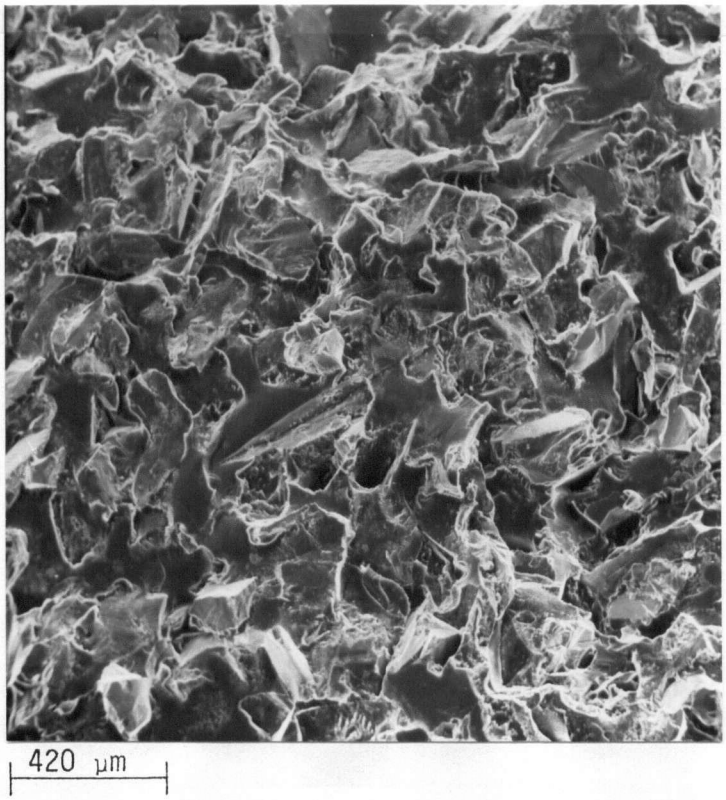

Figure 26. SEM of alumina-filled epoxy.
d. Average particle size: 137 μm.
V_f = 0.444

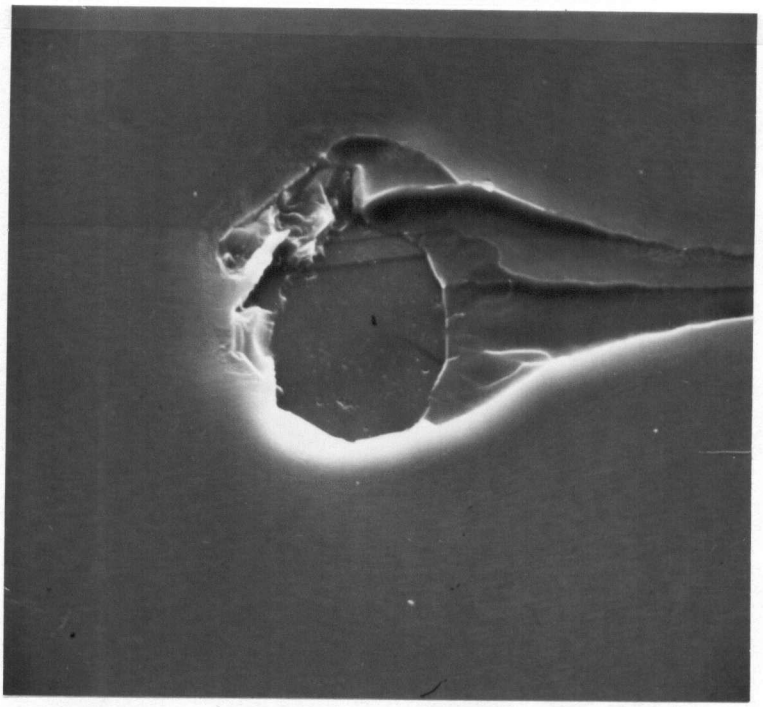

Figure 27. SEM of alumina-filled epoxy exhibiting particle pull-out. Average particle size: 50 μm. V_f = 0.013

Figure 28. SEM of alumina-filled epoxy exhibiting particle pull-out and embedded particles. Average particle size: 137 μm. V_f = 0.186.

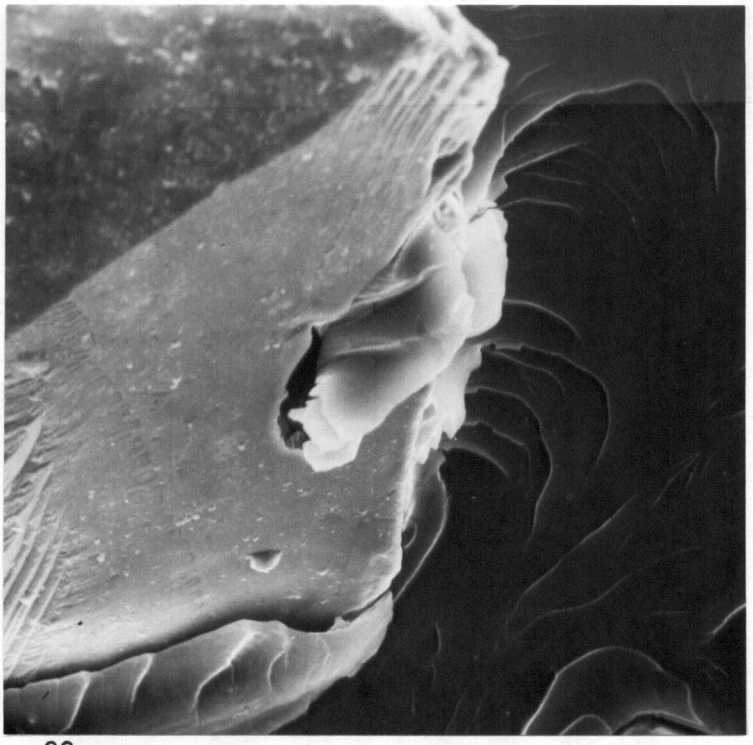

Figure 29. SEM of alumina-filled epoxy. Epoxy can be seen on the surface of the alumina particle. Average particle size: 137 μm. V_f = 0.186.

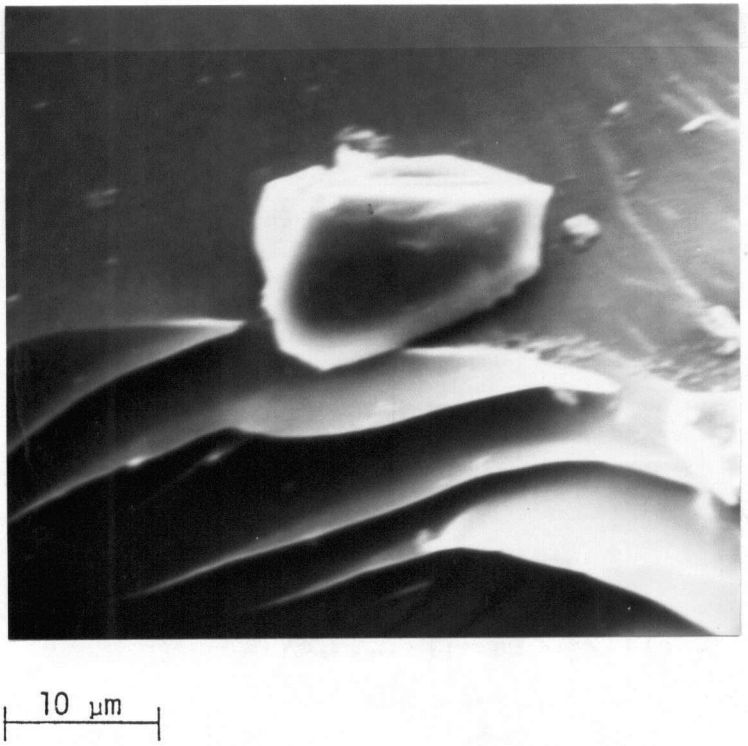

Figure 30. SEM showing a small alumina particle. Average particle size of the composite: 137 μm. V_f = 0.186.

TABLE X

Fracture Toughness of Alumina-Filled Martensitic Steels.

Three-Point Bending Tests

Average Alumina Particle Size (μm)	Volume Fraction of Alumina	Fracture Toughness (MPa√m)
-	0.000	36.16
-	0.000	49.29
50	0.01	21.52
"	0.01	38.53
"	0.01	38.37
"	0.01	44.58
65	0.01	43.37
"	0.01	25.90
"	0.01	32.88
"	0.01	34.65
"	0.01	29.64
90	0.01	23.88
"	0.01	23.95
"	0.01	24.57
"	0.01	20.08
"	0.01	25.15
"	0.01	25.79
"	0.01	25.13
"	0.01	28.93
137	0.05	34.07
"	0.05	26.16
"	0.05	31.05
"	0.05	24.71
"	0.05	27.05

pattern for all the results does not allow for conclusions. The bluntness of the crack in the samples, the varying composition and the changing microstructure of the fabricated specimens could all have contributed to the large scatter in the results.

3.2.2. Acoustic Emission Tests

Table XI contains the AE per unit area during cracking for the different specimens used in three-point bending tests. The inconsistency of the results does not permit a correlation to be made between AE and the composite microstructure. The AE test was unreliable because only one AE burst was measured (Section 3.1.3.2.) and the composition could not be controlled. Both factors could have contributed to the scatter.

3.2.3. Fractography of Alumina-Filled Martensitic Steel Composites

The original iron powders are shown in Figure 31 and the surface of a fractured composite is represented in Figure 32. From the electron scanning micrographs, the grain size of the steel matrix was estimated to be 4-13 μm. Therefore, it is evident that the cracks propagated through

TABLE XI

Acoustic Emission of Alumina-Filled Martensitic Steels.

Three-Point Bending Tests

Average Alumina Particle Size (μm)	Volume Fraction of Alumina	Acoustic Emission per Fractured Area (10^9 counts/m^2)
-	0.000	1.179
-	0.000	3.004
50	0.010	14.246
"	0.010	3.292
"	0.010	10.675
"	0.010	4.163
65	0.010	3.729
"	0.010	7.331
"	0.010	4.002
"	0.010	6.090
"	0.010	2.194
90	0.010	1.654
"	0.010	7.722
"	0.010	8.409
"	0.010	11.593
"	0.010	4.443
"	0.010	2.707
"	0.010	3.939
"	0.010	3.200
137	0.050	5.706
"	0.050	9.187
"	0.050	6.905
"	0.050	9.039
"	0.050	10.580

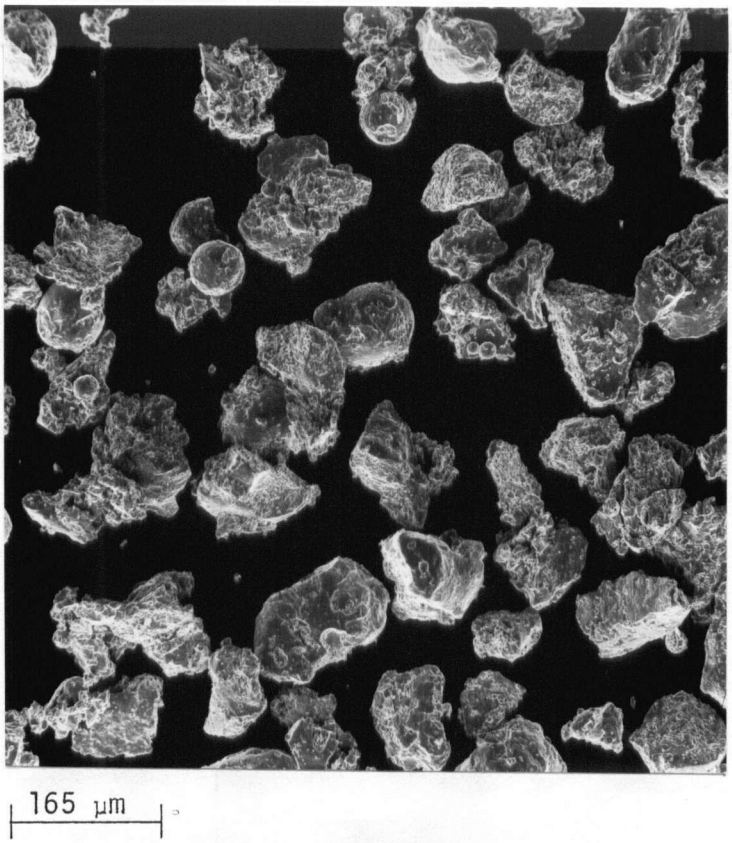

Figure 31. SEM of iron powders Atomet 28.

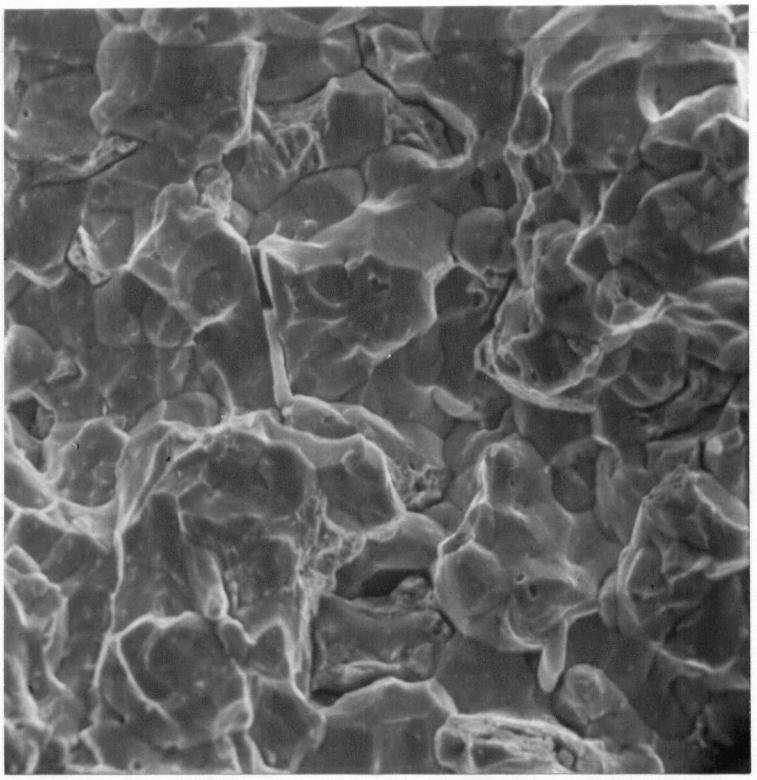

Figure 32. SEM of martensitic steel composite exhibiting intergranular failure. Average particle size: 50 µm. $V_f = 0.01$

the original steel powders. The composite which was fractured at liquid nitrogen temperature exhibited both transgranular and intergranular failure (Figure 33). This low temperature test further confirmed that the iron powders had consolidated during hot forging and hot rolling and that therefore the cracks travelled through the steel powders rather than around them.

Particle decohesion from the matrix seemed to occur in some of the contact zones between the matrix and the particle (Figure 34). Nevertheless, bonding appeared not to have taken place over the entire particle surface area (Figure 34).

Extensive areas of the fracture surface exhibited dimples (Figure 35). After observing dimple zones, three-point bending tests were abandoned since the dimples could have masked the effect of the alumina particles on AE.

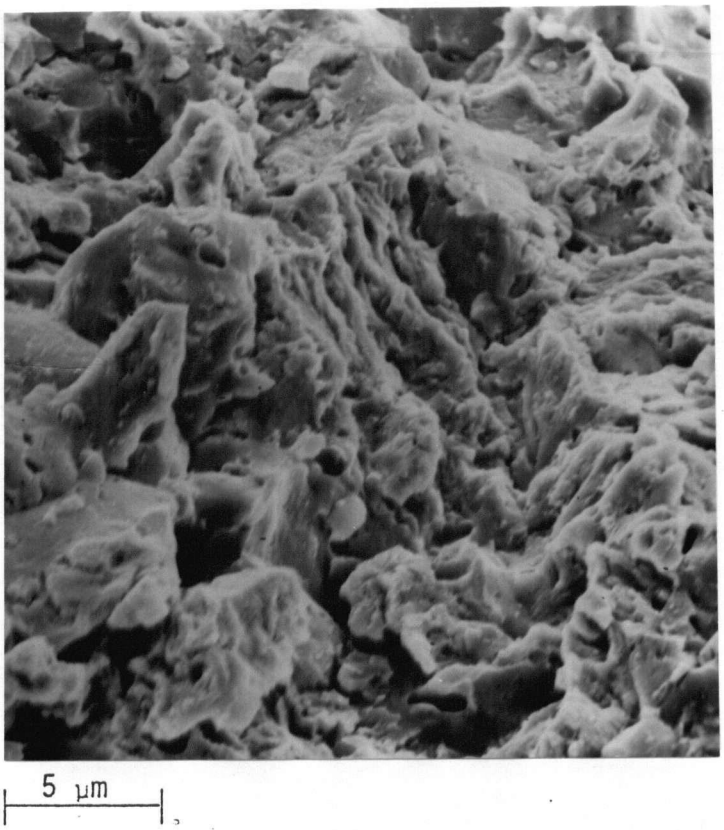

Figure 33. SEM of martensitic steel composite fractured at liquid nitrogen temperature. V_f = 0.000

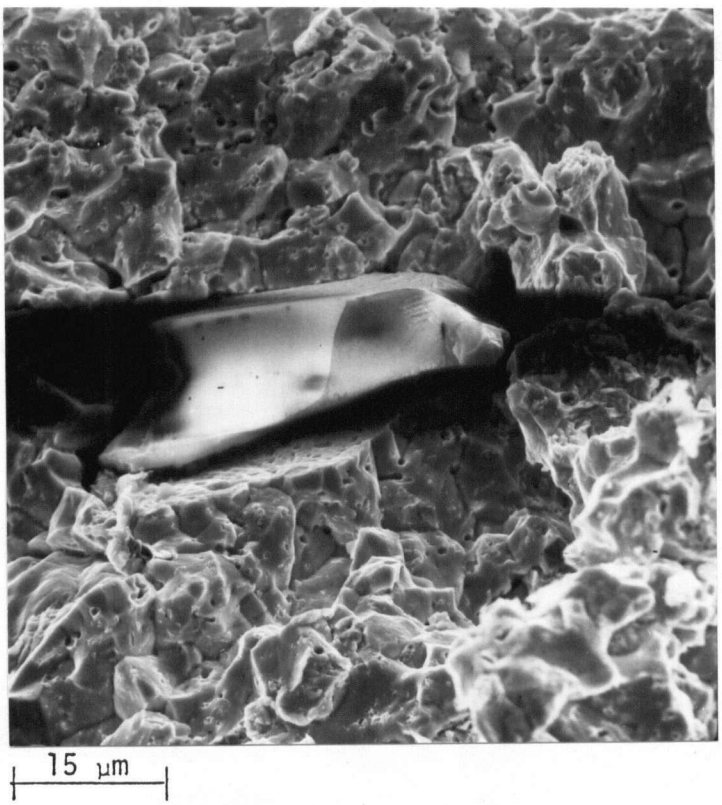

Figure 34. SEM of martensitic steel composite exhibiting a region of particle decohesion. Average particle size: 40 μm. V_f = 0.01

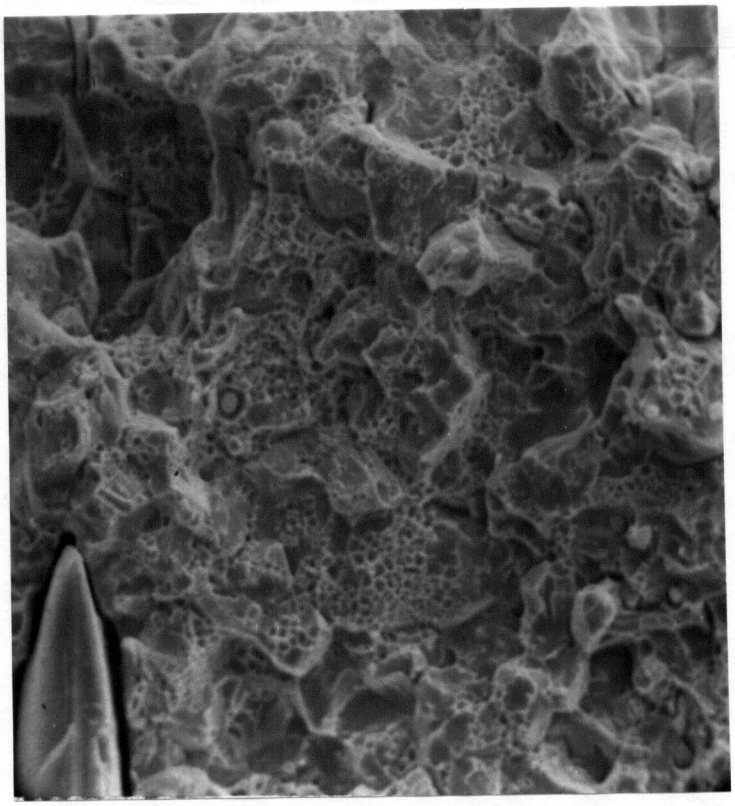

15 μm

Figure 35. SEM of martensitic steel composite exhibiting dimples. Average particle size: 40 μm. V_f = 0.01

4. ANALYSIS OF RESULTS AND DISCUSSION FOR ALUMINA REINFORCED EPOXY COMPOSITES

In this chapter only the properties of alumina reinforced epoxy composites are discussed. The results from particle-filled martensitic steels are not dealt with for reasons explained in Section 3.2. The properties of the epoxy composites are discussed in the following order:

1. elastic constants.
2. acoustic wave attenuation.
3. fracture energy and toughness.
4. acoustic emission during fracture.

4.1. Elastic Constants

The scatter observed in the values of the elastic constants (Figure 9) could be attributed to the characteristics of the fabricated samples. The samples were prepared from different batches of resin and curing agent varying slightly in their composition. The age of these materials varied and some changes in the batch, such as polymerization, could have occurred. During frequent sampling, exposure to air could have changed the moisture content of the bulk and contamination could have occurred. The temperature fluctuations in the furnace,

during 17 1/2 hours of curing, could have varied from one batch of samples to the next. The holes in the finished sample did not affect the toughness, but did affect the compliance and therefore the apparent elastic modulus.

Figure 9 illustrates the theoretical predictions of Kerner[29], Paul[30], and Ishai[31]. The experimental values of the elastic modulus are in the vicinity of these predicted curves. Paul's and Ishai's equations define narrow boundaries for the elastic moduli of composites, in which the ratio of filler elastic modulus, E_f, to matrix elastic modulus, E_E, is greater than 20[32]. This is the case for alumina-filled epoxy. Kerner used an averaging procedure to determine elongations and stresses within the composite in order to derive formulas for the elastic modulus. Paul and Ishai used the energy theorems of elasticity to obtain their equations.

$$E_c = \left(\frac{1 + A_t c V_f}{1 - c V_f}\right) E_E \tag{39}$$

$$A_t = \frac{7-5\nu_E}{8-10\nu_E} \tag{40}$$

$$c = \frac{E_A/E_E - 1}{E_A/E_E + A_t} \tag{41}$$

where E_c = the elastic modulus of the composite,

E_A = 393. GPa[26] is the elastic modulus of alumina,

V_f is the volume fraction of alumina, and

ν_E = 0.352 is the Poisson's ratio of epoxy[19].

Paul's equation for the upper-bound values of the elastic modulus is[30]:

$$E_c = E_E\left[\frac{E_E + (E_A - E_E)V_f^{2/3}}{E_E + (E_A - E_E)V_f^{2/3}(1 - V_f^{1/3})}\right] \qquad (42)$$

Ishai's equation defines the lower-bound values of the elastic modulus[31]:

$$E_c = E_E\left[1 + \frac{V_F}{(E_A/E_E)/(E_A/E_E - 1) - \sqrt[3]{V_f}}\right] \qquad (43)$$

Even though Kerner's equation refers only to low-filler concentrations, the results from this experiment for high concentrations appeared to be in agreement with Kerner's curve.

E_E, the elastic modulus of epoxy, was determined to be 4.34 GPa and this value was used in the calculations of predicted values. Most of the experimental elastic moduli of the composites for large volume fractions are in the region bounded by Paul's and Ishai's curves. However, there is one set of points outside the boundaries of these regions. It is possible that, if the values of E_E between 3 GPa - 4 GPa

were used for Kerner's and Ishai's equations, these points would be within the boundaries. Values of 3 GPa have been published[19].

Summary

The elastic modulus was found to increase with increasing alumina volume fraction. The elastic constants were independent of the alumina particle size. The theoretical predictions of Kerner, Paul and Ishai on the elastic modulus of particle reinforced composites were in reasonable agreement with the experimental values found in this study.

4.2. Attenuation of Elastic Waves

The attenuation of a material is generally expressed in dB/m. With the type of equipment used in this study, it was not possible to measure attenuation in dB/m. However, the pulser tests (Section 2.3.1.3.) expressed attenuation in counts/m, which was a relative measure of changes in the magnitude of attenuation.

A pulser introduces AE through the surface of a material. During fracture, AE is generated both in the interior and on the surface of the material. AE is measured in all cases by

a transducer placed on the surface. It seemed reasonable to assume that the relations of AE and the distance between the transducer and the source in fractured epoxy would follow a similar pattern to that in pulsing tests.

Attenuation was influenced by the shape of the sample (Figure 10). Imperfections, such as cavities in the specimens, produced unpredictable results. Just as in testing for the elastic modulus (Section 4.1.), the properties of the resin, curing agent and the factors affecting the sample fabrications could have contributed to the scatter in the results.

For metals, the attenuation of elastic shear waves and longitudinal waves has been related to the inverse of the velocity of the wave[33]. Since the velocity of the wave increases with the elastic modulus of any solid material[34], attenuation decreases with the increase of the elastic modulus. Therefore, the difference of attenuation between epoxy and glass (Figure 10) is a result of the difference in their elastic moduli, $E_G/E_E \simeq 23$.

Munson et al[34] found that the wave velocity of alumina-filled epoxy increased with increasing alumina volume fraction. Assuming that the wave propagation phenomenon in alumina-filled epoxy is similar to that in metals, the decrease in attenuation

with the increase of alumina volume fraction (Figure 11) can be mainly attributed to the increasing modulus. It was observed that particle size had no influence on attenuation. This is in agreement with the fact that the elastic modulus is also independent of particle size (Section 3.1.1.2.). It also suggested that the scatter of waves due to the presence of discontinuities (interfaces) in the material was not an important factor in attenuation since the amount of interface increases as the particle size decreases. Other workers[35], studying the propagation of shock waves through fibre-reinforced composites, have found that the dispersive effect of phase discontinuities on attenuation was negligible. In the attenuation tests, where a pulser and a transducer were separated by the sample thickness (front-to-front tests), the counts in glass were $\sim$ 5 times higher than those in epoxy. The same relation was found between the y intercepts of the linear functions of counts versus distance calculated for glass and epoxy (Figure 10). In testing alumina-filled epoxy composites of varying volume fraction, no dependence of front-to-front and y intercepts on volume fraction was observed (Figure 12 and 13). No satisfactory explanation was found for the latter.

Summary

The attenuation of acoustic waves due to distance between source and detector in the epoxy composites was found to be

dependent on the volume fraction of alumina. It appeared to be independent of the alumina particle size. The acoustic wave attenuation decreased slightly with increasing elastic modulus, but the effect was too small to be of significance in the fracture studies.

4.3. Fracture Energy and Toughness

An attempt is made here to analyze and compare the fracture energy and toughness results from this study with the already existing theories. Some of the factors that have been suggested to increase the fracture energy are discussed.

Surface Roughness

Fracture energy values are calculated for a smooth surface. Lange[25] estimated the fracture surface of a particle reinforced composite of 0.5 volume fraction to be ≈ 2 times the fracture surface of an unfilled material. He suggested that the increase in area due to surface roughness is independent of the filler particle size. In this study partial particle separation from the matrix (Figure 28) and secondary cracking (Figure 26c) were observed. The two latter factors together with the increase in surface roughness (because of the presence of particles) determine the surface area increase for the composites tested here. The following model was used to calculate the total surface area.

Assumption:

The interfaces of all particles intersected by the crack are completely fractured.

Mathematical Development:

According to Fullman[36],

$$N_s = N_v p \tag{44}$$

where N_s = average number of intersections per unit area of sectioning plane.

N_v = number of particles/unit vol.

p = probability of plane intersecting a particle,

and

$$p = D \tag{45}$$

where D is the average particle size.

The volume fraction of filler can be calculated using the following relation:

$$V_f = \frac{N_v V_p}{V_T} \tag{46}$$

where

V_T = 1 is a unit volume and

V_p is the volume of a particle.

Thus, it follows that

$$V_p = \frac{\pi D^3}{6} \tag{47}$$

Substituting V_p in equation (46)

$$N_v = \frac{6V_f}{\pi D^3} \tag{48}$$

Thus,

$$N_s = \frac{6V_f}{\pi D^2} \tag{49}$$

The surface area of a single particle is

$$S_p = \pi D^2 \tag{50}$$

The total area of intersected particles is

$$A_s = A_p \times N_s \tag{51}$$

Thus,

$$A_s = 6V_f \tag{52}$$

The increase in fracture energy of the alumina-filled epoxy composites with increasing filler volume fraction was particle size independent as shown in Table V. It is important to notice that the increase in fractured area caused by the addition of a filler is also particle size independent. In this study, for a volume fraction $\sim$ 0.5 the fracture energy of the composite was $\sim$ 5 times the fracture energy of the matrix. For a volume fraction of 0.5, this model predicts that the fractured area of the composite is 3 times the fractured area of the matrix. Thus, it would appear that the increase in fractured area can account for about 60% of the fracture energy increase. If it were considered that at some distance from the crack plane particle decohesion occurred as well, then the increase in fractured area would be greater than 3. However, no experimental data was obtained in this study regarding the decohesion of particles at a distance from the main crack.

Energy Absorbed by the Filler Particle

Scanning electron microscope observations of fracture surfaces revealed the presence of particles much smaller than the filler particles. These were indentified by X-ray spectral analysis as alumina particles. The fracture of small alumina chips did not appear to be a frequent event for the following reasons:

i) Scanning electron microscopy disclosed the existence of large sections of fracture surface, where embedded particles of the same size as the average particle size of the composite were observed (Figures 26 and 28).

ii) The fracture toughness of the alumina particles is greater than the fracture toughness of epoxy (Table XII). Thus, before the stress intensity in the crack tip reaches the value necessary to fracture the alumina particles, matrix failure occurs.

Thus, the fracture of alumina particles very likely had a negligible contribution on the total fracture energy of the alumina-filled epoxy composites.

Friction Between Parting Fracture Surfaces

Epoxy and alumina have different coefficients of thermal contractions (α); $\alpha_{Al_2O_3} = 70 \times 10^{-6} \circ C^{-1}$ (Ref. 26), $\alpha_{epoxy} = 8 \times 10^{-6} \circ C^{-1}$ (Ref. 19). This would have created residual stresses (σ) which had to be overcome to pull the particles out of the matrix[38]:

$$\frac{(\alpha_{Al_2O_3} - \alpha_{epoxy})(T_h - T_p)}{\left(\frac{1 + \nu_E}{2E_E}\right) + \left(\frac{1 - 2\nu_A}{E_A}\right)} \qquad (53)$$

TABLE XII

Fracture Constants and Elastic Moduli

of Epoxy and of Alumina

	Epoxy	Alumina
Young's Modulus (GPa)	4.0	393*
Fracture Toughness (MPa$\sqrt{m}$)	1.0	5.2+
Fracture Energy (N/m)	250	20x

* Reference 26.
\+ Reference 37.
x Reference 38.

where

T_h is the highest curing temperature ≈ 200°C and

T_p is the ambient temperature

Examining the fracture surface with a scanning microscope, particles partially pulled out of the matrix were frequently observed (Figure 28). Thus, it would appear that some energy was expended to pull out the particles in order to overcome friction between the particles and the matrix. The magnitude of the energy required for pulling out particles can be estimated as follows:

Work of Pull-Out

The work of friction (U_F) for pulling out a square particle is:

$$U_F = F_F \times D \tag{54}$$

where F_F is the friction force.

When the pull-out of a particle is initiated, the friction force is at maximum because the friction area is largest. Although a friction force is normally independent of area, in this case the normal force depends upon the area of particle

exposed to the residual stress. When the particle is almost completely pulled out, the friction force is zero. Thus,

$$F_F \simeq \frac{\sigma S_p}{2} \tag{55}$$

where

σ is the thermal stress and

S_p is the surface area of a particle

The total area exposed is:

$$A_s = 6V_f \tag{52}$$

Thus,

$$U_F = \frac{\sigma 6 \quad V_f}{2} \quad D \tag{56}$$

This model predicts that the pull-out energy is particle size dependent. The fracture energy of the alumina-filled epoxy composites tested in this study was not particle size dependent. Thus, it would appear that the energy required for pulling out particles was not a major reinforcing factor in this instance.

Interaction of the Crack Front with the Second Phase Dispersion

According to Lange[25,32,40], the pinning of the crack-front where the second phase exists increases the fracture

energy considerably. Since the crack front bows between each pair of pinning positions, its length increases before it breaks away from the pinning points. The energy required for the increase in crack length is called the line energy. Lange's equation for the fracture energy of the composite is[25]:

$$G = G_o + \frac{T}{d} \tag{57}$$

where G_o is the energy/unit area required to form a new fracture surface,

T is the critical line energy/unit length of the crack front,

d is the distance between pinning positions:

$$d = \frac{2D}{3} \frac{(1 - V_f)}{V_f} \tag{58}$$

Equation 57 indicates that when crack front particle interaction takes place, fracture energy is a linear function of the inverse of the interparticle distance. However, when there are so many particles ahead of the crack front that the composite becomes a "uniform" system, the fracture energy should drop. The relation of fracture energy and interparticle spacing of the composites examined in this study is linear see Figure 36. However, no drop in fracture energy was observed

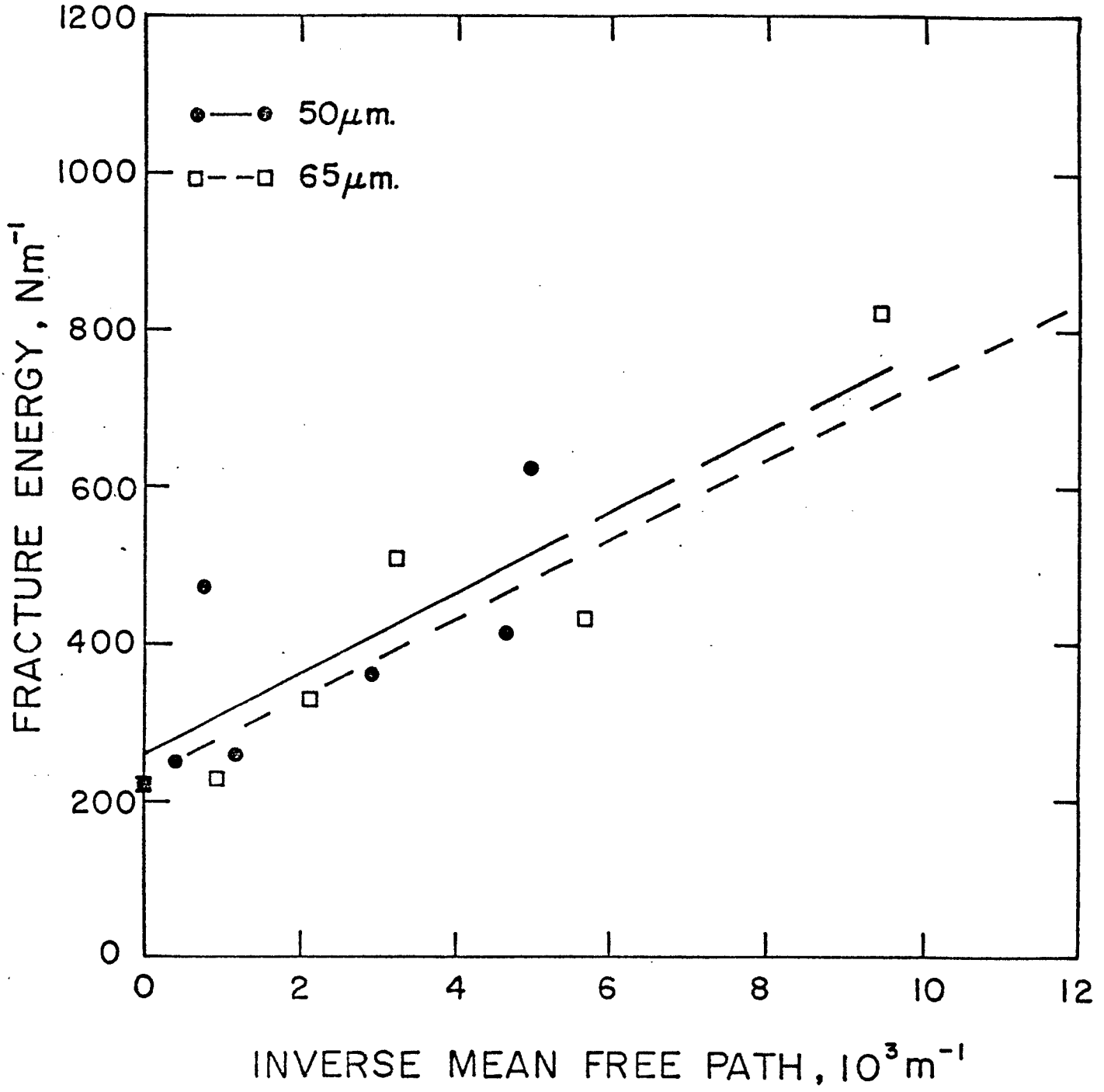

Figure 36a. Fracture energy versus mean free path for composites of differing particle size.

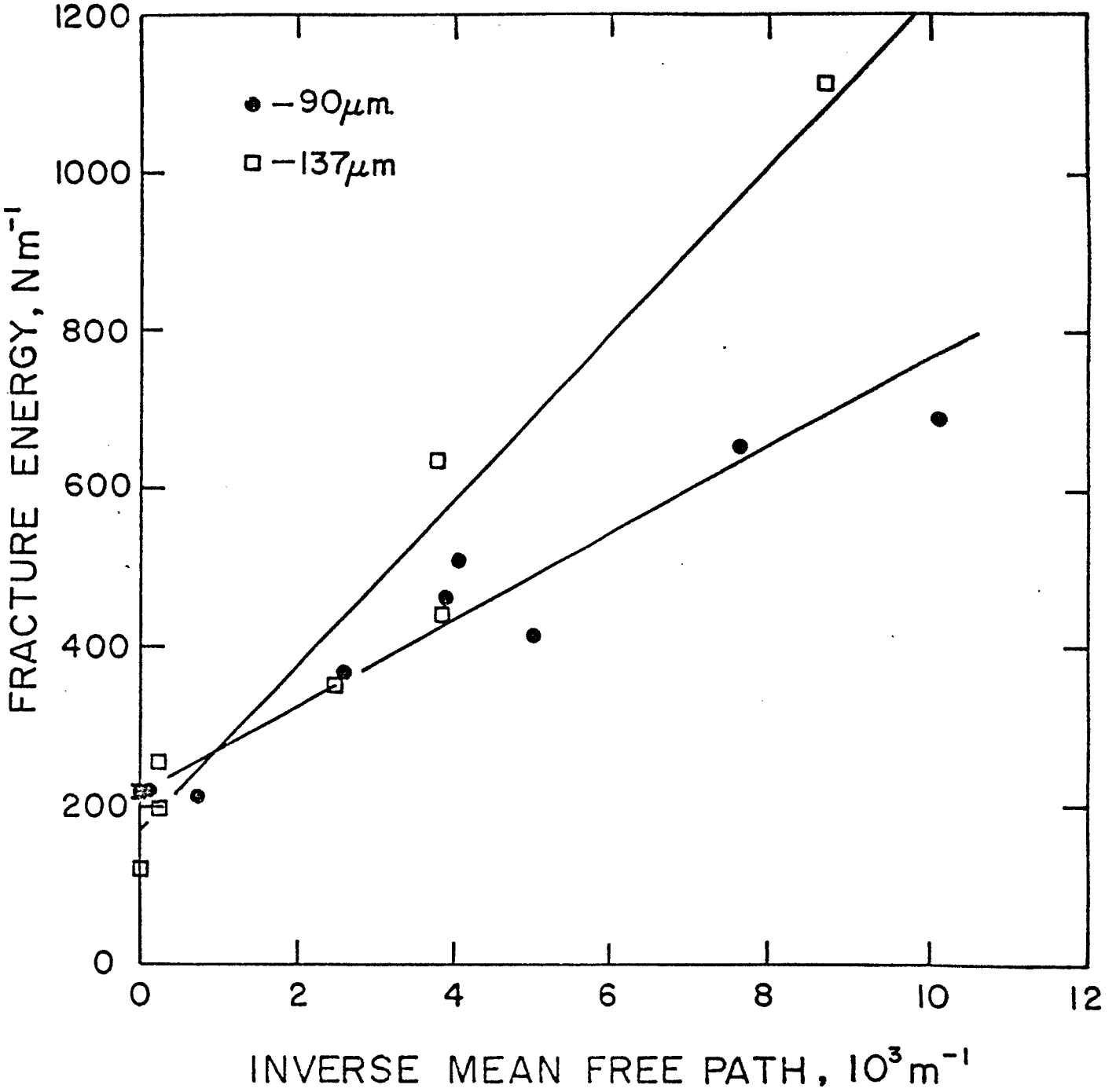

Figure 36b. Fracture energy versus mean free path for composites of differing particle size.

at large volume fractions of particles. Figure 37 shows the fracture energy of an epoxy $Al_2O_3 \cdot 3H_2O$ composite studied by Lange[40].

The evidence of diminished crack front-particle interaction for higher volume fractions than for intermediate volume fractions was obtained from the fracture surface and from AE studies. Comet marks left by the main crack behind the particles (see Figures 26a, 26b, 26c and 27) were observed up to intermediate volume fractions. The disappearance of comet marks at high volume fractions (see Figure 26d) is accompanied by a drop in AE (see Figure 21). For composites of small particle sizes, the marks ceased at lower volume fractions than they did for large particle sizes. This trend was also observed by Lange[25,40].

Evans et al[41] have proposed that the toughness increase observed when adding a dispersed second phase is a consequence of the crack deflection around the particles. For sphere-like dispersions, Evans et al[41] predict an increase in fracture energy with increasing volume fraction. The reinforcement due to crack deflection is particle size independent. For a volume fraction of 0.5, the fracture energy of the composite is predicted to be $\sim$ 1.8 times the fracture energy of the matrix. The toughness increase due to crack deflection

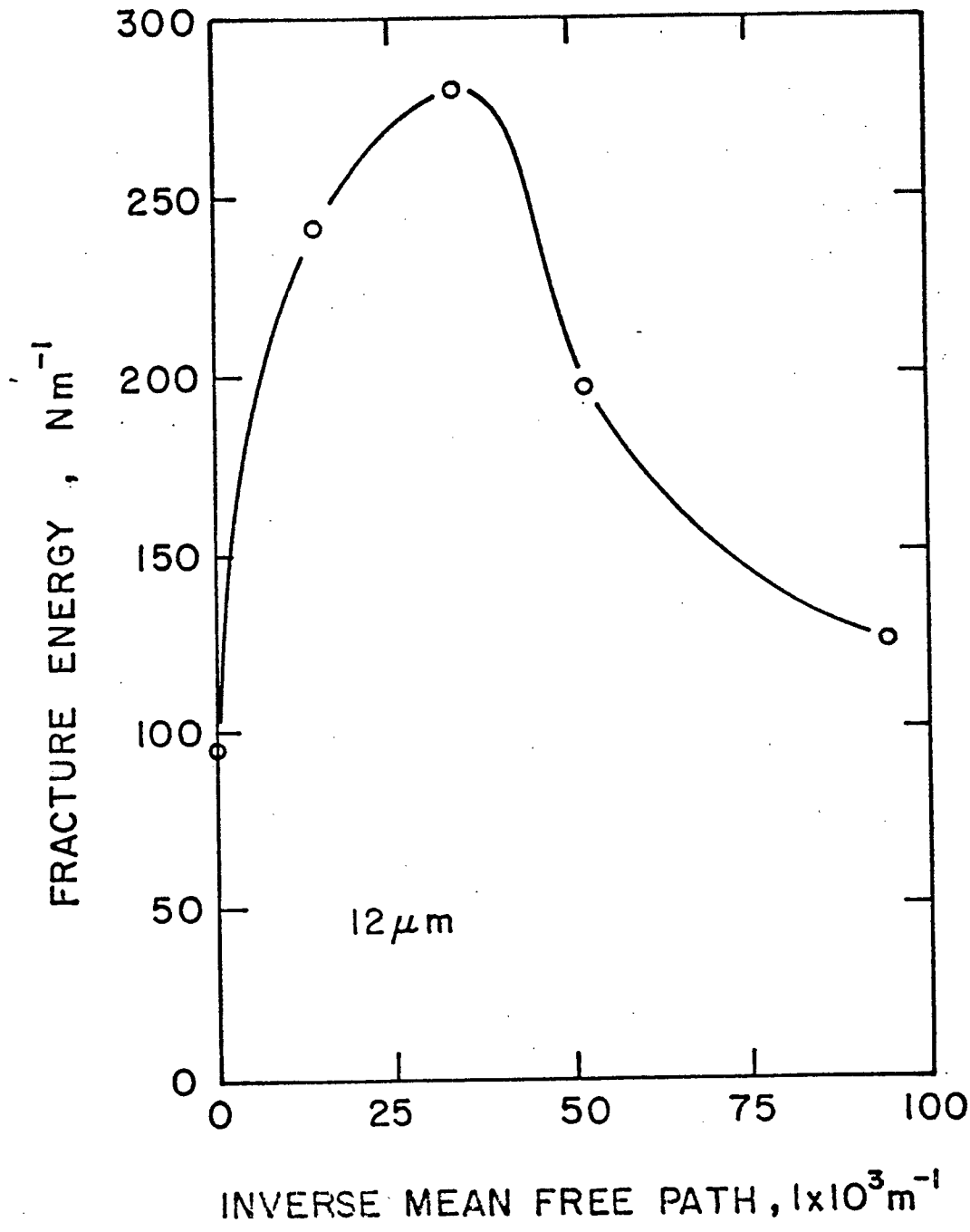

Figure 37. Fracture energy versus mean free path of an alumina trihydrate-epoxy composite[40].

could have made some contribution to the toughness of the alumina-filled epoxy composites tested in this study.

Debonding at crack tips in glass bead-filled epoxy has been observed[42]. The presence of such debonded zones can impede crack motion due to crack blunting. Crack blunting at semi-voids around alumina particles could have made some contribution to the fracture energy of the composites used here. This is a natural extension of the surface roughening process proposed earlier in this section.

Summary

The following factors appear to contribute to the fracture energy of alumina-filled epoxy:

i) Surface roughness.
ii) Crack deflection due to the presence of a dispersed phase.
iii) Crack blunting in semi-voids around particles.

For a volume fraction of $\sim$ 0.5, the fracture energy of the alumina-filled composites was $\sim$ 5 times the toughness of the matrix. The increase in surface area due to the presence of alumina particles was estimated here to be $\sim 6V_f$. Thus, for

a volume fraction of 0.5, the fractured area of the composite is ∿ 3 times the fractured area of epoxy. Consequently, surface roughness seems to be one of the major factors controlling the increase in toughness of the composites used in this study.

4.4. Acoustic Emission During Fracture

In the following section the possible factors which affect acoustic emission in alumina-reinforced epoxy will be analyzed and discussed.

Crazing

Crazing has been found to be a source of AE in plastics[43,44]. Using ordinary AE equipment, Peterlin[43] observed no significant variations in the AE of a plastic when crazing was increased. He concluded that the AE from crazing was masked by machine noises and more sophisticated equipment (laser displacement probe) was required to detect it.

The fibrils observed in epoxy, in this study, (Figures 23-25) seem to be crazes. Lilley and Holloway[45] have observed crazes in various epoxy resins fractured by wedge-loading. They found that the crazes developed in a direction perpendicular to the crack arrest marks, just as observed in this

study. No AE was detected during slow crack growth in pure epoxy. AE was generated only at the moment rapid crack propagation was reinitiated. Since it was in the crack arrest marks where crazes developed, it would appear that crazing is a source of AE in the unfilled matrix. However, the level of AE due to crazing was so low that it was not a factor in filled composites.

Interaction of the Crack Front with the Second Phase Dispersion

Nadeau[13] studied the AE during fracture of glass plates. These plates had a series of parallel grooves to represent microstructure. He found that AE resulted from successive pinning and breakaway of the main crack. No AE was detected below a threshold value of surface discontinuity. In the present study, the AE per unit area of composites with an alumina particle size of 40 μm was up to ∿ 4 times the AE per unit area of the matrix. Composites with an average particle size of 137 μm had an AE per unit area of up to ∿ 50 times that of the matrix. Thus, just as in Nadeau's study, a strong dependence was found between AE and discontinuity size.

When a crack is released from a pinning point (particle), load stress and strain accumulations are released and AE is produced. For small particles the pinning action is not very

large[25]. Consequently, local crack speed for surpassing small obstacles is not significantly greater than the crack speed in pure epoxy. Since the amplitude of emitted pulses increases with increasing crack velocity[8,13], small particles have little effect on AE. The converse holds true for large particles.

The AE per unit area of alumina-filled epoxy increased with increasing alumina volume fraction only when comet marks (see Section 4.3.) were present in the fracture surface. For high alumina volume fractions the composite becomes a "uniform" material to the crack front. Consequently, the pinning action on the crack decreases and AE per unit area decreases. It would appear that the pinning and breakaway of the main crack from discontinuities is a critical factor in the generation of AE.

Decohesion of Alumina Particles from the Matrix

If the main source of AE were the decohesion of alumina particles from the matrix, AE would increase monotonically with increasing volume fraction. However, AE per unit area values drop for high alumina volume fractions, as shown in Figures 21 and 22. Thus, the decohesion of the filler from epoxy cannot account for the observed behaviour.

Fracture of Alumina Particles

The fracture of alumina particles was disregarded as a major AE source for the same reasons as was decohesion of alumina particles from the matrix.

Friction between Parting Fracture Surfaces

The friction between parting fracture surfaces was neglected as a major factor contributing to AE for the same reason as decohesion of alumina.

Surface Roughness

The AE per area of some of the composites was up to 50 times that of the epoxy. Using a correction factor to take into account the surface roughness of the composite would have had no major effect on the AE per unit area values.

Summary

Crazing appears to be the major source of AE in pure epoxy. For the alumina-filled epoxy composites, the successive pinning and breakaway of the main crack from particles seems to be the major contributing factor to the generation of AE.

Even though the AE in this study yielded consistent results, a large scatter was observed in the AE data. In the worst cases, the standard variation of AE per area was found to have the same order of magnitude as the average value. Such standard variations were not found in other properties, such as fracture toughness. The difficulty in quantifying information contained in elastic waves and the complexity of wave propagation phenomena seriously limits the reliability of AE techniques.

CONCLUDING REMARKS

The fracture toughness and fracture energy of the composites studied increased with increasing volume fraction and were independent of alumina particle size. The increase in fracture surface due to the presence of the alumina particles accounted for about 60% of the fracture energy increase.

The AE per unit area during failure of the alumina-filled composites increased with increasing alumina particle size. A cut-off particle size of about 40 μm appears to exist, below which no AE increase occurs with the addition of particles. AE per unit area versus volume fraction curves exhibited a maximum at intermediate alumina volume fractions. The pinning and release of the crack front due to the presence of particles seemed to be the major contributing factor to the AE of alumina-filled composites.

APPENDIX

APPENDIX 1

Sample Table of the Data Collected During a Wedge Loading Test

Sample Width H (10^{-2} x m)	Plate Thickness in the plane of the Crack, Bn (10^{-2} x m)	Critical Load, $P^{+}_{x_1}$ (lbs)	Crack Length, a (10^{-2} x m)	AE (counts)	Step number, i
1.860	0.440	20.8	2.1	140	1
"	"	18.9	2.5	320	2
"	0.460	16.6	3.0	400	3
"	"	14.8	3.3	570	4
"	0.490	14.6	3.8	780	5
"	0.450	14.4	4.1	450	6
"	0.480	14.0	4.4	610	7
"	0.460	14.5	4.7	2120	8
"	0.420	13.9	5.8	210	9
"	"	10.2	6.0	2460	10
"	0.440	8.8	7.1	1020	11
"	0.460	8.8	7.7	1540	12
"	0.440	8.3	8.0	1290	13
"	0.430	7.9	8.6	2170	14
"	0.430	7.4	8.9	1150	15
"	0.440	6.8	9.3	1320	16
"	0.430	6.7	9.7	3460	17
"	"	6.9	10.3	1330	18
"	0.460	6.2	10.9	410	19
"	0.410	6.4	11.2	610	20
"	0.400	6.1	12.1	2190	21
"	0.410	5.3	13.6	980	22
"	0.430	5.7	14.0	1810	23
"	"	5.7	14.4	2120	24
"	0.430	9.4	15.2	1550	25
"	0.440	9.6	15.5	1450	26
"	0.460	4.8	16.3	14360	27

Alumina volume fraction: 0.076
Average alumina particle size: 129 μm
Sample thickness: 1.27×10^{-2} m.
Sample length: 18.0×10^{-2} m.

$^{+}$ $P = \dfrac{P_{x_1}}{2 \tan \theta}$

REFERENCES

1. Dunegan/Endevco, "System Design", Short Course on Acoustic Emission, San Juan Capistrano, California, June 17-21, 1974, p. 1.

2. H.N.G. Wadley, C.B. Scruby and J.H. Speake, "Acoustic Emission for Physical Examination of Metals", International Metals Reviews 25 (1980) 41.

3. A.A. Pollock, "Acoustic Emission-2. Acoustic Emission Amplitudes", Non-Destructive Testing 6 (1973) 264.

4. C.R. Heiple, S.H. Carpenter and M.J. Carr, "Acoustic Emission from Dislocation Motion in Precipitation-Strengthened Alloys", Metal Science 15 (1981) 587.

5. C.B. Scruby, H.N.G. Wadley, K. Rusbridge and D. Stockham-Jones, "Influence of Microstructure on Acoustic Emission during Deformation of Aluminum Alloys", Metal Science 15 (1981) 599.

6. S. Mc K. Cousland and C.M. Scala, "Acoustic Emission and Microstructure in Aluminum Alloys 7075 and 7050", Metal Science 15 (1981) 609.

7. T.J.C. Webborn and R.D. Rawlings, "Acoustic Emission from Structural Steels and Fe-C Alloys", Metal Science 15 (1981) 533.

8. J.H. Williams, Jr. and S.S. Lee, "Acoustic Emission from Graphite/Epoxy Composites Containing Interlaminar Paper Inclusions", NDT International 12 (1979) 5.

9. K. Ono, M. Shibata and M.A. Hamstad, "A Note on the Anisotropic Acoustic Emission Behaviour of HSLA Steels", Metallurgical Transactions A 10A (1979) 761.

10. M.A. Hamstad, E.M. Leon and A.K. Mukherjee, "Acoustic Emission under Biaxial Stresses in Unflawed 21-6-9 and 304 Stainless Steel", Metal Science 15 (1981) 541.

11. A. Frydman and A. Pszonka, "Acoustic Emission of Two Phase Brass", Materials Science and Engineering 40 (1979) 191.

12. R. Bunch, M.A. Hamstad and A.K. Mukherjee, "Correlation Between Acoustic Emission and Microstructure in Aluminum Alloys", UCRL Report 81879, 1978, Lawrence Livermore Lab., Cal.

13. J.S. Nadeau, "Origins of Acoustic Emission in the Fracture of Glass Plates", ICF-4, Volume 3, Ed. by D.M.R. Taplin, Waterloo, Ontario, 1977 (University of Waterloo, Press) p. 979.

14. J. Baram, Y. Gefen and M. Rosen, "Acoustic Emission Generated during a Single Interface Movement in the Martensitic Transformation of Au-47.5% Cd. Alloy", Scripta Metallurgica 15 (1981) 835.

15. R. Pascual, M. Ahlers, R. Rapacioli and W. Arneodo, "Acoustic Emission and the Martensitic Transformation of β Brass", Scripta Metallurgica 9 (1975) 79.

16. A.A. Pollock, "Wave Propagation of Acoustic Emission", Short Course on Acoustic Emission, San Juan Capistrano, California, June 17-21, 1974, p. 1.

17. E.P. Papadakis, Physical Acoustics, Ed. by W.P. Mason, 1976 (Academic Press Inc., N.Y.) p. 277.

18. J.S. Nadeau, "Acoustic Emission in the Fracture of Glass Plates", Journal of the American Ceramic Society 64 (1981) 587.

19. R.J. Crowson and R.G.C. Arridge, "The Elastic Properties in Bulk and Shear of a Glass Bead-Reinforced Epoxy Resin Composite", Journal of Materials Science 12 (1977) 2154.

20. D.P. Williams and A.G. Evans, "A Simple Method for Studying Slow Crack Growth", ASTM Journal of Testing and Evaluation 1 (1973) 264.

21. A.G. Evans, "A Simple Method for Evaluating Slow Crack Growth in Brittle Materials", International Journal of Fracture 9 (1973) 267.

22. R.G. Hoagland, A.R. Rosenfield and G.T. Hahn, "Mechanisms of Fast Fracture and Arrest in Steels", Metallurgical Transactions 3 (1972) 123.

23. H. Tada, G. Paris and G. Irwin, The Stress Analysis of Cracks Handbook, 1973 (Del Research Corporation, Hellertown, Pennsylvania) p. 2.16.

24. F.F. Lange, "Effect of Microstructure on Strength of Si_3N_4-SiC Composite System", Journal of the American Ceramic Society 56 (1973) 445.

25. F.F. Lange, "Fracture Energy and Strength Behaviour of a Sodium Borosilicate Glass-Alumina Composite System", Journal of the American Ceramic Society 54 (1971) 614.

26. R.P. Wahi and B. Ilschner, "Fracture Behaviour of Composites based on Al_2O_3-TiC", Journal of Materials Science 15 (1980) 875.

27. R.J. Young and P.W.R. Beaumont, "Failure of Brittle Polymers by Slow Crack Growth", Journal of Materials Science 10 (1975) 1343.

28. R.G. Hoagland, C.W. Marschall and A.R. Rosenfield, Microstructural Factors Influencing Fracture Toughness of Hafnium Titanate", Materials Science and Engineering 15 (1974) 51.

29. E.H. Kerner, "The Elastic and Thermoelastic Properties of Composite Media", Proceeding Physics Society 69B (1956) 808.

30. B. Paul, "Prediction of Elastic Constants of Multiphase Materials", Transactions of the Metallurgical Society of AIME, 218 (1960) 36.

31. O. Ishai, (Discussion of paper by U.J. Counto), Magazine of Concrete Research 17 (1965) 148.

32. F.F. Lange, Composite Materials, Vol. 5, Ed. by L.J. Broutman, 1974 (Academic Press Inc., N.Y.) p. 1.

33. W.P. Mason, Physical Acoustics, Vol. IV, Part A, Ed. by W.P. Mason, 1966 (Academic Press Inc., N.Y.), p. 299.

34. D.E. Munson, R.R. Boade and K.W. Schuler, "Stress Wave Propagation in Al_2O_3 - Epoxy Mixtures", Journal of Applied Physics 49 (1978) 4797.

35. P.J. Torvik, "Shock Propagation in a Composite Material", Journal of Composite Materials 4 (1970) 296.

36. R.L. Fullman, "Measurement of Particle Sizes in Opaque Bodies", Transactions AIME, 197, (1953) 447.

37. A.G. Evans, "A Method for Evaluating the Time-Dependent Failure Characteristics of Brittle-Materials - and its Application to Polycrystalline Alumina", Journal of Materials Science 7 (1972) 1137.

38. L.A. Simpson, "Effect of Microstructure on Measurements of Fracture Energy of Al_2O_3", Journal of the American Ceramic Society 56 (1973) 7.

39. F.F. Lange, Fracture Mechanics of Ceramics, Vol. 2, Ed. by R.C. Bradt, DPH Hasselman and F.F. Lange, 1978 (Plenum Press, N.Y.) p. 599.

40. F.F. Lange, K.C. Radford, "Fracture Energy of an Epoxy Composite System", Journal of Materials Science 6 (1971) 1197.

41. K.T. Faber and A.G. Evans, "Crack Deflection Processes: I, Theory", to be published by Acta Metallurgica.

42. A.B. Owen, "Direct Observations of Debonding at Crack Tips in Glass Bead-Filled Epoxy", Journal of Materials Science 14 (1979) 2521.

43. A. Peterlin, B.B. Djordjevic, J.C. Murphy, R.E. Gree, Jr., "AE during Craze Formation in Polymers", to be published.

44. H.H. Kausch, Polymer Fracture, 1978 (Springe-Verlag Press, N.Y.) p. 272.

45. J. Lilley, D.G. Holloway, "Crazing in Epoxy Resins", Philosophical Magazine 28 (1973) 215.